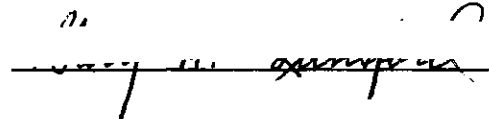


In presenting the dissertation as a partial fulfillment of the requirements for an advanced degree from the Georgia Institute of Technology, I agree that the Library of the Institute shall make it available for inspection and circulation in accordance with its regulations governing materials of this type. I agree that permission to copy from, or to publish from, this dissertation may be granted by the professor under whose direction it was written, or, in his absence, by the Dean of the Graduate Division when such copying or publication is solely for scholarly purposes and does not involve potential financial gain. It is understood that any copying from, or publication of, this dissertation which involves potential financial gain will not be allowed without written permission.

A handwritten signature in black ink, appearing to be "W. H. ...", written over a horizontal line.

7/25/68

STOCHASTIC BEHAVIOR OF RESONANT,  
NEARLY-LINEAR OSCILLATOR SYSTEMS  
FOR ARBITRARILY SMALL NONLINEAR COUPLING

A THESIS

Presented to  
The Faculty of the Graduate Division  
by  
Gary Hamilton Lunsford

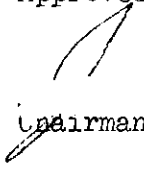
In Partial Fulfillment  
of the Requirements for the Degree  
Doctor of Philosophy  
in the School of Physics

Georgia Institute of Technology

December, 1971

STOCHASTIC BEHAVIOR OF RESONANT,  
NEARLY-LINEAR OSCILLATOR SYSTEMS  
FOR ARBITRARILY SMALL NONLINEAR COUPLING

Approved:

  
Chairman

Date approved by chairman: 12/6/71

## ACKNOWLEDGMENTS

The author wishes to thank Dr. Joseph Ford for suggesting these studies, and for his guidance and encouragement throughout the work. The author is also grateful to Dr. Harold Gersch and Dr. Marvin Sledd for their suggestions and comments during the preparation of the manuscript, and to Miss Wynette Wright for her work in typing the final draft.

## TABLE OF CONTENTS

	Page
ACKNOWLEDGMENTS . . . . .	ii
LIST OF TABLES . . . . .	iv
LIST OF ILLUSTRATIONS . . . . .	v
SUMMARY . . . . .	viii
Chapter	
I. INTRODUCTION . . . . .	1
II. GENERAL THEORY FOR THE N-OSCILLATOR SYSTEM WITH SMALL NONLINEARITY . . . . .	13
III. STOCHASTICITY FOR $N = 3$ AND $\gamma = 1$ . . . . .	21
IV. STOCHASTICITY IN THE LIMIT AS $\gamma$ TENDS TO ZERO FOR $N = 3$ . . . . .	46
V. AREA-PRESERVING MAPPINGS . . . . .	51
VI. PATHOLOGY OF AREA-PRESERVING MAPPINGS . . . . .	60
Analysis of Separatrix Behavior Stability Analysis Technique of Greene	
VII. STABILITY OF PERIODIC ORBITS OF THE HENON AND HEILES SYSTEM . . . . .	86
VIII. CONCLUSIONS . . . . .	108
APPENDIX A . . . . .	114
APPENDIX B . . . . .	118
APPENDIX C . . . . .	121
FOOTNOTES . . . . .	123
VITA . . . . .	126

## LIST OF TABLES

Table		Page
1.	Percentage of Stochastic Trajectories for Hamiltonian (III-1) with $H = 3.00$ and $\gamma = 1$ . . . . .	40
2.	Percentage of Stochastic Trajectories for Hamiltonian (III-1) in the Limit as $\gamma \rightarrow 0$ . . . . .	49
3.	The Quantity $f =  R ^{2/Q}$ As a Function of $Q/P$ for Selected Fixed Points of the Henon and Heiles System at Energy $E = 1/12$ . . . . .	92
4.	The Residue as a Function of System Energy for the $5/1$ Fixed-Point Family in the Henon and Heiles System . . . . .	99

## LIST OF ILLUSTRATIONS

Figure		Page
1.	Level Curves for the Henon and Heiles System for Energy $E = 1/12$ . . . . .	6
2.	Level Curves for the Henon and Heiles System for Energy $E = 1/8$ . . . . .	7
3.	Level Curves for the Henon and Heiles System for Energy $E = 1/6$ . . . . .	8
4.	Level Curves for Hamiltonian (III-6) with $H = 3.00$ , $J_1 = 2.999$ , $K = 0.001$ , and $\alpha = 0.100$ for Seven Starting Points . . . . .	28
5.	Level Curves for Hamiltonian (III-6) with $H = 3.00$ , $J_1 = 2.999$ , $K = 0.001$ , and $\alpha = 0.100$ for Two Starting Points . . . . .	29
6.	Level Curves for Hamiltonian (III-6) with $H = 3.00$ , $J_1 = 2.901$ , $K = 0.099$ , and $\alpha = 0.100$ for Five Starting Points . . . . .	30
7.	Level Curves for Hamiltonian (III-6) with $H = 3.00$ , $J_1 = 2.901$ , $K = 0.099$ , and $\alpha = 0.100$ for One Starting Point . . . . .	31
8.	Level Curves for Hamiltonian (III-6) with $H = 3.00$ , $J_1 = 2.990$ , $K = 0.010$ , and $\alpha = 0.000$ for Six Starting Points . . . . .	32
9.	Level Curves for Hamiltonian (III-6) with $H = 3.00$ , $J_1 = 2.990$ , $K = 0.010$ , and $\alpha = 0.001$ for Six Starting Points . . . . .	33
10.	Level Curves for Hamiltonian (III-6) with $H = 3.00$ , $J_1 = 2.990$ , $K = 0.010$ , and $\alpha = 0.010$ for Six Starting Points . . . . .	34
11.	Level Curves for Hamiltonian (III-6) with $H = 3.00$ , $J_1 = 2.990$ , $K = 0.010$ , and $\alpha = 0.025$ for Six Starting Points . . . . .	35

## LIST OF ILLUSTRATIONS (Continued)

Figure		Page
12.	Level Curves for Hamiltonian (III-6) with $H = 3.00$ , $J_1 = 2.990$ , $K = 0.010$ , and $\alpha = 0.050$ for Six Starting Points . . . . .	36
13.	Level Curves for Hamiltonian (III-6) with $H = 3.00$ , $J_1 = 2.990$ , $K = 0.010$ , and $\alpha = 0.0185$ for One Starting Point . . . . .	37
14.	A Plot of Phase Space Separation Distance Between Two Initially Close Trajectories Started in a Stable Region . . . . .	43
15.	A Plot of $\log_{10}$ of the Separation Distance Versus Time for Four Distinct Orbit-Pairs . . . . .	44
16.	Typical Graph of the Mapping Generated by Equations (V-5), Showing Only the Grossest Features . . .	55
17.	The Henon Algebraic Mapping of Equations (V-6) for $\cos \alpha = 0.24$ . . . . .	57
18.	A Magnified Region Around the Rightmost Hyperbolic Fixed Point of the Henon Mapping for $\cos \alpha = 0.24$ . . . .	58
19.	Invariant Curves for an Integrable Mapping . . . . .	64
20.	Invariant Curves for a Small Non-integrable Perturbation . . . . .	65
21.	An Adjacent Pair of Hyperbolic II Fixed Points for the Laslett Mapping of Equations (VI-11) . . . . .	68
22.	An Example of the Arnold Mapping of Equations (VI-12) Which is Ergodic and Mixing . . . . .	72
23.	Some Fixed Points of the Greene Algebraic Mapping Given by Equations (VI-14) . . . . .	75
24.	A Plot of $f = (4R)^{2/Q}$ Versus Inverse Rotation Number for Selected Fixed Points of the Greene Mapping . . . . .	83
25.	Selected Periodic Orbits in the Henon and Heiles Level Curve Plane for Energy $E = 1/12$ . . . . .	89



## LIST OF ILLUSTRATIONS (Concluded)

Figure		Page
26.	A Plot of $f =  R ^{2/Q}$ Versus Inverse Rotation Number for Selected Fixed Points of the Henon and Heiles System at Energy $E = 1/12$ . . . . .	91
27.	A Plot of $f =  R ^{2/Q}$ Versus Inverse Rotation Number for Selected Fixed Points of the Henon and Heiles System at Energy $E = 1/8$ . . . . .	96
28.	The Profile of Residue Versus System Energy for the 5/1 Fixed-Point Family in the Henon and Heiles System . . . . .	98
29.	The Profile of Residue Versus System Energy for the 8/1 Fixed-Point Family in the Henon and Heiles System . . . . .	102
30.	A Plot of Residue Versus System Energy for the Original and Bifurcated 8/1 Periodic Orbits of the Henon and Heiles System . . . . .	104

## SUMMARY

This thesis investigates the classical motion of nonlinear oscillator systems governed by Hamiltonians having the nearly-linear form

$$H = \sum_{k=1}^N \frac{\omega_k}{2} (P_k^2 + Q_k^2) + \gamma [V_3 + V_4 + \dots], \quad (1)$$

where  $N$  is the number of oscillators,  $\omega_k$  are the positive frequencies of the harmonic approximation,  $\gamma$  is the nonlinear coupling parameter, and  $V_3$ ,  $V_4$ , etc., are the cubic, quartic, etc., polynomials in  $Q_k$  and  $P_k$ . The purpose of this investigation is to demonstrate that macroscopic irreversibility is an inherent property of physical nearly-linear oscillator systems, even in the limit as the nonlinear parameter  $\gamma$  tends toward zero. In particular, we focus our attention on the individual trajectories of Hamiltonian (1) and seek to determine the conditions under which most of these trajectories exhibit stochastic behavior, by which we mean that a trajectory wanders more or less randomly over part or most of the energy surface. From the viewpoint of thermodynamics, most of the microscopic, mechanical states  $(Q_k, P_k)$  on a widely stochastic trajectory would correspond to macroscopic thermodynamic equilibrium states ( $P, V, T$ , etc.). Thus starting the trajectory in a "disequilibrium"  $(Q_k, P_k)$  state would inevitably lead to equilibrium, giving the appearance of irreversibility. In essence, then, our central purpose is to expose those essential properties of Hamiltonian

(1) that are crucial for irreversibility as the nonlinear coupling tends to zero.

For the nearly-linear oscillator models described by Hamiltonian (1), we demonstrate that widespread stochasticity can occur for arbitrarily small but nonzero  $\gamma$  provided that  $N \geq 3$  and that the  $\omega_k$  satisfy commensurability conditions which allow certain of the  $V_3$  and/or  $V_4$  interaction terms to strongly couple all internal degrees of freedom. This widespread stochasticity is demonstrated through an extensive computer study of the case  $N = 3$ , a case which is especially suitable for study since it possesses much of the complexity of the full many-body problem and yet is sufficiently simple to yield to graphical analysis, which provides a strikingly lucid pictorial display of the random motion of individual trajectories.

The computer study also shows that system trajectories originally close to each other in a stochastic region of phase space can move apart more or less exponentially with time. This exponential stirring of phase space is of the type which Gibbs envisioned as leading to irreversible behavior. In particular, the slightest uncertainty in the initial state leads very quickly to complete uncertainty of the final state. Since the nonlinear oscillator systems, thought of as a model for a solid, share ownership of exponentially divergent trajectories with gaseous systems, we are led to believe that this exponentiating property is perhaps the ultimate source of irreversibility in physical systems exhibiting an approach to equilibrium.

Having determined criteria for which nearly-linear Hamiltonian systems may exhibit stochastic behavior and having established that

stochastic systems may exhibit exponentially separating orbits, the thesis then directs its attention to elaborating further details of the motion in the stochastic region of phase space. In particular, attention is focused on the periodic orbits which appear to be dense throughout such regions. If each of these periodic orbits could be shown to be unstable, in the sense that neighboring non-periodic orbits would all diverge exponentially, then one would anticipate that each non-periodic orbit uniformly covers the whole stochastic region in an almost random fashion. In the graphical procedures used and described herein, periodic orbits appear as fixed points in a plane area-preserving mapping. Stability of the periodic orbits is thereby reduced to determining the stability of fixed points of the associated mapping. Using recently developed numerical procedures, it is established that a large and perhaps dense class of these fixed points is indeed unstable. Nonetheless, it appears that some stable periodic orbits continue to exist, which disallows uniform stochasticity throughout the basically unstable region.

## CHAPTER I

## INTRODUCTION

Classical statistical mechanics is founded on the premise that the phase space trajectories for an isolated system wander freely over the energy surface. It then deduces that the vast majority of mechanical, microstates  $(Q_i, P_i)$  on the energy surface correspond to macroscopic, thermodynamic equilibrium states  $(P, V, T, \text{etc.})$ . One thus expects that an isolated system--started in some disequilibrium state and subsequently allowed to follow its assumed tendency to wander freely over the energy surface--would surely tend to equilibrium. Certainly the approach to equilibrium might not be monotonic and even large fluctuations from equilibrium might occur and recur; nonetheless, the general trend would be for the system to approach equilibrium and remain there. Using such partially intuitive arguments for a foundation, statistical mechanics has erected a theoretical structure which correctly predicts all calculable equilibrium properties and which accurately describes non-equilibrium properties, at least for a limited range of systems and disequilibrium initial states.

From the viewpoint of classical mechanics, however, the enormous success of statistical mechanics appears somewhat paradoxical. All the solvable problems of classical mechanics yield trajectories which do not wander freely over the energy surface. Indeed a survey of the solvable problems shows that they all possess as many single-valued, analytic constants of the motion as there are degrees of freedom. Such

systems are said to be integrable, and the trajectory for such a system with  $N$  degrees of freedom can wander freely only over an  $N$ -dimensional subspace of the  $(2N-1)$ -dimensional energy surface.

This gap between statistical mechanics and classical mechanics does not narrow even if one includes those nonintegrable systems which can be treated by classical perturbation theory. Here one considers systems with  $N$  degrees of freedom governed by Hamiltonians of the form

$$H = H_0 + \gamma V, \quad (I-1)$$

where  $\gamma V$  represents a small perturbation to the integrable Hamiltonian  $H_0$ , and  $H_0$  may, without loss of generality, be taken to be a function of the generalized momentum variables  $P_i$  alone.<sup>1</sup> For such systems a recent theorem due to Kolmogorov,<sup>2</sup> Arnold,<sup>3</sup> and Moser<sup>4</sup> proves that, under very weak and general conditions, Hamiltonians (I-1) do not generate trajectories which wander freely over the  $(2N-1)$ -dimensional energy surface. Indeed the Kolmogorov-Arnold-Moser (hereafter called KAM) Theorem asserts that Hamiltonians (I-1) yield trajectories which, excepting a set of small measure, lie on smooth,  $N$ -dimensional, integral surfaces called tori embedded in the  $2N$ -dimensional phase space provided, among other things,

- (i) the perturbation  $\gamma V$  is sufficiently small, and
- (ii) the determinant of the matrix  $\{\partial^2 H_0 / \partial P_i \partial P_j\}$  does not vanish identically.

In essence, the KAM Theorem asserts that, even though nonintegrable, Hamiltonians (I-1) display integrable system behavior for the most part.

Although statistical mechanics is much too well established and experimentally verified to be shaken by the KAM results, the findings of KAM do at first glance come perilously close to forming a breach rather than a gap between statistical mechanics and classical mechanics. In particular, statistical mechanics frequently considers systems of the type governed by Hamiltonians (I-1) and asserts that their equilibrium properties may be calculated using the canonical probability distribution  $e^{-H_0/kT}$ , where  $k$  is the Boltzmann constant and  $T$  is the absolute temperature. Most especially one should note that this canonical distribution neglects the weak perturbation  $\gamma V$ , tacitly assuming that the perturbation is too small to influence equilibrium properties even though it, and it alone, serves to bring the system to equilibrium. In short, statistical mechanics makes the uncommon physical assumption that a very small cause results in an incredibly large effect. Despite these facts, there exists only a gap rather than a breach because statistical mechanics is completely non-committal in regard to the characteristics of the  $\gamma V$  perturbation which are required of systems falling under its jurisdiction. As a result, no contradiction exists.

But aside from any element of contradiction, there are several reasons for seeking classical mechanical models which can be shown to exhibit the properties assumed by statistical mechanics. First, there is the desire, even if academic, to answer a host of troublesome questions concerning the foundations of statistical mechanics; for until all such questions are answered, there remains a lingering, even if minor, suspicion that there exist physically interesting  $N$ -body systems which lie outside the province of statistical mechanics. But perhaps

more important, it is conjectured that such models might prove invaluable in the development of a general theory for irreversible processes. For both these reasons, it is highly gratifying to note that recent computer experiments, supported by theoretical work, indicate that the conditions of the KAM Theorem form the dividing line between statistical and non-statistical trajectories for the systems of Hamiltonian (I-1). We now discuss briefly some of the recent work which demonstrates that violation of KAM Condition (i) leads to freely wandering trajectories when the perturbation  $\gamma V$  is large; the remainder of this thesis then demonstrates that, provided KAM Condition (ii) is violated, statistical behavior can occur no matter how small the perturbation  $\gamma V$ , thus demonstrating that small causes can indeed have enormous consequences.

Although not the first,<sup>5,6</sup> the work of Henon and Heiles<sup>7</sup> provides perhaps the clearest example of freely wandering trajectories, once KAM Condition (i) is violated. These investigators chose to consider the bounded motion generated by the two-oscillator Hamiltonian

$$H = (1/2)(p_1^2 + p_2^2 + q_1^2 + q_2^2) + q_1^2 q_2 - (1/3)q_2^3. \quad (I-2)$$

In order to survey the nature of the trajectories for Hamiltonian (I-2), a Poincaré surface of section was utilized.<sup>16</sup> We shall also refer to a surface of section as a level curve plane in this thesis. In applying this technique, one first notes that the trajectories for Hamiltonian (I-2) lie in a four-dimensional phase space  $(q_1, p_1, q_2, p_2)$ . However, since the Hamiltonian (or energy) is a constant of the motion, we are permitted to plot trajectories in the three-space  $(q_1, q_2, p_2)$ , since  $p_1$



may be determined from Equation (I-2). Let us now introduce as our surface of section (of the three-space) the plane  $(q_2, p_2)$ , and consider the set of points generated by a given trajectory as it intersects this surface of section; i.e., those  $(q_2, p_2)$  coordinates on a trajectory for which  $q_1 = 0$  and  $p_1 \geq 0$ . If the perturbation term  $\gamma V = q_1^2 q_2 - (1/3)q_2^3$  is sufficiently small with respect to the unperturbed, integrable Hamiltonian  $H_0 = (1/2)(p_1^2 + p_2^2 + q_1^2 + q_2^2)$ , as it will be for the low energy motion of Hamiltonian (I-2), then one may apply the KAM Theorem. In this situation, most trajectories will lie on smooth, two-dimensional integral surfaces, and the intersection points of each trajectory with the surface of section will form a curve. On the other hand at large energies where  $\gamma V$  is not small with respect to  $H_0$  and the KAM Condition (i) is violated, it is possible that each trajectory wanders freely over part or all of the  $(q_1, q_2, p_2)$  space. In this event, the trajectory intersection points with the surface of section would form a set of scattered points with little or no apparent correlation. Using this technique, Henon and Heiles surveyed the nature of the trajectories for Hamiltonian (I-2) at three distinct energies.

The results for the energy  $E = 1/12$  are shown in Figure 1. Here the system is seen to lie deep within the region of KAM stability, and we note that each trajectory investigated yields a curve of intersection points with the  $(q_2, p_2)$  plane. However at the increased energy  $E = 1/8$ , Figure 2 reveals the beginning of statistical or stochastic trajectories, since the scattered dots generated by a single trajectory cover more or less uniformly about 30 percent of the area allowed by the conservation of energy. Finally at the dissociation energy  $E = 1/6$ , Figure 3 indicates that almost all trajectories are statistical in character since

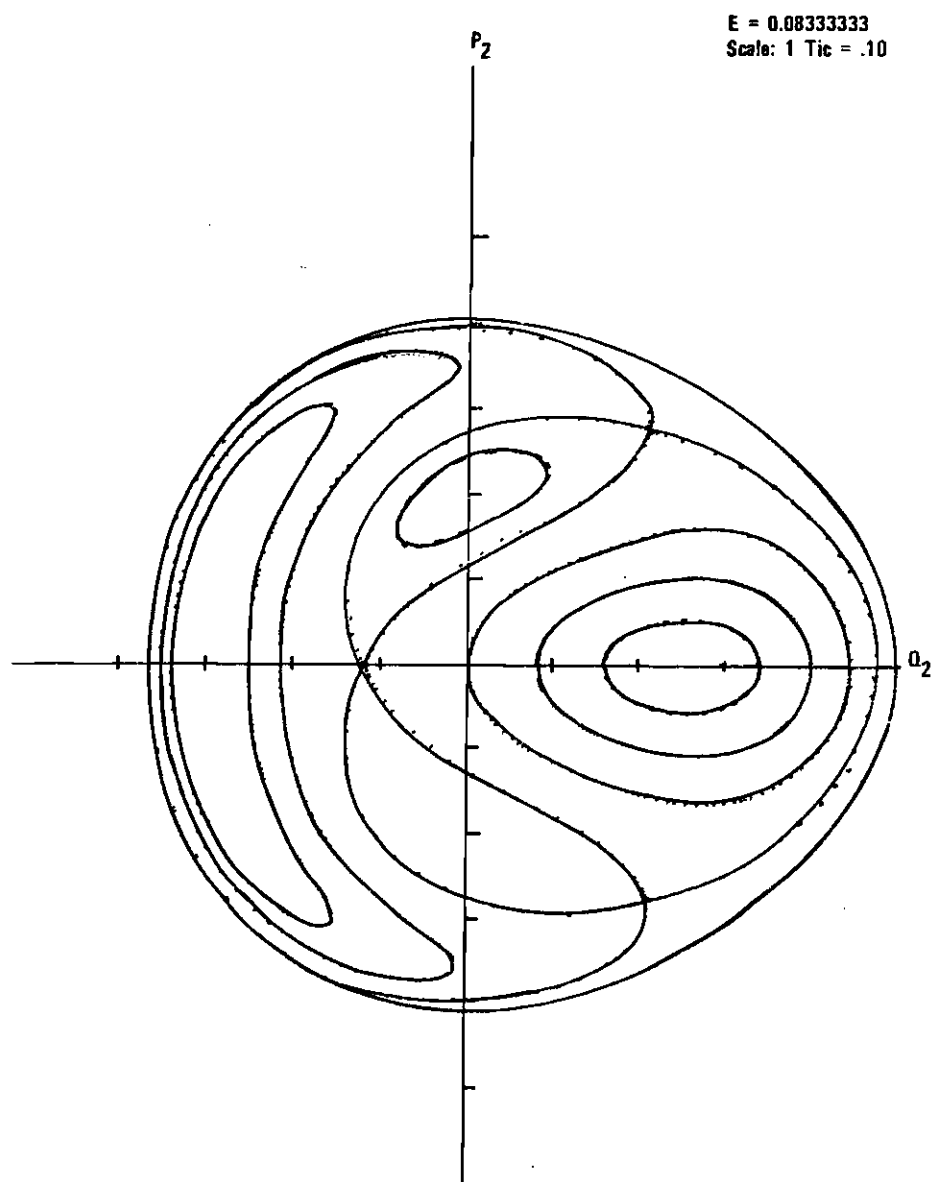


Figure 1. Level Curves for the Henon and Heiles System for Energy  $E = 1/12$ .

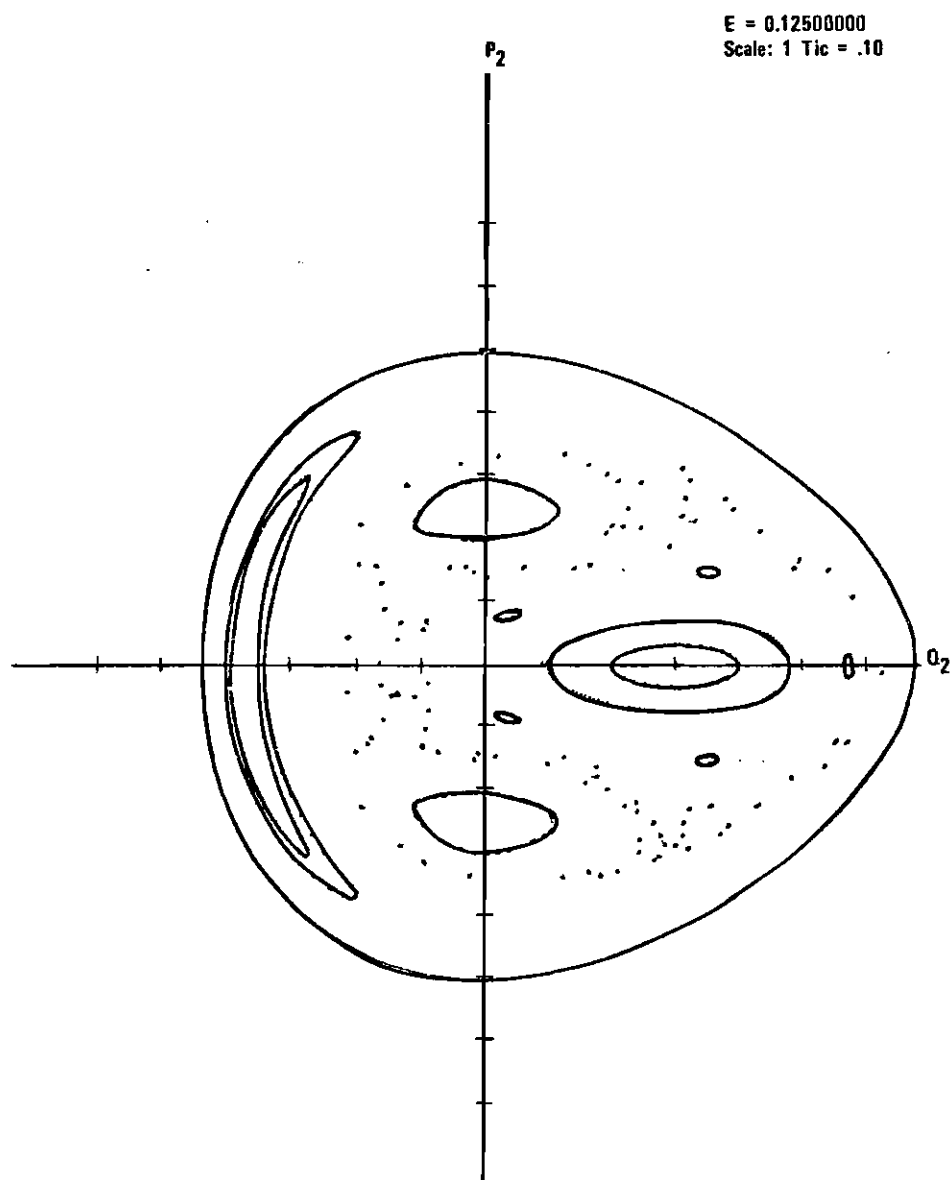


Figure 2. Level Curves for the Henon and Heiles System for Energy  $E = 1/8$ .

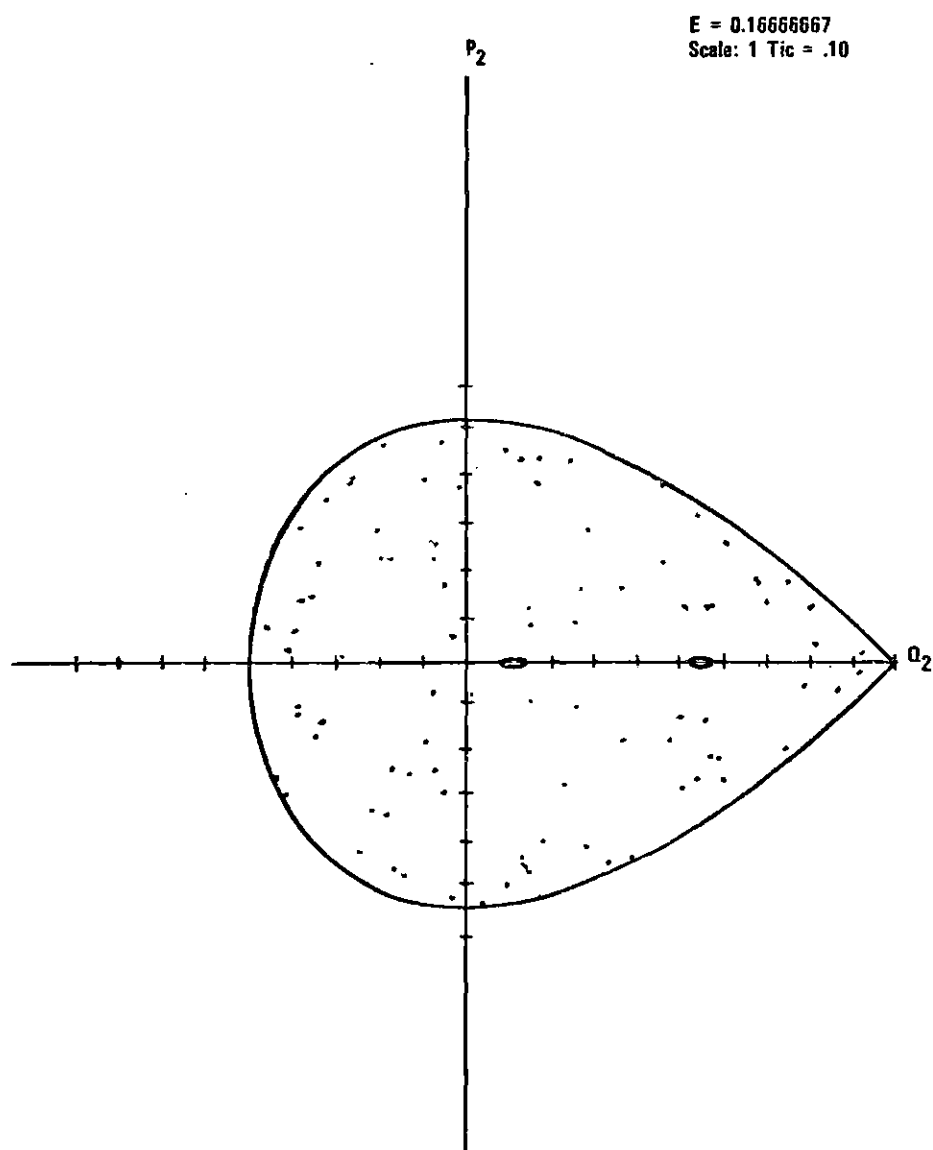


Figure 3. Level Curves for the Henon and Heiles System for Energy  $E = 1/6$ .

the  $(q_2, p_2)$  surface of section is now almost completely covered by the dots generated by a single trajectory.

In order to pave the way for the following sections of this thesis, we now further illuminate the application of the KAM Theorem to the Henon-Heiles system. Our discussion will omit much mathematical detail and the interested reader is referred to any of several review articles.<sup>1,8-10,16-19</sup> First, let us introduce into Hamiltonian (I-2) the canonical change of variables specified by

$$q_i = (2J_i)^{\frac{1}{2}} \cos \varphi_i, \quad (\text{I-3a})$$

$$p_i = -(2J_i)^{\frac{1}{2}} \sin \varphi_i; \quad i = 1, 2. \quad (\text{I-3b})$$

Hamiltonian (I-2) may then be written

$$\begin{aligned} H = & J_1 + J_2 + 2^{\frac{1}{2}} J_1 J_2^{\frac{1}{2}} \cos \varphi_2 + 2^{-\frac{1}{2}} J_1 J_2^{\frac{1}{2}} \cos(2\varphi_1 + \varphi_2) + \\ & 2^{-\frac{1}{2}} J_1 J_2^{\frac{1}{2}} \cos(2\varphi_1 - \varphi_2) - 2^{-\frac{1}{2}} J_2^{\frac{3}{2}} \cos \varphi_2 - (1/3\sqrt{2}) J_2^{\frac{3}{2}} \cos 3\varphi_2, \end{aligned} \quad (\text{I-4})$$

where the  $J_i$  are generalized momenta variables and the  $\varphi_i$  are angle variables. Unfortunately, one may not apply the KAM Theorem directly to Hamiltonian (I-4) since  $H_0 = J_1 + J_2$  violates Condition (ii) of that theorem. Nonetheless, we may introduce another canonical transformation,<sup>1</sup> the details of which need not concern us here, such that Hamiltonian (I-4) becomes

$$H = H_0(J_1, J_2) + V(J_1, J_2, \theta_1, \theta_2), \quad (I-5)$$

where the  $J_i$  are new momenta variables and the  $\theta_i$  are new angle variables, and where  $V$  may be written as a trigonometric series in the angle variables. Provided that the system energy is sufficiently small, we may prove that Hamiltonian (I-5) satisfies the assumptions of the KAM Theorem.

In essence, the KAM Theorem is proved by eliminating all angle dependent terms from Hamiltonian (I-5) via a convergent sequence of canonical transformations, finally bringing the Hamiltonian to the clearly integrable form

$$H = H(\bar{J}_1, \bar{J}_2). \quad (I-6)$$

In illustration of this process, let us write Hamiltonian (I-5) as

$$H = H_0(J_1, J_2) + f_{mn}(J_1, J_2) \cos(m\theta_1 - n\theta_2) + \dots, \quad (I-7)$$

where only one angle-dependent term has been explicitly written out. A typical transformation equation which would be used to eliminate this explicit angle term has the form

$$J_1' = J_1 - \frac{f_{mn}(J_1, J_2) \cos(m\theta_1 - n\theta_2)}{(m\Omega_1 - n\Omega_2)} + \dots, \quad (I-8)$$

where  $\Omega_i(J_1, J_2) \equiv \partial H_0 / \partial J_i$ . KAM Condition (i) insures that all the  $f_{mn}$

are small thereby aiding convergence of the procedure. KAM Condition (ii) insures that the  $J$ -dependent, denominators  $(m\Omega_1 - n\Omega_2)$  do not vanish identically. KAM then proceed to prove that the sequence of canonical transformations leading to Hamiltonian (I-6) converges except in those small regions of phase space where one or more of the frequency denominators  $[m\Omega_1(J_1, J_2) - n\Omega_2(J_1, J_2)]$  are small. Such denominators are called resonant-denominators and the corresponding angle-dependent, interaction terms involving  $(m\theta_1 - n\theta_2)$  are called resonant interactions. When all the  $f_{mn}$  are small, the excluded regions affected by the resonant interactions may be shown to possess small measure. However as the  $f_{mn}$  increase, the excluded resonant regions also increase in size eventually reaching the size of the allowed phase space. In particular, the excluded resonant width in phase space of each resonant interaction increases in size until the trajectories in almost every region of phase space are under the influence of many overlapping resonances. Intuitively speaking, one then has the situation envisioned in the quantum mechanical golden rule<sup>20</sup> where an initial state  $(J_1, J_2)$  makes resonant transitions to any of a density of final states  $(J'_1, J'_2)$ , leading to irreversible behavior. In analogy, one expects the classical trajectories in phase space regions containing many overlapping resonances to wander erratically over the energy surface. The validity of this conjecture is of course supported by the Henon-Heiles calculations as well as those of others.<sup>1,3,10,22</sup>

Thus using the KAM Theorem as a basis, one may assign resonance and resonance overlap a central role in the development of stochastic or freely wandering trajectories. In the example presented, resonance

and resonance overlap have an appreciable effect only when the perturbation becomes large as might occur in a solid near melting or in polyatomic molecules near dissociation. In the following sections of this thesis, we investigate the conditions under which resonance and resonance overlap can occur no matter how small the perturbation. In the final computational sections, we reconsider the nature of the statistical regions of phase space and develop an alternative view of the source of stochasticity.



## CHAPTER II

GENERAL THEORY FOR THE N-OSCILLATOR  
SYSTEM WITH SMALL NONLINEARITY

We have seen that for sufficiently large energies, the trajectories for  $N = 2$  nonlinear oscillator systems can exhibit stochastic behavior, by which we mean that such trajectories wander freely over part or all of the energy surface. We shall now show that the trajectories for a physically interesting class of  $N$ -oscillator systems can also display highly erratic behavior using even a very small nonlinear perturbation provided a violation of Condition (ii) of KAM theory occurs. In order to observe this widespread stochasticity at low energies, we investigate the classical motion of oscillator systems having the nearly-linear form

$$H = \sum_{k=1}^N \frac{\omega_k}{2} (P_k^2 + Q_k^2) + \gamma [V_3 + V_4 + \dots] . \quad (\text{II-1})$$

Here  $N$  is the number of oscillators,  $\omega_k$  are the positive frequencies of the harmonic approximation,  $\gamma$  is the nonlinear coupling parameter, and  $V_3, V_4$ , etc., are cubic, quartic, etc., polynomials in  $Q_k$  and  $P_k$ . Our intent is to expose those essential properties of Hamiltonian (II-1) which are crucial for irreversibility as the nonlinear coupling tends to zero. As in the earlier work described in the previous chapter, we shall achieve this end by focusing our attention on the individual trajectories of this nearly-linear Hamiltonian and by seeking to

determine the conditions under which most trajectories exhibit stochastic behavior.

Unfortunately, not all Hamiltonians (II-1) yield freely wandering trajectories when the perturbation term  $\gamma[V_3 + V_4 + \dots]$  is small. For example, we demonstrated in Chapter I that the Henon and Heiles Hamiltonian (I-2), which has the form of Hamiltonian (II-1), does not display stochastic behavior unless the perturbation is large. In order to determine that sub-class of Hamiltonian (II-1) which can yield stochastic trajectories when the perturbation is small, let us attempt to transform Hamiltonian (II-1) into a form for which the KAM Theorem would be valid.

First, we introduce new canonical variables  $(J_k, \varphi_k)$  defined by

$$Q_k = (2J_k)^{\frac{1}{2}} \cos \varphi_k, \quad (\text{II-2a})$$

$$P_k = -(2J_k)^{\frac{1}{2}} \sin \varphi_k; \quad k = 1, \dots, N, \quad (\text{II-2b})$$

where the  $J_k$  are the new momenta variables and the  $\varphi_k$  are the new position or angle variables. Hamiltonian (II-1) may then be written

$$H = \sum_{k=1}^N \omega_k J_k + \gamma[V_3 + V_4 + \dots], \quad (\text{II-3})$$

where  $V_3, V_4$ , etc., are each a finite sum of trigonometric terms. Let us here take  $H_0 = \sum_{k=1}^N \omega_k J_k$  as the unperturbed Hamiltonian and seek to eliminate the angle-dependent terms in  $V_3$  and  $V_4$  in the fashion indicated by Equations (I-7) and (I-8). Now  $V_3$  consists of a sum of terms each

having the form  $J_k |n_k/2| J_\ell |n_\ell/2| J_m |n_m/2| \frac{\sin(n_k \varphi_k + n_\ell \varphi_\ell + n_m \varphi_m)}{\cos(n_k \varphi_k + n_\ell \varphi_\ell + n_m \varphi_m)}$ , where  $|n_k| + |n_\ell| + |n_m| = 3$  and where here we allow  $k = \ell$  or  $k = \ell = m$ . Thus, according to Equation (I-8), we may eliminate any  $V_3$  angle-dependent term with argument  $(n_k \varphi_k + n_\ell \varphi_\ell + n_m \varphi_m)$  provided  $(n_k \omega_k + n_\ell \omega_\ell + n_m \omega_m) \neq 0$ , where  $\omega_k = \frac{\partial H_0}{\partial J_k}$ . Hence, if we require the harmonic frequencies  $\omega_k$  to be such that  $\sum n_k \omega_k \neq 0$  for every integer set  $\{n_k\}$  satisfying  $\sum |n_k| = 3$ , then Hamiltonian (II-3) can be canonically transformed to the form

$$H = \sum_{k=1}^N \omega_k J_k + \gamma [V_4 + V_5 + \dots]. \quad (\text{II-4})$$

Now  $V_4$  is a sum of terms each having the form  $J_i |n_i/2| J_k |n_k/2| \times J_\ell |n_\ell/2| J_m |n_m/2| \times \frac{\sin(n_i \varphi_i + n_k \varphi_k + n_\ell \varphi_\ell + n_m \varphi_m)}{\cos(n_i \varphi_i + n_k \varphi_k + n_\ell \varphi_\ell + n_m \varphi_m)}$ , where  $|n_i| + |n_k| + |n_\ell| + |n_m| = 4$  and where here we again allow equality of the subscripts  $i, k, \ell$ , and  $m$ . Each of these terms can be eliminated provided the corresponding frequency sum  $(n_i \omega_i + n_k \omega_k + n_\ell \omega_\ell + n_m \omega_m) \neq 0$ . However, there are pure  $J$ -terms in  $V_4$  that cannot be eliminated regardless of the arithmetic nature of the  $\omega_k$ . Since we allow equality of subscripts in the above general  $V_4$  term, we may have terms like  $J_1^2 \cos(\varphi_1 + \varphi_1 - \varphi_1 - \varphi_1) = J_1^2$ , which clearly cannot be eliminated because the corresponding frequency sum is identically zero. Nonetheless, if we also require that the harmonic frequencies are such that  $\sum n_k \omega_k \neq 0$  for every integer set  $\{n_k\}$  satisfying  $\sum |n_k| = 4$ , then Hamiltonian (II-4) can be brought to the form

$$H = \sum_{k=1}^N \omega_k J_k + \gamma \sum_{k, \ell=1}^N A_{k\ell} J_k J_\ell + \gamma [V_5 + V_6 + \dots], \quad (\text{II-5})$$

where the  $A_{k\ell}$  are constants. Now Hamiltonian (II-5) will in general satisfy the conditions of the KAM Theorem since  $H_0 = \left[ \sum_{k=1}^N \omega_k J_k + \gamma \sum_{k,\ell=1}^N A_{k\ell} J_k J_\ell \right]$  will in most cases yield a determinant  $|\partial^2 H_0 / \partial J_i \partial J_k|$  which is nonzero.

We may summarize these results by stating Arnold's version of the KAM Theorem<sup>23</sup> which specifically applies to Hamiltonian (II-1). Arnold rigorously proves that most -- in the sense of measure theory -- trajectories of Hamiltonians (II-1) lie on smooth, N-dimensional integral surfaces provided, among other things,

- (a)  $\gamma$  or, equivalently, the total energy is sufficiently small, and
- (b) the harmonic frequencies  $\omega_k$  do not satisfy low order resonance conditions of the form  $\sum n_k \omega_k = 0$  for any integer set  $\{n_k\}$  such that  $\sum |n_k| \leq 4$ .

In essence Arnold Condition (a) is equivalent to KAM Condition (i), while Arnold Condition (b) is a restatement of KAM Condition (ii) in a form applicable to nearly-linear Hamiltonians. Thus, only that subclass of Hamiltonians (II-1) which violate Arnold's Condition (b) are even candidates for yielding stochastic behavior when the nonlinear perturbation  $\gamma[V_3 + V_4 + \dots]$  is small. It is the task of this thesis to demonstrate by example that violation of Arnold's Condition (b) does indeed lead to stochastic trajectories.

In order to simplify the discussion without loss of significant generality, let us specialize to the case of resonant "three phonon" interactions for which  $\omega_k = k\omega$ , where  $\omega$  is a positive number. Here, using the action-angle variables of Equations (II-2), Hamiltonian (II-1)

may be written

$$H = \sum_{k=1}^N k \omega_k J_k + \gamma \sum_{k, \ell, m} A_{k, \ell, m} J_k |J_\ell|^{n_\ell/2} |J_m|^{n_m/2} \times \quad (\text{II-6})$$

$$\cos(n_k \varphi_k + n_\ell \varphi_\ell + n_m \varphi_m) + \gamma V,$$

where the  $A_{k, \ell, m}$  are constants, the second sum is taken over all resonant  $V_3$  interactions defined as those  $V_3$  terms with angle arguments  $\sum n_k \varphi_k$  for which  $\sum n_k \omega_k = 0$  where  $\sum |n_k| = 3$  [these are the terms which provide the violation of Arnold's Condition (b)], and  $\gamma V$  includes all nonresonant  $V_3$  terms as well as all higher order terms. If this resonant, second sum were absent from Hamiltonian (II-6), then all the remaining angle-dependent terms in  $V_3$  and  $V_4$  could be eliminated, and most system trajectories would lie on the smooth, N-dimensional integral surfaces predicted by the Arnold Theorem. Moreover, for small  $\gamma$ , the  $\gamma V$  terms would then serve only to slightly distort the N-dimensional integral surfaces of the  $\gamma = 0$  harmonic system and would thus have no appreciable effect on stochasticity. As a consequence, when  $\gamma$  is extremely small, any widespread stochastic behavior of Hamiltonian (II-6) may be determined by investigating the pure resonant Hamiltonian

$$H = \sum_{k=1}^N k \omega_k J_k + \gamma \sum_{k, \ell, m} A_{k, \ell, m} J_k |J_\ell|^{n_\ell/2} |J_m|^{n_m/2} \times \quad (\text{II-7})$$

$$\cos(n_k \varphi_k + n_\ell \varphi_\ell + n_m \varphi_m).$$

In Hamiltonian (II-7), the term  $\sum_{k=1}^N k\omega J_k$  only serves to contribute rapidly varying terms to the  $\varphi_k$ -solutions; therefore, let us seek to eliminate these terms. To this end, we introduce the time dependent, canonical transformation generated by<sup>21</sup>

$$F = \sum_{k=1}^N (\bar{J}_k) \cdot (\varphi_k - k\omega t), \quad (\text{II-8})$$

which yields the transformation

$$J_k = \bar{J}_k, \quad (\text{II-9a})$$

$$\varphi_k = \bar{\varphi}_k + k\omega t; \quad k = 1, \dots, N. \quad (\text{II-9b})$$

Substituting Equations (II-9) into Hamiltonian (II-7), we obtain

$$\mathcal{H} = \gamma \sum_{k,\ell,m} A_{k\ell m} \bar{J}_k^{n_k/2} \bar{J}_\ell^{n_\ell/2} \bar{J}_m^{n_m/2} \times \quad (\text{II-10})$$

$$\cos(n_k \bar{\varphi}_k + n_\ell \bar{\varphi}_\ell + n_m \bar{\varphi}_m),$$

where  $H = \sum_{k=1}^N k\omega \bar{J}_k + \mathcal{H}$ . We now observe that  $\gamma$  is only a multiplicative, constant factor in Hamiltonian (II-10); hence,  $\gamma$  primarily determines only the time scale of the motion. As a consequence, any widespread stochasticity which occurs for Hamiltonian (II-10) or the equivalent Hamiltonian (II-7) will continue to occur no matter how small the value of  $\gamma$ , excluding  $\gamma = 0$  of course.

As discussed earlier in the Introduction, it is known that

wandering trajectories associated with stochastic motion for large  $\gamma$  are found when there is multiple resonance overlap. Since each resonant term in Hamiltonian (II-7) strongly influences every trajectory, one has that complete, multiple resonance overlap anticipated to cause violent stochasticity. The effect of overlapping resonances is to destroy most of the smooth integral surfaces predicted by the Arnold Theorem, thus allowing each system trajectory to range widely over the energy surface. For the pure resonant Hamiltonian (II-7) however,  $\sum_{k=1}^N k\omega_k$  is a constant of the motion in addition to the Hamiltonian itself. Thus each system trajectory can at best be stochastic only on a  $(2N-2)$ -dimensional subspace of the  $(2N-1)$ -dimensional energy surface. For  $N = 2$  then, Hamiltonian (II-7) is no more stochastic than a pure harmonic system with  $N = 2$ . As  $N$  becomes greater than 2 however, an increasing percentage of the energy surface can be reached and a striking increase in stochasticity is anticipated.

In order to demonstrate that widespread stochasticity does indeed occur for low order resonant systems, the following two chapters describe a detailed investigation of Hamiltonian (II-7) for the case  $N = 3$ , which is especially interesting since it should exhibit the minimum stochasticity to be expected for low order resonant systems. Before concluding this discussion of the general case with  $N$  oscillators, it is worth emphasizing that classical systems<sup>1,5-15</sup> can exhibit statistical mechanical behavior without invoking the traditional limit of  $N \rightarrow \infty$ . We have already seen in the Introduction that the  $N = 2$  system of Henon and Heiles<sup>7</sup> shows widespread stochasticity for large non-linearity. We shall demonstrate widespread stochasticity with small

nonlinearity using  $N = 3$ . Sinai<sup>24</sup> has rigorously proved that a hard sphere gas system is stochastic when the number of particles is two or greater. Thus, analytic studies of relatively small systems, aided by computers, may be able to contribute significantly to contemporary statistical mechanics.



## CHAPTER III

STOCHASTICITY FOR  $N = 3$  AND  $\gamma = 1$ 

We demonstrate by example in this chapter that a pure resonant, nearly-linear, three-oscillator system can exhibit widespread stochasticity when there are low order resonant terms present in the Hamiltonian which link all degrees of freedom. For the case  $N = 3$  and  $\omega = 1$ , Hamiltonian (II-7) becomes

$$H = J_1 + 2J_2 + 3J_3 + \sqrt{\alpha J_1 J_2}^{\frac{1}{2}} \cos(2\varphi_1 - \varphi_2) + \quad (\text{III-1})$$

$$\beta (J_1 J_2 J_3)^{\frac{1}{2}} \cos(\varphi_1 + \varphi_2 - \varphi_3),$$

since there are only two resonant perturbation terms for  $N = 3$ , where we defined a resonant term in Chapter II to be one which violates Condition (b) of the Arnold Theorem. The ratio of the unperturbed frequencies (1:2:3) in the  $H_0$  term is chosen to simulate the linear acoustic region of the dispersion curve for solids, while the two cosine terms represent the overlapping, resonant, three-phonon interactions  $2\omega_1 \rightleftharpoons \omega_2$  and  $(\omega_1 + \omega_2) \rightleftharpoons \omega_3$  respectively; i.e., the pure resonant Hamiltonian (III-1) is a very simple model of a solid.

In Hamiltonian (III-1) the only effect of the terms linear in  $J$  is to cause a relatively rapid change with time of the angle variables. We may eliminate this rapid angle change along with the linear  $J$ -terms

by transforming to a rotating coordinate system using the transformation generated by Equation (II-8). We then obtain

$$\mathcal{K} = \gamma \left[ \alpha \bar{J}_1 \bar{J}_2^{\frac{1}{2}} \cos(2\bar{\varphi}_1 - \bar{\varphi}_2) + \beta (\bar{J}_1 \bar{J}_2 \bar{J}_3)^{\frac{1}{2}} \cos(\bar{\varphi}_1 + \bar{\varphi}_2 - \bar{\varphi}_3) \right], \quad (\text{III-2})$$

where  $H = (\bar{J}_1 + 2\bar{J}_2 + 3\bar{J}_3) + \mathcal{K}$ . We may now eliminate  $\gamma$  by canonically transforming the time variable to  $\tau = \gamma t$ , obtaining<sup>36</sup>

$$K = \alpha \bar{J}_1 \bar{J}_2^{\frac{1}{2}} \cos(2\bar{\varphi}_1 - \bar{\varphi}_2) + \beta (\bar{J}_1 \bar{J}_2 \bar{J}_3)^{\frac{1}{2}} \cos(\bar{\varphi}_1 + \bar{\varphi}_2 - \bar{\varphi}_3), \quad (\text{III-3})$$

where  $H = (\bar{J}_1 + 2\bar{J}_2 + 3\bar{J}_3) + \gamma K$ . Clearly we could also eliminate either  $\alpha$  or  $\beta$  by again changing the time scale, making  $K$  depend only on the ratio  $(\alpha/\beta)$ ; instead, we somewhat arbitrarily fix  $\beta$  in all calculations at  $\beta = 0.4$  and vary the  $(\alpha/\beta)$  ratio by changing  $\alpha$ .

Now from the definition of the resonant angle-dependent terms in Hamiltonian (III-3), it can be shown that  $(\bar{J}_1 + 2\bar{J}_2 + 3\bar{J}_3)$  is a constant of the motion. It is thus convenient to canonically transform to coordinates in which  $(\bar{J}_1 + 2\bar{J}_2 + 3\bar{J}_3)$  is one of the momenta. This may be accomplished using the canonical transformation generated by

$$F = (J_1 - 2J_2 - 3J_3)\bar{\varphi}_1 + J_2\bar{\varphi}_2 + J_3\varphi_3, \quad (\text{III-4})$$

from which we obtain the new Hamiltonian form

$$K = \alpha (J_1 - 2J_2 - 3J_3) J_2^{\frac{1}{2}} \cos \theta_2 + \beta [J_2 J_3 (J_1 - 2J_2 - 3J_3)]^{\frac{1}{2}} \times \cos(\theta_2 - \theta_3), \quad (\text{III-5})$$

where  $H = J_1 + \gamma K$ . Since  $J_1$  is a constant of the motion and since Hamiltonian (III-5) does not depend on  $\theta_1$ , we have in effect split the original six-dimensional phase space into an independent product of a two-dimensional  $(J_1, \theta_1)$  space and a four-dimensional  $(J_2, J_3, \theta_2, \theta_3)$  space.

In particular, we may regard Hamiltonian (III-5) as describing the motion of a system whose trajectories move only in the four-dimensional  $(J_2, J_3, \theta_2, \theta_3)$  space, treating  $J_1$  as merely a parameter like  $\alpha$  or  $\beta$ . Thus, we may canonically transform Hamiltonian (III-5), which represents a system with two degrees of freedom, to rectangular coordinates and survey the nature of the trajectories for the rectangular Hamiltonian by the surface of section technique described in the Introduction. Using the canonical transformation (I-3) in Hamiltonian (III-5), we obtain

$$K = (\alpha/\sqrt{2})q_2 A + (\beta/2)(q_2 q_3 + p_2 p_3)A^{\frac{1}{2}}, \quad (\text{III-6a})$$

where

$$A = J_1 - (q_2^2 + p_2^2) - (3/2)(q_3^2 + p_3^2), \quad (\text{III-6b})$$

and

$$H = J_1 + \gamma K. \quad (\text{III-6c})$$

When the values of  $H$ ,  $J_1$ , and  $\gamma$  are specified, Hamiltonian (III-6a) becomes a constant of the motion, and we can plot trajectories in the

three-space  $(q_2, q_3, p_3)$ , since  $p_2$  can be determined from Equation (III-6a). We then choose the  $(q_3, p_3)$  plane as the surface of section and plot the set of points representing trajectory intersections with this plane (that is, those  $(q_3, p_3)$  points on a trajectory for which  $q_2 = 0$  and  $p_2 \geq 0$ ), which will indicate the amount of stochasticity present in the associated regions of phase space. When the phase space motion takes place on two-dimensional integral surfaces, the intersection points of the trajectories with the  $q_3 p_3$  plane form a smooth curve; conversely, in those regions of phase space where the motion is stochastic, the trajectories wander more or less randomly over some or most of the allowed  $(q_2, q_3, p_3)$  space and a set of scattered points is seen in the surface of section.

We further observe that all the allowed points in the  $(q_3, p_3)$  plane must lie on or within a simple closed curve called the bounding curve, since, from the equation for the constant of the motion  $J_1$  given by

$$J_1 = J_1 + (q_2^2 + p_2^2) + (3/2)(q_3^2 + p_3^2), \quad (\text{III-7})$$

we see that  $J_1$  must be positive definite. The bounding curve equation is obtained by the following scheme. We consider Equation (III-6a) written for  $q_2 = 0$ , which becomes

$$K = (\beta/2)p_2 p_3 \left[ \{J_1 - (3/2)(q_3^2 + p_3^2)\} - p_2^2 \right]^{1/2}. \quad (\text{III-8})$$

Substituting Equation (III-8) into Equation (III-6c) and solving for  $p_2$ , we obtain the quadratic-quartic equation in  $p_2$  given by

$$p_2^4 - [J_1 - (3/2)(q_3^2 + p_3^2)]p_2^2 + \left[ \frac{4(H-J_1)^2}{\sqrt{2}\beta^2 p_3^2} \right] = 0. \quad (\text{III-9})$$

Using the property that the discriminant must be real when Equation (III-9) is solved for  $p_2$  and invoking the positive definiteness of  $J_1$  from Equation (III-7), we find the equation for the bounding curve in the  $q_3 p_3$  plane to be

$$q_3^2 = (2/3)J_1 - p_3^2 - \frac{8(H-J_1)}{3\sqrt{2}\beta p_3}, \quad (\text{III-10})$$

where we take  $J_1 < H$ .

In order to illustrate the extent to which Hamiltonian (III-6) exhibits widespread stochastic behavior, we first present some typical level curve or surface of section diagrams and then summarize the results of a broad survey of representative level curve diagrams. These level curve plots were obtained by integrating the rectangular coordinate version of Hamiltonian (III-3) and determining the corresponding solution to Hamiltonian (III-6) using the connecting, canonical transformation. In particular, we first took the full six-space Hamiltonian (III-3) and transformed it to rectangular coordinates via

$$Q_i = (2\bar{J}_i)^{\frac{1}{2}} \cos \bar{\varphi}_i, \quad (\text{III-11a})$$

$$P_i = -(2\bar{J}_i)^{\frac{1}{2}} \sin \bar{\varphi}_i; \quad i = 1, 2, 3. \quad (\text{III-11b})$$

The resulting six-space rectangular Hamiltonian is a cubic polynomial given by

$$K = (\sqrt{2}/4) \{ \alpha [ Q_1^2 Q_2 - p_1^2 Q_2 + 2 Q_1 p_1 p_2 ] + \quad (III-12)$$

$$\beta [ Q_1 Q_2 Q_3 - p_1 p_2 Q_3 + p_1 Q_2 p_3 + Q_1 p_2 p_3 ] \},$$

where

$$H = ( \bar{J}_1 + 2 \bar{J}_2 + 3 \bar{J}_3 ) + \gamma K = J_1 + \gamma K. \quad (III-13)$$

The trajectories used to develop the level curve diagrams were then obtained by integrating Hamilton's differential equations for Hamiltonian (III-12). The rotational relationships between the full six-space coordinates  $(Q_i, P_i)$  and the reduced four-space coordinates  $(q_k, p_k)$  are given by

$$\begin{bmatrix} q_2 \\ p_2 \end{bmatrix} = \begin{bmatrix} \cos 2\bar{\varphi}_1 & -\sin 2\bar{\varphi}_1 \\ \sin 2\bar{\varphi}_1 & \cos 2\bar{\varphi}_1 \end{bmatrix} \begin{bmatrix} Q_2 \\ P_2 \end{bmatrix}, \quad (III-14a)$$

$$\begin{bmatrix} q_3 \\ p_3 \end{bmatrix} = \begin{bmatrix} \cos 3\bar{\varphi}_1 & -\sin 3\bar{\varphi}_1 \\ \sin 3\bar{\varphi}_1 & \cos 3\bar{\varphi}_1 \end{bmatrix} \begin{bmatrix} Q_3 \\ P_3 \end{bmatrix}, \quad (III-14b)$$

where

$$\bar{\varphi}_1 = \tan^{-1}(-P_1/Q_1). \quad (III-14c)$$

Having finished this preliminary discussion of the procedures followed in evolving the trajectories for this pure resonant, three-oscillator system, we now consider the nature of the resulting level curve diagrams. We first set the values of  $K$  and  $J_1$  to determine the four-space Hamiltonian (III-6) and then selected a set of  $(q_3, p_3)$  points as initial data from which we evolved the trajectories used to generate the level curve diagrams. For each  $(K, J_1, q_2 = 0, p_2 \geq 0, q_3, p_3)$  set, Equation (III-9) gives two values for  $p_2$  that satisfy the energy condition of Equation (III-8), which indicates that two level curves can pass through each  $(q_3, p_3)$  point. However, when  $K$  and  $J_1$  are specified, all level curves for Hamiltonian (III-6) occupy only a half-plane. This can be seen most clearly from Equation (III-8) which shows that the level curve plane conditions  $q_2 = 0, p_2 > 0$  require that  $p_3 > 0$  in all cases, since we elect to take both  $K$  and  $\beta$  positive, and a half-plane results. Thus, in order to study the behavior of both branches, we chose to take  $p_3$  positive on both sides of the origin and plotted the level curves initiating on one  $p_2$  branch in the upper half-plane and those commencing with the second  $p_2 > 0$  branch in the lower half-plane.

Figure 4 shows a typical level curve plane containing about 70 percent smooth curves. Here  $J_1 = 2.999$ ,  $K = 0.001$ , and  $\alpha = 0.1$ . As mentioned earlier, in all calculations  $\beta$  is fixed at the value 0.4. Level curves initiating from the same seven  $(q_3, p_3)$  points appear in both upper and lower half-planes with those in the upper half-plane initiating from one  $p_2$  branch while those in the lower half-plane initiate from the other  $p_2$  branch. Figure 5 is a continuation of Figure 4 using only two  $(q_3, p_3)$  starting points. In the upper as well as the

1 Tick = 0.5

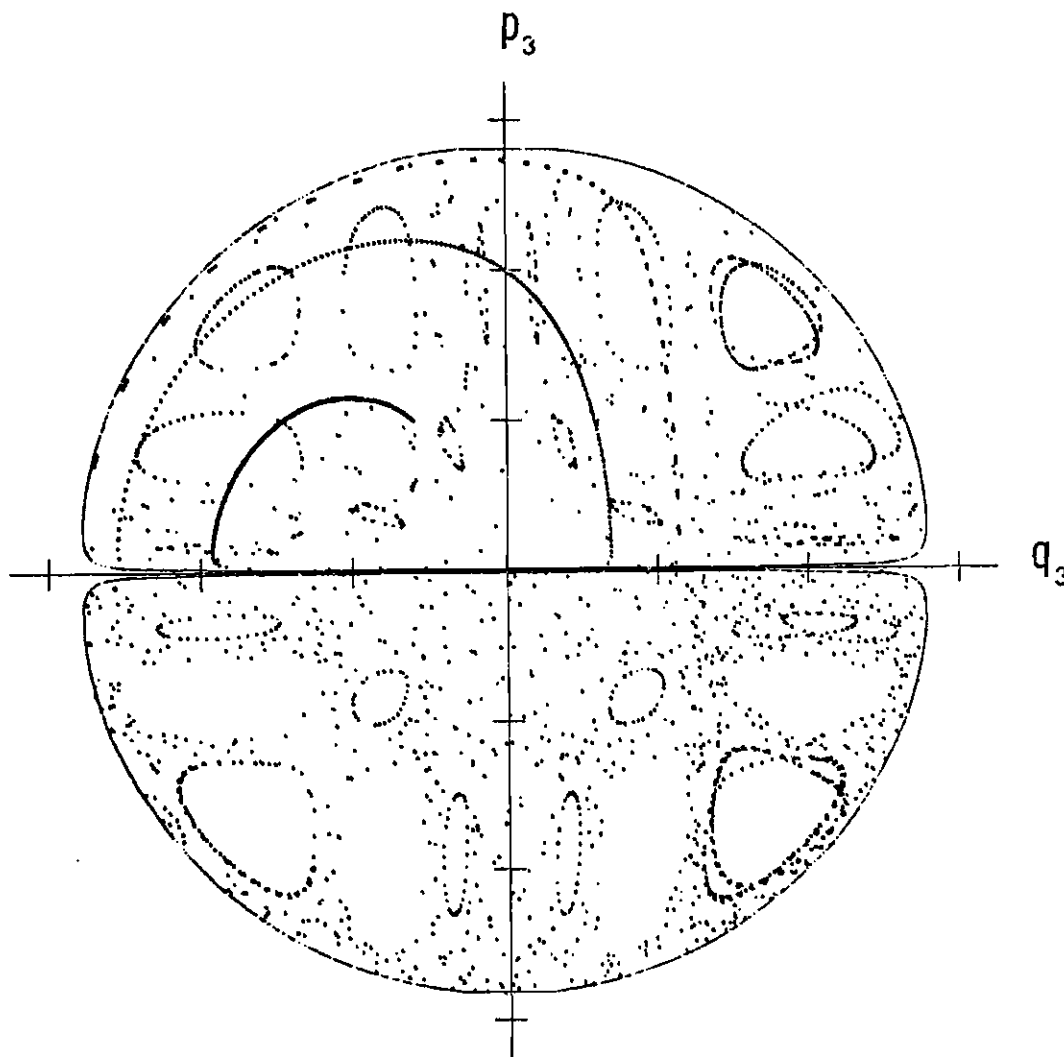


Figure 4. Level Curves for Hamiltonian (III-6) with  $H = 3.00$ ,  $J_1 = 2.999$ ,  $K = 0.001$ , and  $\alpha = 0.100$  for Seven Starting Points. (This plane contains about 70 percent smooth curves. For given  $(q_3, p_3)$  in the plane,  $p_2$  is double valued and two level curves can pass through each  $(q_3, p_3)$  point. Each level curve in the upper half-plane is started on one  $p_2$  branch, while those in the lower half-plane start on the other  $p_2$  branch. Here  $p_3$  is positive on both sides of the origin. The smooth, outermost curve in all figures is the bounding curve which encloses all allowed  $(q_3, p_3)$  points.)



1 Tick = 0.5

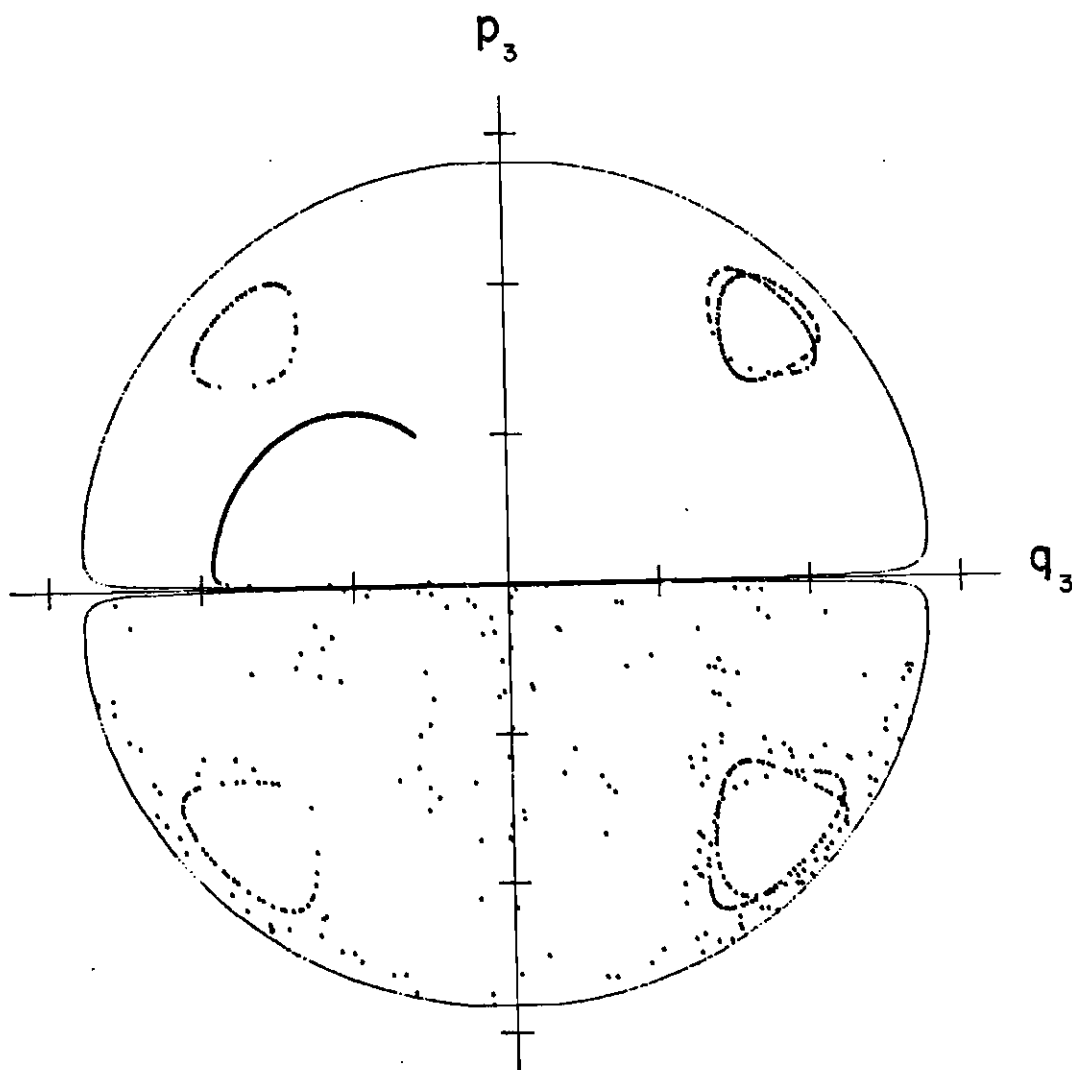


Figure 5. Level Curves for Hamiltonian (III-6) with  $H = 3.00$ ,  $J_1 = 2.999$ ,  $K = 0.001$ , and  $\alpha = 0.100$  for Two Starting Points. (This figure is a continuation of Figure 4.)

1 Tick = 0.5

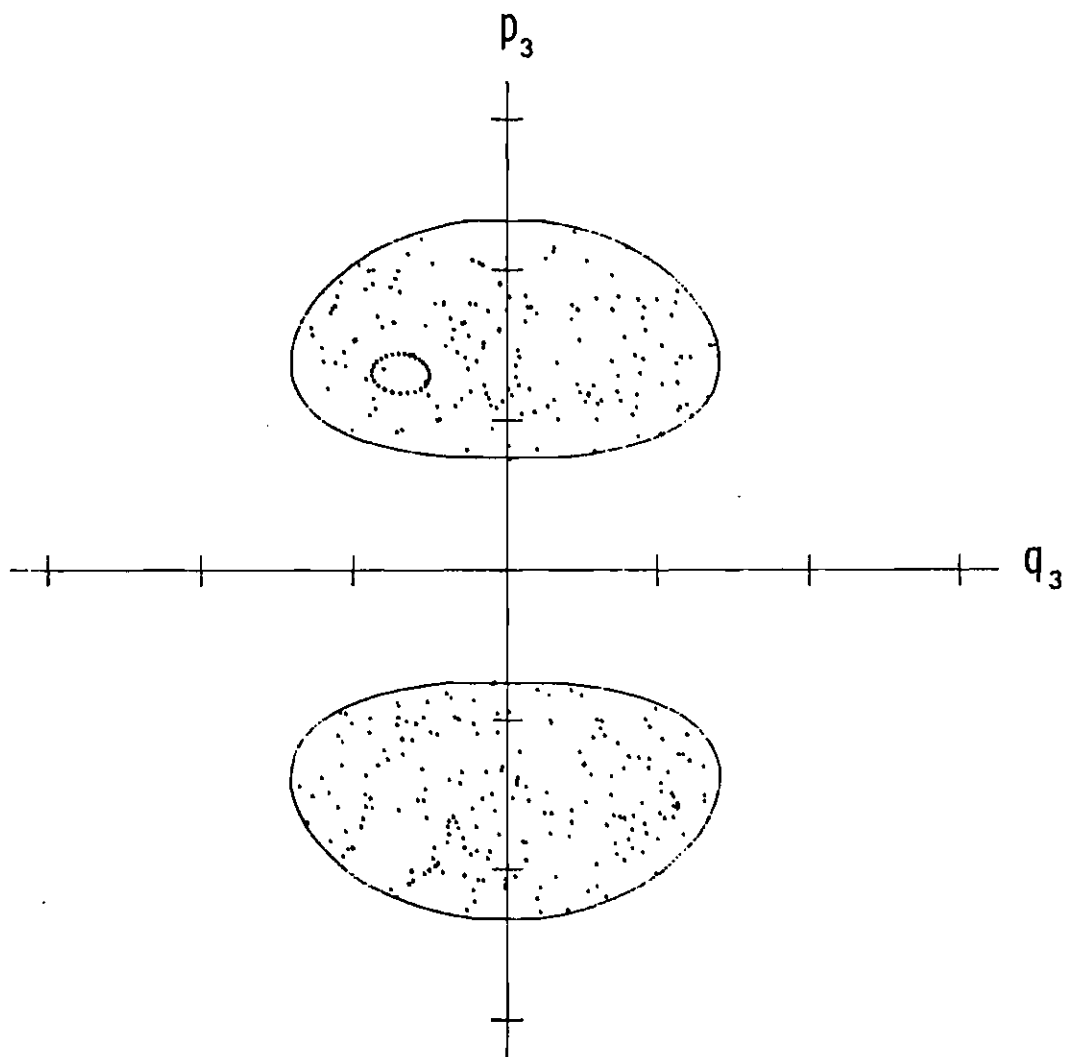


Figure 6. Level Curves for Hamiltonian (III-6) with  $H = 3.00$ ,  $J_1 = 2.901$ ,  $K = 0.099$ , and  $\alpha = 0.100$  for Five Starting Points. (The same five  $(q_3, p_3)$  starting points are used in both upper and lower half-planes. This plane contains only about 10 percent smooth curves.)

1 Tick = 0.5

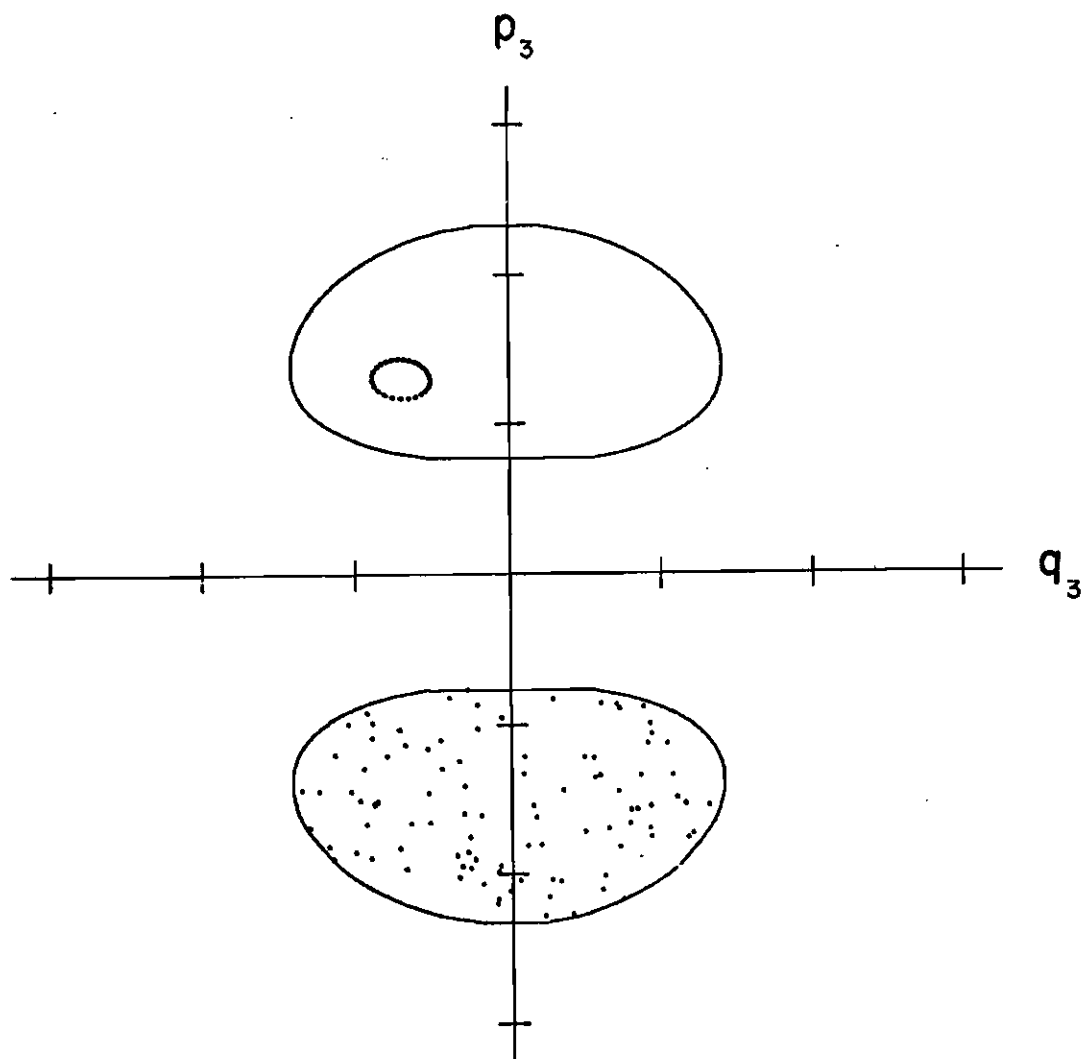


Figure 7. Level Curves for Hamiltonian (III-6) with  $H = 3.00$ ,  $J_1 = 2.901$ ,  $K = 0.099$ , and  $\alpha = 0.100$  for One Starting Point. (This figure is a continuation of Figure 6 using only one  $(q_3, p_3)$  starting point in upper and lower half-planes and integrating the trajectories for a longer time period.)

1 Tick = 0.5

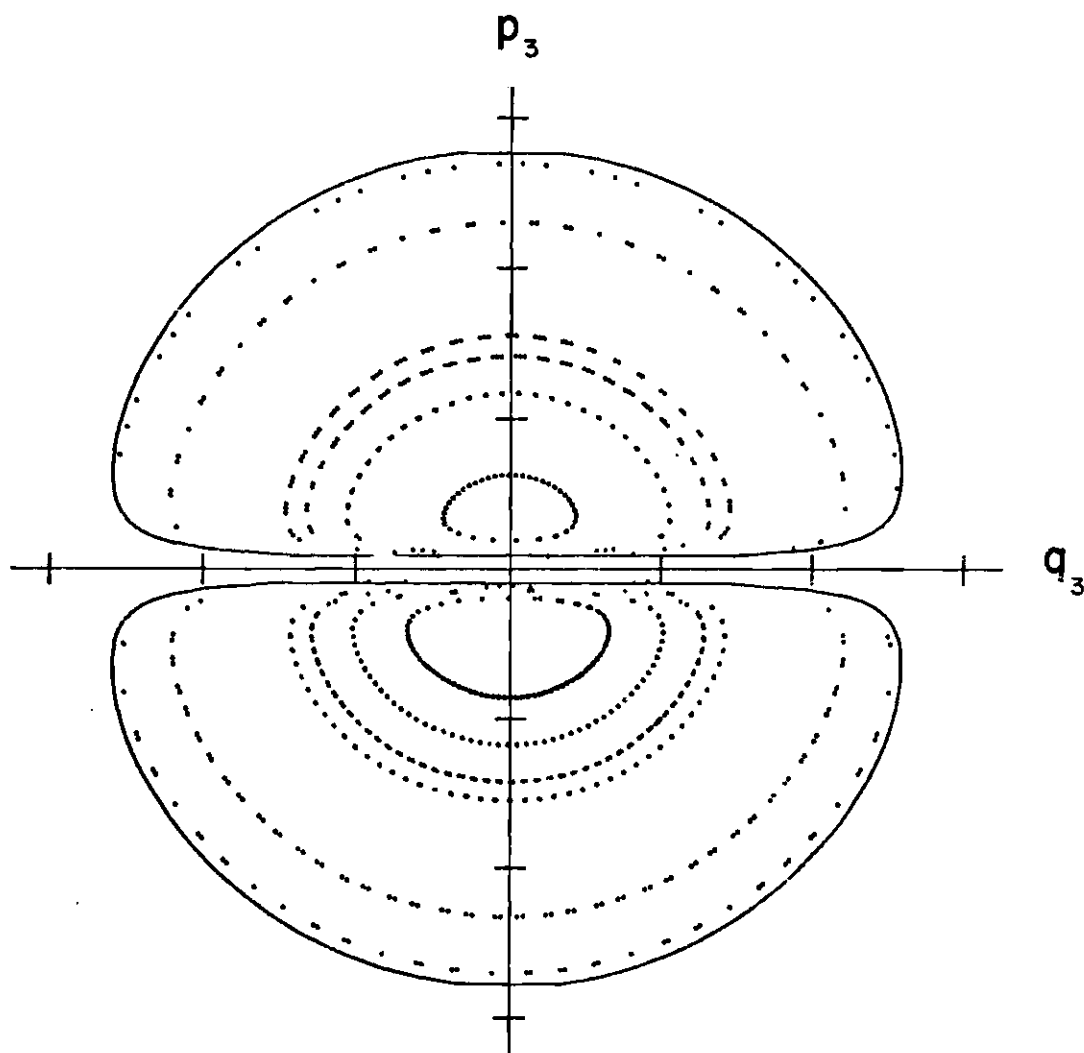


Figure 8. Level Curves for Hamiltonian (III-6) with  $H = 3.00$ ,  $J_1 = 2.990$ ,  $K = 0.010$ , and  $\alpha = 0.000$  for Six Starting Points. (This plane contains 100 percent smooth curves. The same six starting points are used in both upper and lower half-planes. This figure is the first in a sequence of five showing the change in level curve pattern as only  $\alpha$  is varied.)

1 Tick = 0.5

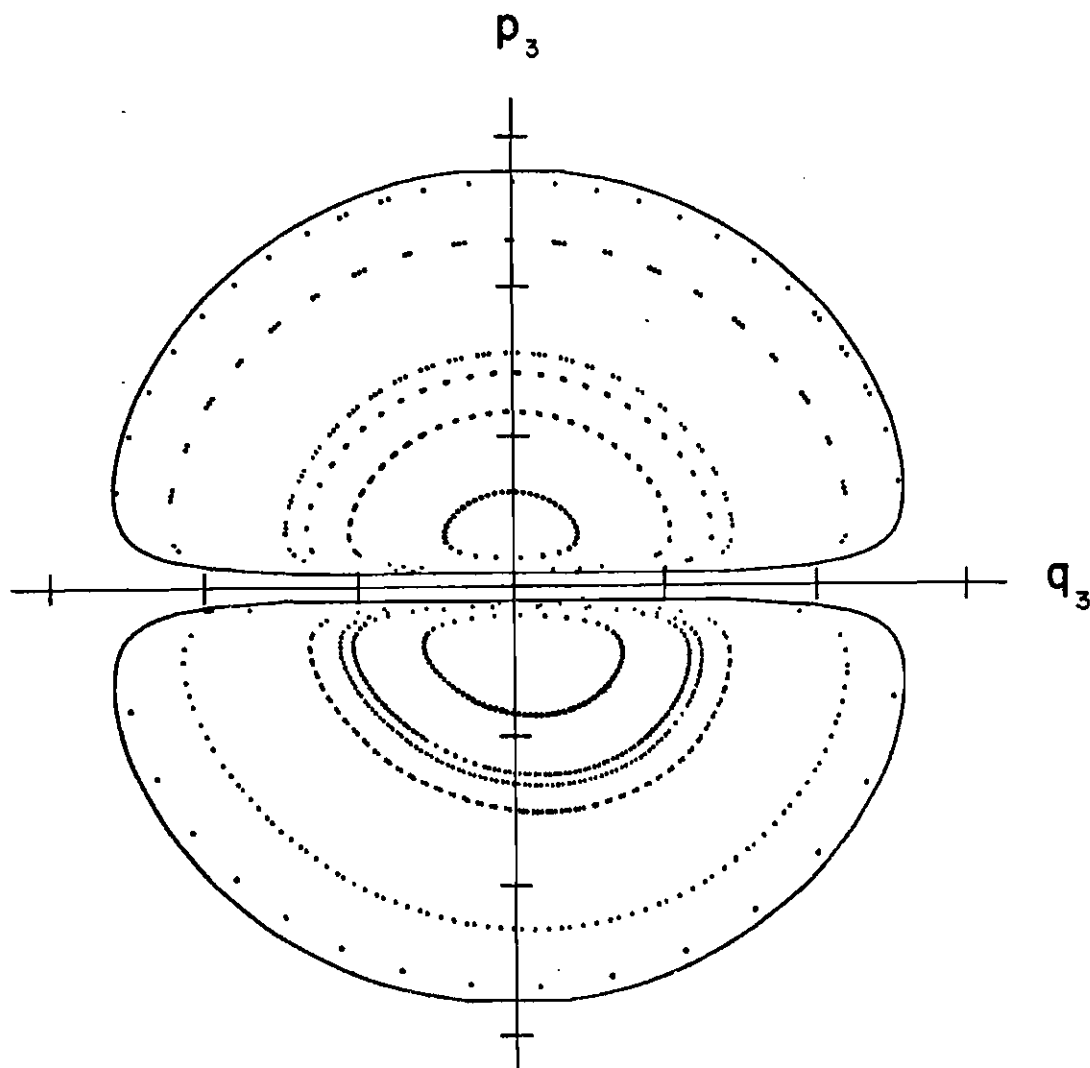


Figure 9. Level Curves for Hamiltonian (III-6) with  $H = 3.00$ ,  $J_1 = 2.990$ ,  $K = 0.010$ , and  $\alpha = 0.001$  for Six Starting Points. (There is only a slight distortion of the Figure 8 curves for this value of  $\alpha$ .)

1 Tick = 0.5

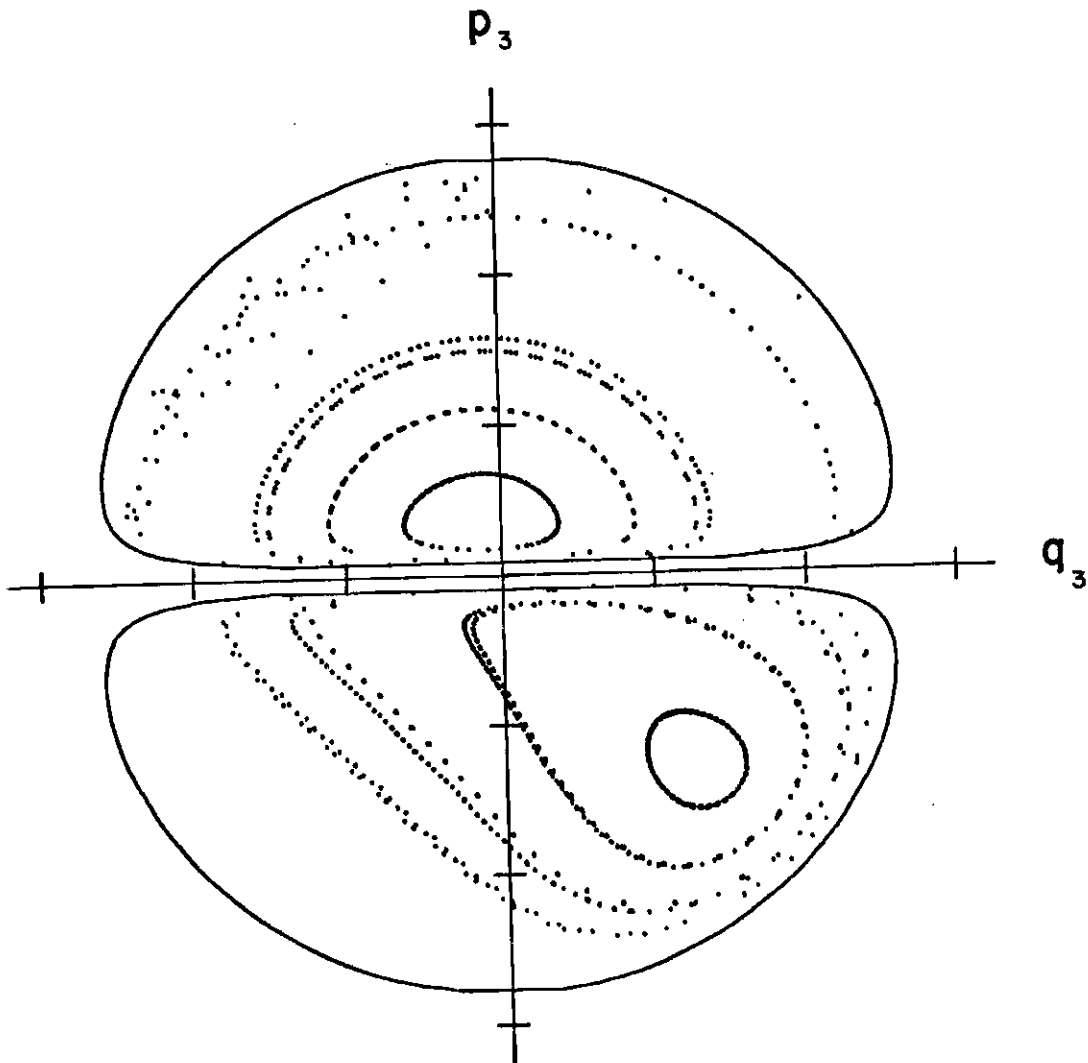


Figure 10. Level Curves for Hamiltonian (III-6) with  $H = 3.00$ ,  $J_1 = 2.990$ ,  $K = 0.010$ , and  $\alpha = 0.010$  for Six Starting Points. (This level curve plane continues the sequence begun in Figure 8. Increasing distortion occurs in the lower half-plane, and beginning stochasticity appears in both half-planes.)

1 Tick = 0.5

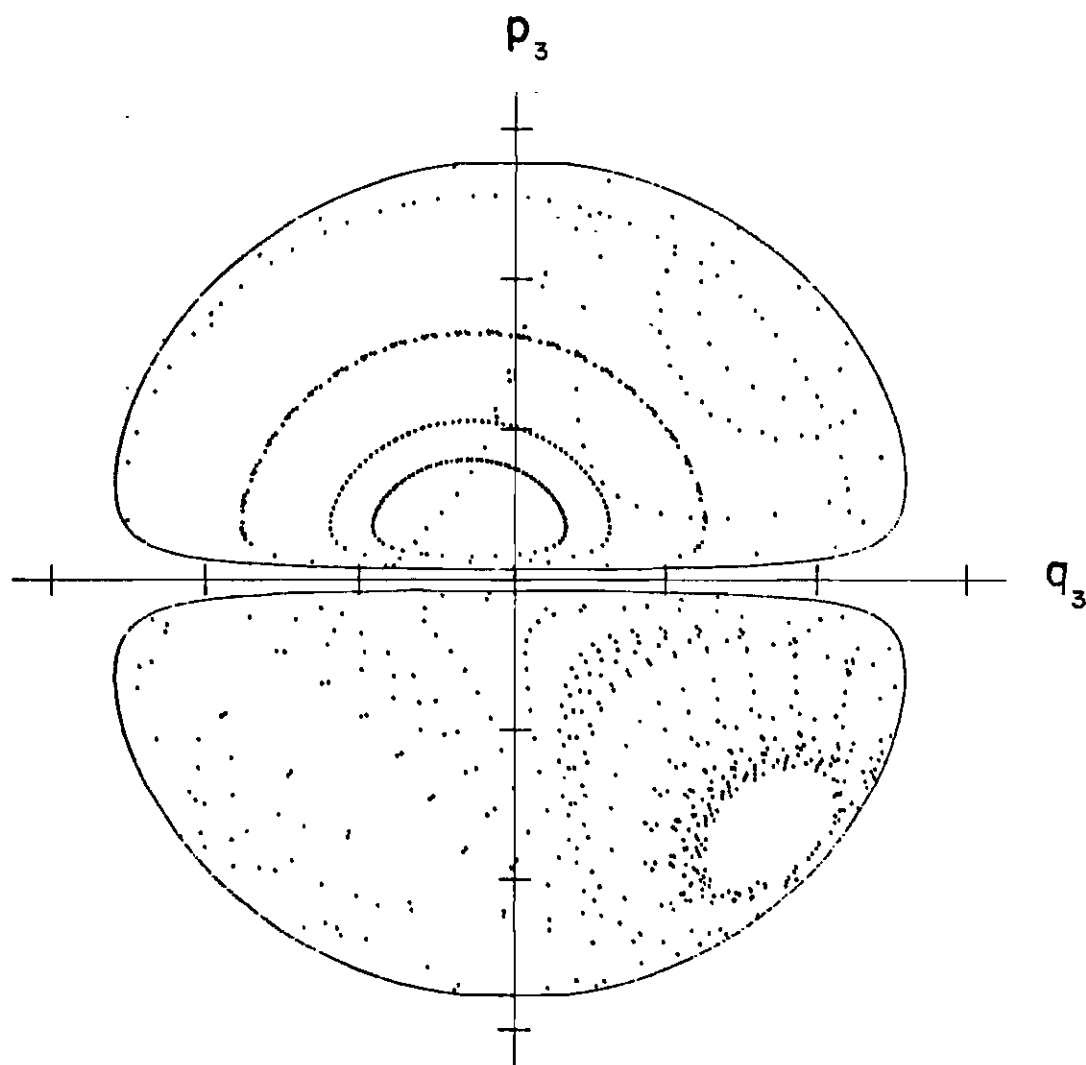


Figure 11. Level Curves for Hamiltonian (III-6) with  $H = 3.00$ ,  $J_1 = 2.990$ ,  $K = 0.010$ , and  $\alpha = 0.025$  for Six Starting Points. (This is the fourth figure in the sequence begun in Figure 8.)

1 Tick = 0.5

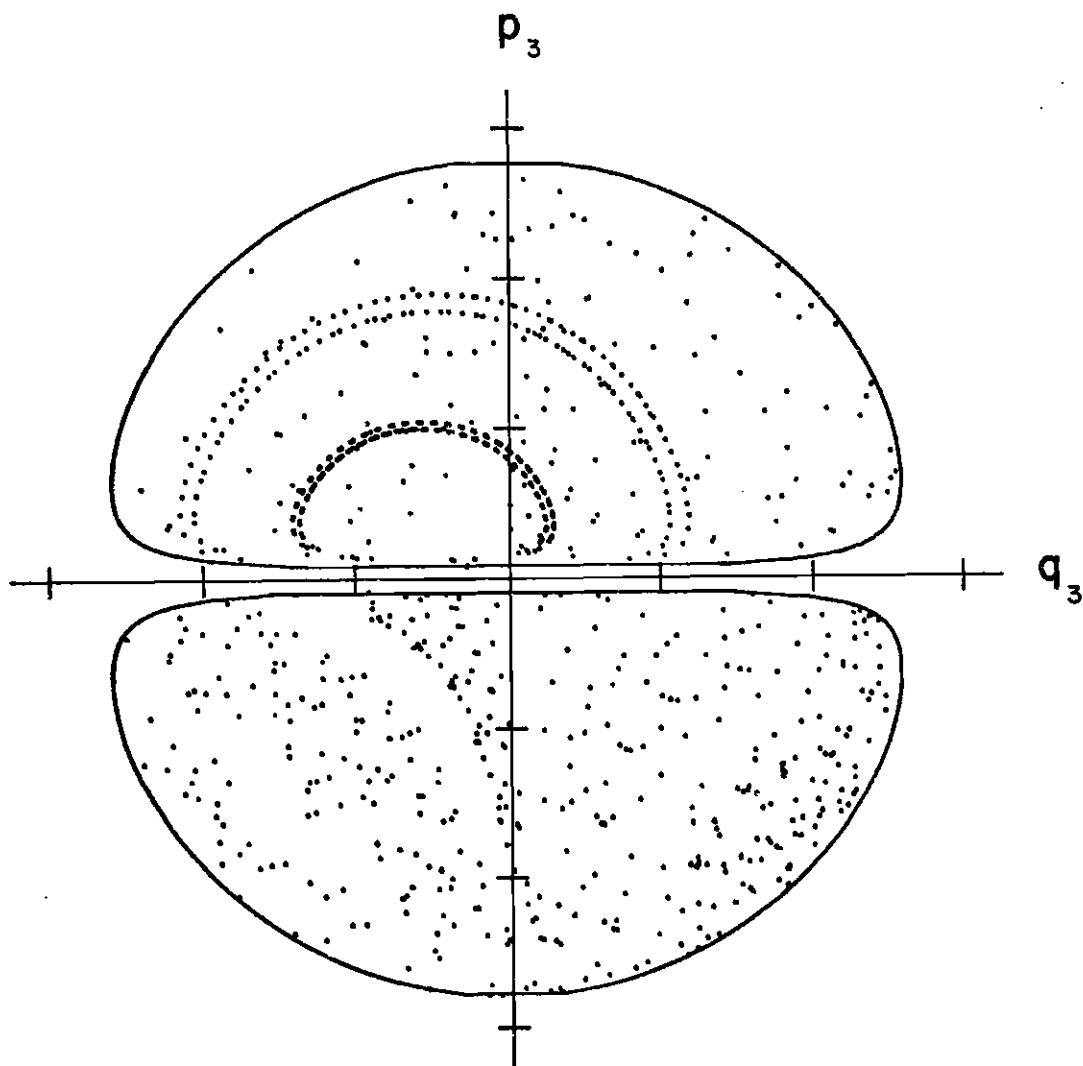


Figure 12. Level Curves for Hamiltonian (III-6) with  $H = 3.00$ ,  $J_1 = 2.990$ ,  $K = 0.010$ , and  $\alpha = 0.050$  for Six Starting Points. (This is the final level curve plane in the sequence begun in Figure 8. This plane contains about 50 percent smooth level curves.)



1 Tick = 0.5

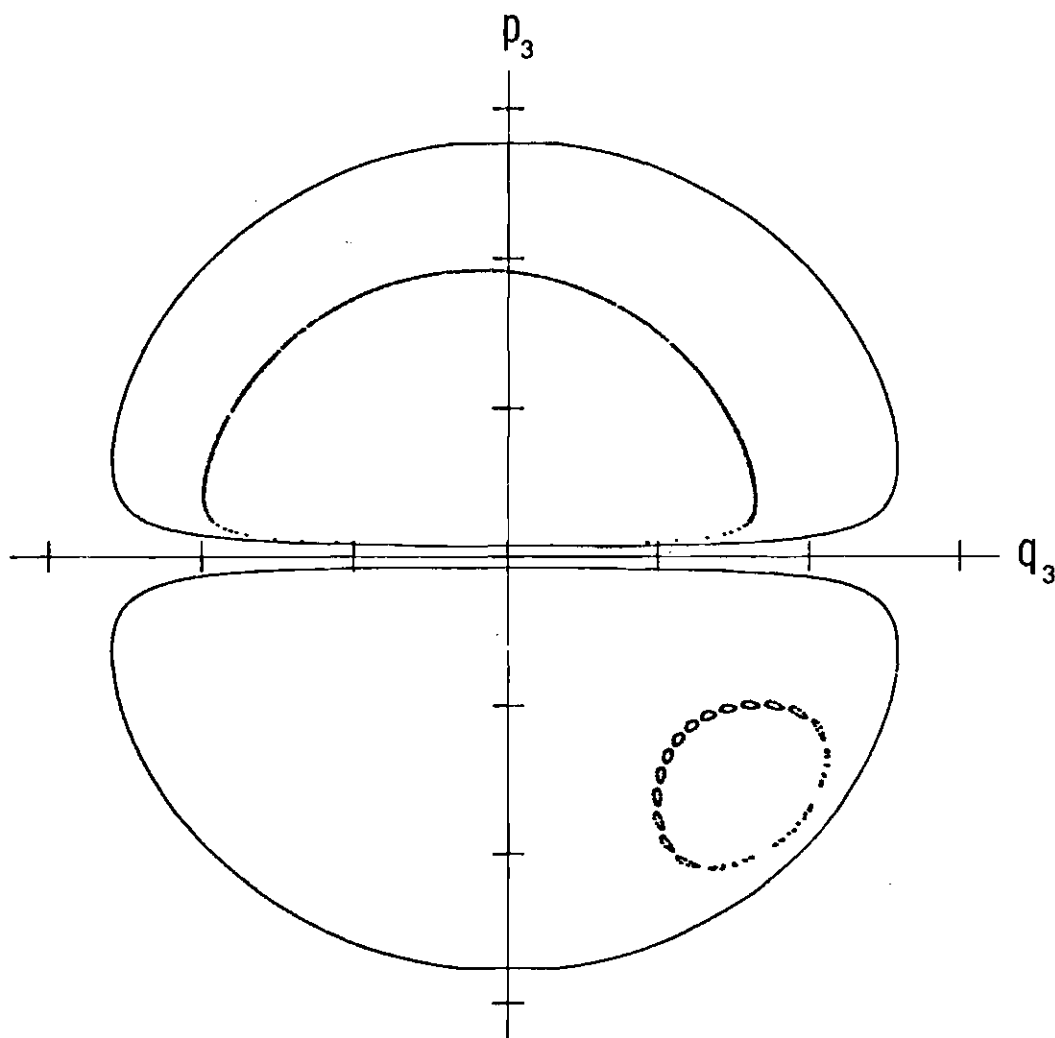


Figure 13. Level Curves for Hamiltonian (III-6) with  $H = 3.00$ ,  $J_1 = 2.990$ ,  $K = 0.010$ , and  $\alpha = 0.0185$  for One Starting Point. (Note the very unstable chain of islands in the fourth quadrant. The values of  $H$ ,  $J_1$ , and  $K$  from Figure 8 are used here.)

lower half-plane of Figure 5, the three small closed ovals represent a single level curve issuing from one of the  $(q_3, p_3)$  points. The other  $(q_3, p_3)$  initial point yields both the incomplete, smooth level curve in the second quadrant of the upper half-plane and the highly stochastic orbit of the lower half-plane. Figure 6 shows a typical level curve plane containing only about 10 percent smooth curves. Here  $J_1 = 2.901$ ,  $K = 0.099$ , and  $\alpha = 0.1$ , and the same five starting points are used in upper and lower half-planes. Figure 7 is a continuation of Figure 6 using only one  $(q_3, p_3)$  starting point and integrating the resulting two trajectories for a longer time period.

Next Figures 8-12 show a sequence of level curve planes that illustrate the change in stochastic behavior as the  $(\alpha/\beta)$  ratio is changed by varying  $\alpha$ . In each figure of this sequence,  $J_1 = 2.990$ ,  $K = 0.010$ , and the same six  $(q_3, p_3)$  starting points are used. Figure 8 is for  $\alpha = 0$ , in which case Hamiltonian (III-6) is integrable<sup>25</sup> and all trajectories yield smooth level curves. In Figure 9 for  $\alpha = 0.001$ , the upper half-plane is only slightly distorted, while the lower half-plane has noticeable deviation from the  $\alpha = 0$  curves. Figure 10 for  $\alpha = 0.010$  shows increasing distortion in the lower half-plane and beginning stochasticity in upper and lower half-planes. Figure 11 for  $\alpha = 0.025$  shows the lower half-plane on the verge of the almost complete stochasticity shown in Figure 12 for  $\alpha = 0.050$ . The plane in Figure 12 contains only about 50 percent smooth curves. As  $\alpha$  increases, a maximum percentage of about 65 percent stochastic trajectories is found to occur around  $\alpha = 0.100$ . When  $\alpha$  becomes very large, one in effect approaches the case  $\beta = 0$  for which Hamiltonian (III-6) is integrable<sup>25</sup> and all

trajectories again yield smooth level curves. Figure 13 shows a type of island structure in the fourth quadrant, which frequently develops in the transition from smooth level curves to stochastic behavior for a given region. The sensitivity of Hamiltonian (III-6) to small changes in  $\alpha$  can be seen by a comparison of Figure 13 with Figures 11 and 12.

We perhaps should emphasize that all level curve diagrams for given  $K$  and  $J_1$  in Hamiltonian (III-6) are invariant with respect to  $\gamma$ . In particular, the highly stochastic orbits exhibited in some of the diagrams are invariant as  $\gamma$  tends to zero. As seen from Equation (III-6c) however, the value of  $H$  to be associated with a particular level curve plane does depend on  $\gamma$ , since a given level curve plane is determined by specifying the values of  $K$  and  $J_1$ . Conversely, if one desires to determine the amount of widespread stochasticity in a representative sampling of  $(K, J_1)$  level curve planes allowed for a given value of  $H$ , then the value of  $\gamma$  must be fixed. In this chapter we estimate stochasticity for fixed  $H$  using  $\gamma = 1$ , while in Chapter IV we make the same estimate as  $\gamma$  tends to zero and obtain almost the same result. Thus for small  $\gamma$ , stochasticity depends only very weakly on  $\gamma$ . Moreover, since changing  $H$  is equivalent to changing  $\gamma$ , stochasticity also depends only weakly on the particular value of  $H$  used. In short, stochasticity for Hamiltonian (III-1) or (III-6) depends primarily upon  $J_1$  and  $(\alpha/\beta)$ . For calculational convenience we set  $H = 3.0$ ,  $\gamma = 1$ , and  $\beta = 0.4$ .

Table 1 gives the percentage of trajectories for Hamiltonian (III-6) that are widely stochastic for a representative sampling of  $J_1$  and  $(\alpha/\beta)$  ratios. In particular, the numbers in Table 1 indicate the

Table 1. Percentage of Stochastic Trajectories for Hamiltonian (III-1) with  $H = 3.00$  and  $\gamma = 1$ . (The trajectories lie on the four-dimensional space allowed by fixed  $H$  and  $J_1$  as a function of  $J_1$  and  $(\alpha/\beta)$ . Percentages are rounded to the nearest whole number.  $J_1$  decreases reading down and  $(\alpha/\beta)$  increases reading across the table.)

		$\alpha/\beta$								$\beta/\alpha$							
$J_1$	0	1/8	2/8	3/8	4/8	5/8	6/8	7/8	8/8	7/8	6/8	5/8	4/8	3/8	2/8	1/8	0
2.999	0	30	27	19	16	17	11	12	5	5	5	8	5	9	10	20	0
2.985	0	52	61	61	52	41	29	15	6	11	9	7	9	11	0	0	0
2.968	0	50	61	71	75	65	48	11	7	11	9	0	0	1	0	0	0
2.947	0	52	68	72	81	76	39	0	0	0	0	0	0	0	0	0	0
2.921	0	51	82	72	45	16	1	0	0	0	0	0	0	0	0	0	0
Average over $J_1$	0	47	60	60	54	43	25	8	4	5	4	3	3	4	2	4	0

amount of stochasticity in the full four-dimensional space allowed by fixed  $J_1$  and  $H$ . For example, the zero percentage figures for  $(\alpha/\beta) = 0$  mean that Hamiltonian (III-1) for this ratio is no more stochastic than an  $N = 3$  harmonic system. The bottom row in Table 1 lists the average stochasticity of Hamiltonian (III-6) as a function of  $(\alpha/\beta)$ , where each average is over the sampling of  $J_1$  values at the given  $(\alpha/\beta)$  ratio. Hence, the last row of Table 1 provides a rough estimate of stochasticity for Hamiltonian (III-1) which is approximately independent of the values of  $H$ ,  $\gamma$ , and  $J_1$ . Finally, in Table 1 we have considered only positive  $(\alpha/\beta)$  ratios and have sampled only those  $J_1$  values for which  $J_1 \leq H$ . Each column in Table 1 may be shown to be invariant to a sign change on the  $(\alpha/\beta)$  ratio. The allowed values of  $J_1$  are almost symmetric about  $J_1 = H$ , which means that the bottom row of Table 1 would be essentially unchanged if we included a sampling of  $J_1 \geq H$  values. In addition, this last row is essentially unchanged if one uses ten representative  $J_1$  values rather than five.

The data for Table 1 were not collected from detailed level curve plots, since such a procedure would be prohibitively time consuming and expensive even on a very high speed computer. Instead we utilized the fact that the distance in phase space between two trajectories, initially started very close to each other, grows more or less linearly in time if the pair of trajectories is started in a smooth level curve region; the distance growth with time is of exponential order or greater for a pair not started in a level curve region. This exponential separation of orbits in phase space appears to be a fundamental property of all highly stochastic or ergodic systems.<sup>7,18,23,24</sup>

Consequently, we integrate a representative sampling of orbit-pairs for each  $(K, J_1)$  level curve plane and take the fractional number of exponentially separating pairs to be the percentage of stochastic orbits in the plane. In addition, if the four-dimensional Hamiltonian (III-6) yields exponentially separating orbit-pairs, then the six-dimensional Hamiltonian (III-3) will also. Thus, the data in Table 1 also represent the fractional number of pair-orbits for Hamiltonian (III-3) with fixed  $H$  and  $J_1$  exhibiting exponential separation in the full six-dimensional phase space.

The distinction between linear separation and exponential divergence for orbit-pairs is clearly seen in Figures 14 and 15. In Figure 14 we plot separation distance versus time for four distinct pair-orbits lying in a smooth level curve region. Here we notice a general linear growth of separation distance with time. In Figure 15 we plot  $\log_{10}$  of the separation distance versus time for four distinct pair-orbits. The two generally lower lying curves are for pair-orbits started in a smooth level curve region and their negative curvature indicates the linear growth of separation distance with time. The generally upper lying curves are for two orbit-pairs started in a stochastic region of the level curve plane, which display the rapid, exponentiating growth of separation distance with time. Thus, we see that integrating pair-orbits for a relatively short period of time will indicate whether they lie in a stochastic or in a stable region of phase space.

Following Equation (II-6) we in effect suggested that including the nonresonant  $V_3$  terms or the higher order terms in Hamiltonian (III-1)

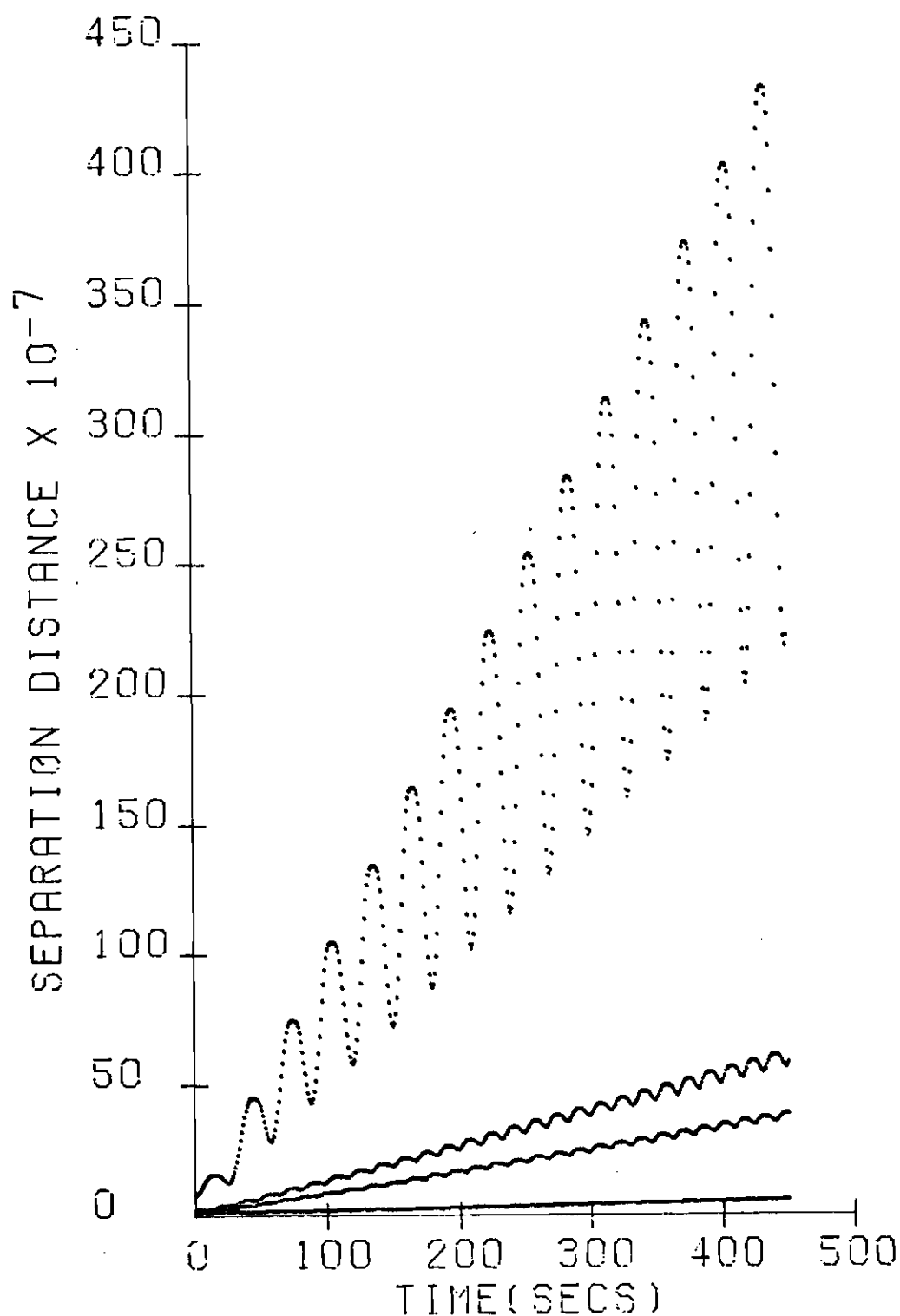


Figure 14. A Plot of Phase Space Separation Distance Between Two Initially Close Trajectories Started in a Stable Region. (Separation distance versus time is plotted for four, distinct orbit-pairs, each orbit-pair starting in a smooth level curve region. Linear growth with time is apparent.)

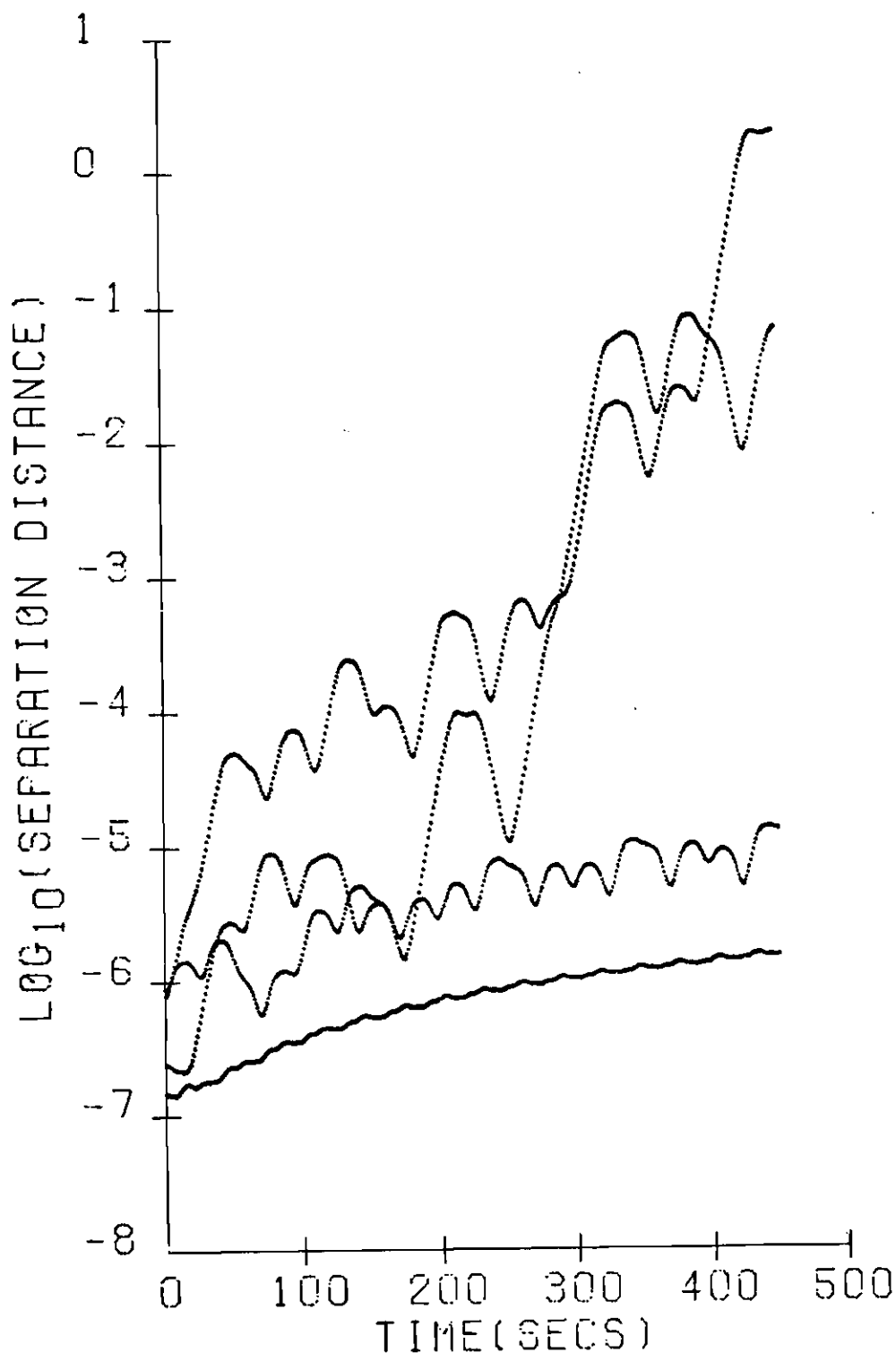


Figure 15. A Plot of  $\log_{10}$  of the Separation Distance Versus Time for Four Distinct Orbit-Pairs. (The generally lower lying curves are for orbit-pairs started in a smooth level curve region, and their generally negative curvature indicates the linear growth of separation distance with time. The generally upper lying curves are for orbit-pairs started in a stochastic region of the level curve plane, and the rapid exponential-order growth of separation distance with time is clear.)



would not radically alter the data of Table 1. In order to partially check this conjecture, we calculated the fractional number of orbit-pairs exhibiting exponential separation after adding numerous non-resonant  $V_3$  terms to Hamiltonian (III-3) but using the same set of initial conditions as for the pure resonant case. In the cases checked, the numbers in Table 1 were changed at most by a few percent. This calculation provides additional evidence that it is the resonant terms themselves in Hamiltonian (II-1) which generate stochastic behavior as predicted by their violation of Arnold's Condition (b).

CHAPTER IV

STOCHASTICITY IN THE LIMIT AS

$\gamma$  TENDS TO ZERO FOR  $N = 3$

In this chapter we investigate stochasticity for the nearly-linear, three-oscillator Hamiltonian (III-1) in the limit as  $\gamma$  tends to zero. As before, the results are summarized in a table analogous to Table 1 of Chapter III. In constructing this table, we follow the same procedure we employed previously. In particular, we estimate the stochasticity for fixed  $H$  in Hamiltonian (III-1) by determining the percentage of trajectories for Hamiltonian (III-6a) that do not yield smooth level curves in each of a representative sampling of  $(q_3, p_3)$  planes. As we mentioned earlier, the motion generated by Hamiltonian (III-6a) for given values of  $K$  and  $J_1$  is invariant as  $\gamma$  tends to zero, except for a change in the time scale. The factor  $\gamma$  enters the calculations only through Equation (III-6c) which relates  $H$  to  $K$  and  $J_1$ . In particular, the range of allowed  $K$  and  $J_1$  values for given  $H$  and  $\gamma$  is determined by Equations (III-6).

In order to clarify this point, we rewrite Equations (III-6) for  $q_2 = 0$  in the form

$$K = (\beta/2)p_2 p_3 A^{\frac{1}{2}}, \quad (\text{IV-1a})$$

$$A + p_2^2 = J_1 - (3/2)(q_3^2 + p_3^2). \quad (\text{IV-1b})$$

Defining  $Y \equiv A^{\frac{1}{2}}$ , we may write Equations (IV-1) as

$$Y^2 + p_2^2 = J_1 - (3/2)(q_3^2 + p_3^2), \quad (\text{IV-2a})$$

$$2Yp_2 = (4K/\beta p_3). \quad (\text{IV-2b})$$

Using the technique of adding and subtracting to complete the squares on the left hand sides, we find

$$p_2 = (1/2)\{\pm[J_1 - (3/2)(q_3^2 + p_3^2) + (4K/\beta p_3)]^{\frac{1}{2}} - (\pm)[J_1 - (3/2)(q_3^2 + p_3^2) - (4K/\beta p_3)]^{\frac{1}{2}}\}. \quad (\text{IV-3})$$

In Equation (IV-1a) we now observe that the product  $(p_2 p_3)$  must have the same sign as  $K$ . Since we shall consider only the case  $K \geq 0$ , we choose to take both  $p_2$  and  $p_3$  positive. Using the relationship  $J_1 = H - \gamma K$  from Equation (III-6c), we may rewrite Equation (IV-3) as

$$p_2 = (1/2)\{[(H - \gamma K) - (3/2)(q_3^2 + p_3^2) + (4K/\beta p_3)]^{\frac{1}{2}} \pm [(H - \gamma K) - (3/2)(q_3^2 + p_3^2) - (4K/\beta p_3)]^{\frac{1}{2}}\}. \quad (\text{IV-4})$$

Now Equation (IV-4) yields real roots for  $p_2$  only if

$$[(H - \gamma K) - (3/2)(q_3^2 + p_3^2) - (4K/\beta p_3)] \geq 0. \quad (\text{IV-5})$$

Finally then Equation (IV-5) determines the allowed range of  $K$ ,  $J_1 = H - \gamma K$ ,  $q_3$ , and  $p_3$  when  $H$  and  $\gamma$  are specified. In the limit as  $\gamma$  tends to zero, Equation (IV-5) becomes

$$[H - (3/2)(q_3^2 + p_3^2) - (4K/\beta p_3)] \geq 0, \quad (\text{IV-6})$$

while Equation (III-6c) becomes

$$H = J_1. \quad (\text{IV-7})$$

Thus as  $\gamma \rightarrow 0$ ,  $J_1$  always equals the given value of  $H$  and the range on  $K$  is determined by Equation (IV-6). We note in passing that Equation (IV-6) can be used to determine bounding curves in the  $q_3 p_3$  plane for the case  $\gamma \rightarrow 0$  in the same way that Equation (III-10) was used for  $\gamma = 1$ .

In Table 2 we list the percentage of stochastic trajectories for Hamiltonian (III-6) in the limit as  $\gamma \rightarrow 0$  for a representative sampling of  $K$  and  $(\alpha/\beta)$  values. As in Table 1 each number in the bottom row is an arithmetic average of the percentages in the column above it. For comparison with Table 1, we again used  $H = 3.00$  in all computer calculations, although the numbers in Table 2 may be shown to be invariant to changes in the value of  $H$ . Each number in Table 2 gives the fractional area of the specified level curve plane containing exponentially separating orbit-pairs. In addition, each number is an approximate estimate of the area more or less uniformly covered by each stochastic orbit in the specified plane.

We have demonstrated in Chapters III and IV that resonant,

Table 2. Percentage of Stochastic Trajectories for Hamiltonian (III-1) in the Limit as  $\gamma \rightarrow 0$ . (The trajectories lie on the four-dimensional space allowed by fixed H and K as a function of K and  $(\alpha/\beta)$ . Percentages are rounded to the nearest whole number. K increases reading down while  $(\alpha/\beta)$  increases reading across.)

K	$\alpha/\beta$																
	0	1/8	2/8	3/8	4/8	5/8	6/8	7/8	8/8	7/8	6/8	5/8	4/8	3/8	2/8	1/8	0
0.0010	0	28	26	19	17	17	12	12	5	3	4	8	6	8	11	20	0
0.0170	0	49	61	64	55	42	31	15	8	8	9	9	5	14	0	0	0
0.0355	0	52	61	70	77	69	48	11	5	8	3	0	0	0	0	0	0
0.0582	0	47	71	72	80	72	15	0	0	0	0	0	0	0	0	0	0
0.0882	0	56	85	76	37	11	0	0	0	0	0	0	0	0	0	0	0
Average over K	0	46	61	60	53	42	21	8	3	4	3	3	2	5	2	4	0

nearly-linear, three-oscillator systems do indeed exhibit stochastic behavior for arbitrarily small nonlinear coupling. In particular, Tables 1 and 2 clearly indicate that stochasticity for Hamiltonian (III-1) is considerably more widespread than for an  $N = 3$  harmonic system, though the percentage of stochasticity decreases appreciably on either side of the ratio  $(\alpha/\beta) \approx (3/8)$ . In addition, as  $N$  increases above three, the percentage of stochasticity for the nearly-linear Hamiltonian (II-7) would be expected to depend less sensitively on the nonlinear parameters because the number of overlapping resonant  $V_3$  terms goes as  $N^2$  and the allowed fraction of the available energy surface increases rapidly with  $N$ . Thus, the widespread stochasticity we have observed for  $N = 3$  probably represents the minimum stochasticity to be generated by the nearly-linear Hamiltonian (II-7) when Arnold's Condition (b) is violated.

## CHAPTER V

## AREA-PRESERVING MAPPINGS

Thus far in our studies of dynamical systems with two and three degrees of freedom, we have made graphical surveys of the complexity of system motion by constructing plots of trajectory intersections with specified planes. Let us now observe that these graphs represent mappings of a plane onto itself which are generated by solving Hamilton's differential equations for the system.<sup>18,19</sup> Indeed, these mappings preserve areas as may be proved<sup>26</sup> using Poincaré's Theorem on integral invariants. As a consequence, there exists an intimate connection between the pathology of trajectories generated by Hamiltonian systems of differential equations and the pathology of area-preserving mappings. Thus, a study of the generic properties of algebraic area-preserving mappings of the form  $x_1 = f(x,y)$ ,  $y_1 = g(x,y)$ , should further illuminate the pathology of the many-body problem. This direct study of algebraic mappings allows us to eliminate the numerical difficulties of solving differential equations and provides us with powerful mapping theorems that are not available for differential equation systems. Without loss of significant generality, we choose to consider only polynomial mappings which are especially convenient for numerical analysis. We shall specify our area-preserving mappings via the relations

$$x_1 = f(x,y), \tag{V-1a}$$

$$y_1 = g(x,y), \quad (V-1b)$$

and denote the mapping by  $(x_1, y_1) = T(x,y)$ .

The simplest case of interest occurs when  $f$  and  $g$  are linear functions of  $x$  and  $y$ .<sup>27</sup> If we assume that the origin is a stable invariant point, this linear mapping can be reduced to a rotation through a constant angle  $\alpha$  about the origin and written in the form<sup>28</sup>

$$x_1 = x \cos \alpha - y \sin \alpha, \quad (V-2a)$$

$$y_1 = x \sin \alpha + y \cos \alpha. \quad (V-2b)$$

The invariant curves for this linear transformation  $T$  are circles, corresponding to the earlier trajectory intersection level curves of the differential equation systems. The operator  $T$  will map each point  $(x,y)$  through the same rotation angle  $\alpha$  on its invariant circle with radius equal to  $(x^2 + y^2)^{\frac{1}{2}}$ . We may rewrite this linear, rotation mapping in the polar coordinate form

$$r_1 = r, \quad (V-3a)$$

$$\theta_1 = \theta + \alpha. \quad (V-3b)$$

If we now let the rotation angle  $\alpha$  become a function of  $r$ , we will introduce a twist into the rotation mapping which is now written

$$r_1 = r, \quad (V-4a)$$



$$\theta_1 = \theta + \alpha(r). \quad (V-4b)$$

Circles are still invariant curves of this twist mapping, but the rotation angle of each circle depends on the radius of that particular circle. We further note that Equations (V-3) and (V-4) both generate mappings corresponding to "integrable" differential equation systems which have smooth trajectory intersection curves everywhere.

We now introduce perturbation terms  $f$  and  $g$  into the twist mappings of Equations (V-4) and ask if the invariant curves persist. The new mapping, denoted by  $T_p$  where  $p$  indicates "perturbation", is given by

$$r_1 = r + f(r, \theta), \quad (V-5a)$$

$$\theta_1 = \theta + \alpha(r) + g(r, \theta), \quad (V-5b)$$

where  $f$  and  $g$  have period  $2\pi$  in  $\theta$ . For this mapping Moser<sup>8</sup> has shown that if  $f$  and  $g$  are sufficiently small, those invariant curves for which the rotation number  $\alpha(r)$  satisfies the inequality  $|\frac{\alpha(r)}{2\pi} - \frac{p}{q}| \geq \frac{\epsilon}{q^{5/2}}$ , where  $p$  and  $q$  are integers, will persist under the perturbations  $f$  and  $g$  and experience only slight distortion. In comparison, the KAM Theorem, as applied to the differential equation systems of Hamiltonian (I-1) for small perturbation  $\gamma V$ , states that most system trajectories continue to lie on smooth, integral surfaces when the frequencies of the motion,  $\Omega_i(J_1, \dots, J_N) \equiv \frac{\partial H_0}{\partial J_i}$ , are incommensurate; i.e., for  $N = 2$  the ratio of the frequencies is an irrational number of the type indicated by the

Moser inequality above.

There is another theorem applicable to the mapping (V-5) which describes additional properties of algebraic systems experiencing small perturbations. This theorem deals with the invariant or fixed points of  $T_p^n$ , by which we mean that the  $n^{\text{th}}$  application of the mapping  $T_p$  will return a given point to its original position. As an illustration of fixed points, let us now consider the unperturbed curves of  $T_p$  bearing rational rotation numbers  $\alpha(r)$  and observe that these curves consist wholly of the invariant points of  $T_p^n$  for  $\alpha(r) = 2\pi\left(\frac{m}{n}\right)$ . When  $f$  and  $g$  are nonzero but small, Birkhoff<sup>29</sup> has shown that the complete curve of fixed points of  $T_p^n$  does not persist; rather, only  $2n$  fixed points remain with  $n$  of these being stable and  $n$  being unstable, where the degree of stability of a given fixed point is manifested by the behavior of nearby points in the plane. The stable fixed points are called elliptic, because, in a small neighborhood of the fixed point, the mapping yields elliptic invariant curves surrounding the fixed point. The unstable fixed points are called hyperbolic, because again nearby invariant curves exist in the form of hyperbolas. The two separate fixed-point families of  $n$  members each are generally interleaved in position around the locus of the former unperturbed invariant curve so that one sees alternating elliptic and hyperbolic points.

Figure 16 from the paper by Arnold<sup>23</sup> illustrates a typical mapping generated by Equations (V-5). Here we see the almost circular invariant curves with irrational rotation numbers that are only slightly distorted by the perturbation as predicted by the Moser Theorem. The alternating elliptic-hyperbolic fixed points predicted by the Birkhoff

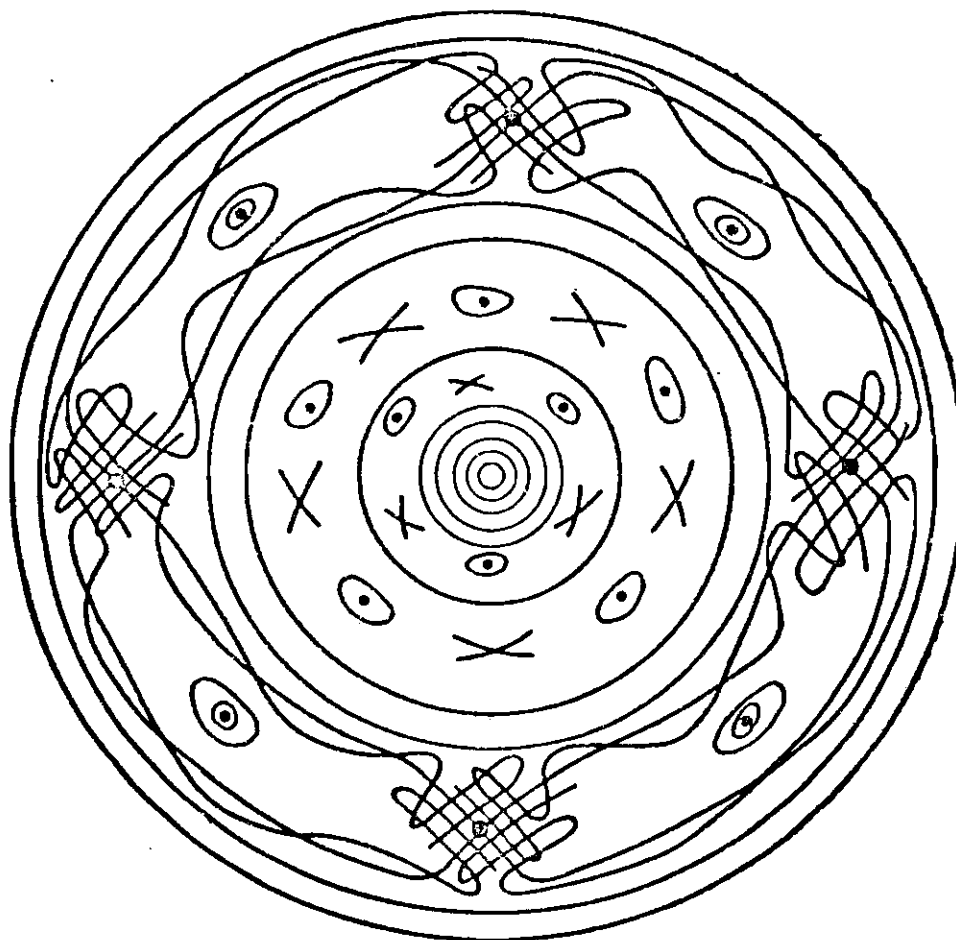


Figure 16. Typical Graph of the Mapping Generated by Equations (V-5), Showing Only the Grossest Features.

Theorem are seen near the origin. The waving, self-intersecting curves emanating from hyperbolic fixed points located near the periphery will be discussed in the next chapter. We should also note that both the Moser and Birkhoff theorems are valid in a neighborhood of each elliptic fixed point of Figure 16. Therefore, the macroscopic picture repeats itself on successive microscopic levels, and we have "boxes within boxes" ad infinitum!

We now have the striking result that even simple algebraic mappings such as Equations (V-5) or the level curve mappings generated by two-oscillator systems such as Hamiltonian (I-2) can yield the incredible intricacies seen in Figure 16. Using the greatest possible computer accuracy, one can see the beginning levels of this complexity in the Henon and Heiles system illustrated in Figure 1. In lieu of attempting to improve the resolution of Figure 1, let us consider the mapping  $T_H$  given by

$$x_1 = x \cos \alpha - (y - x^2) \sin \alpha, \quad (V-6a)$$

$$y_1 = x \sin \alpha + (y - x^2) \cos \alpha, \quad (V-6b)$$

which represents the product of a shear and a rotation as formulated by Henon.<sup>27</sup> It is shown by Henon that any general second-degree polynomials for  $f$  and  $g$  in Equations (V-1) can be reduced to the mapping form of Equations (V-6). In Figure 17 we graph the mapping  $T_H$  of Equations (V-6) for  $\cos \alpha = 0.24$  and notice that at this level of computer accuracy the curves around the elliptic points appear smooth. However, in Figure 18 we magnify a small region near the rightmost hyperbolic

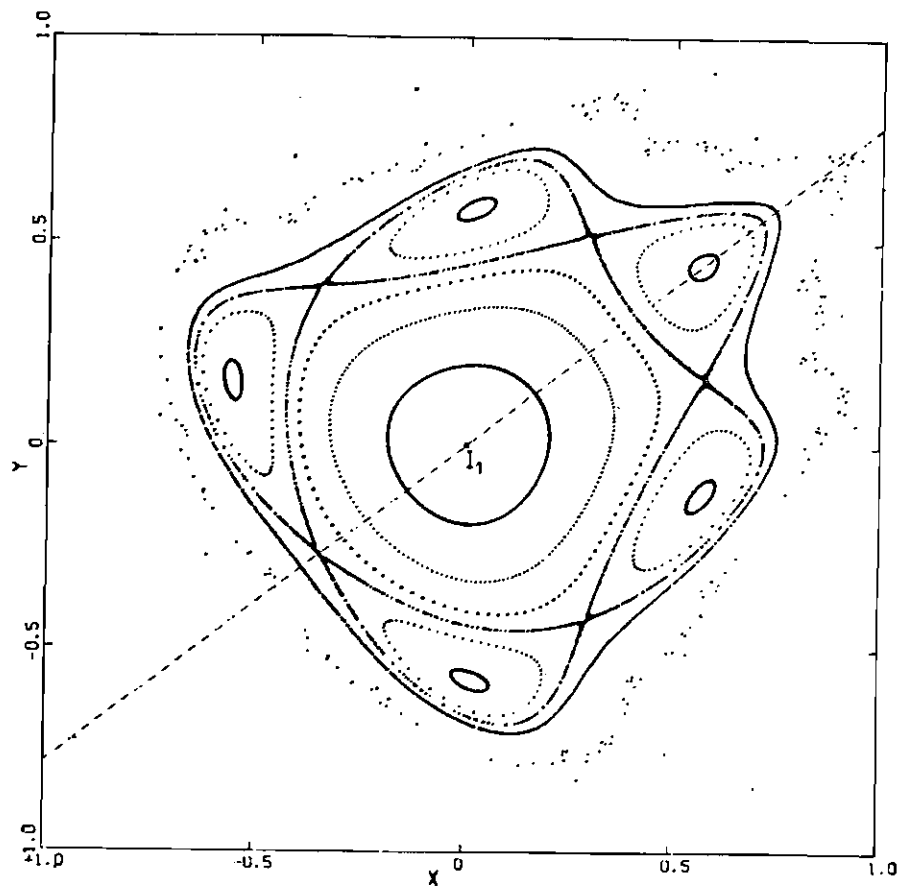


Figure 17. The Henon Algebraic Mapping of Equations (V-6) for  $\cos \alpha = 0.24$ . (Here the invariant curves appear to be smooth.)

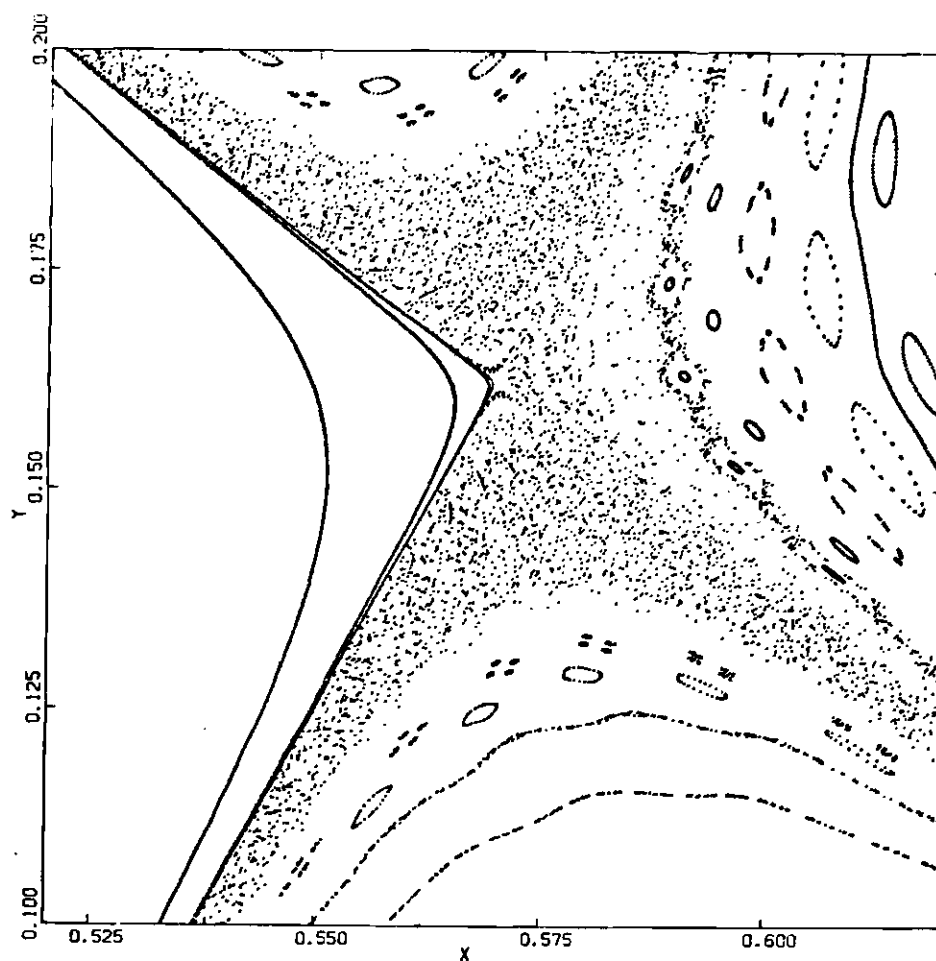


Figure 18. A Magnified Region Around the Rightmost Hyperbolic Fixed Point of the Henon Mapping for  $\cos \alpha = 0.24$ . (This figure shows the very complex structure that exists on a microscopic scale.)

fixed point of Figure 17 and observe some of the incredible complexity of these simple systems.

We have shown in this chapter that simple algebraic mappings can produce the same type of pathology that is generated in level curve planes by the differential equation systems. In particular, we observed that algebraic systems can be constructed which replicate the smooth behavior of integrable Hamiltonians and that the introduction of small perturbation terms into linear algebraic mappings produces diagrams very similar to surface of section plots for Hamiltonian (I-1) with small perturbation  $\gamma V$ . We then discussed the fixed points of a mapping, which are the counterparts of periodic orbits in Hamiltonian systems. The following two chapters develop this close connection between fixed points and periodic orbits in such a way that we will gain new insights into the nature of stochastic behavior.

## CHAPTER VI

## PATHOLOGY OF AREA-PRESERVING MAPPINGS

One of the techniques employed in studying the pathology of area-preserving mappings is to linearize the mapping about an unstable fixed point and then to study the behavior of the extended eigenvectors or separatrices of the resulting linearized transformation matrix. In this chapter we develop this linearization technique for algebraic systems and then use it to illustrate several new properties of stochastic behavior. In Chapter VII we adapt the linearization procedure to differential equation systems and investigate these same stochastic properties for the Henon and Heiles system discussed previously. We now establish the linearization formalism for our mapping analysis; we then proceed to use this analysis in illuminating the nature of stochasticity.

We consider the algebraic mappings to have the general form<sup>19</sup>

$$x_1 = f(x_0, y_0), \quad (\text{VI-1a})$$

$$y_1 = g(x_0, y_0), \quad (\text{VI-1b})$$

which may be written more compactly as

$$(x_1, y_1) = T(x_0, y_0). \quad (\text{VI-2})$$



The functions  $f$  and  $g$  satisfy the area-preserving condition

$$\det (J) = 1, \quad (\text{VI-3})$$

where  $J$  is the Jacobian matrix of the partial derivatives,

$$J(x,y) = \begin{bmatrix} f_x & f_y \\ g_x & g_y \end{bmatrix}, \quad (\text{VI-4})$$

in which we denote the partial derivatives as  $f_x \equiv \frac{\partial f}{\partial x}$ , etc. The  $n^{\text{th}}$  iteration of the mapping can be written as

$$(x_n, y_n) = T^n(x_0, y_0). \quad (\text{VI-5})$$

We linearize the mapping around a given initial point  $(x_0, y_0)$  by forming the first-order differentials of Equations (VI-1),

$$\Delta x_1 = \left( \frac{\partial f}{\partial x} \right)_0 \Delta x_0 + \left( \frac{\partial f}{\partial y} \right)_0 \Delta y_0, \quad (\text{VI-6a})$$

$$\Delta y_1 = \left( \frac{\partial g}{\partial x} \right)_0 \Delta x_0 + \left( \frac{\partial g}{\partial y} \right)_0 \Delta y_0, \quad (\text{VI-6b})$$

which may be expressed in the matrix form

$$\begin{bmatrix} \Delta x_1 \\ \Delta y_1 \end{bmatrix} = \begin{bmatrix} f_x & f_y \\ g_x & g_y \end{bmatrix}_{x_0, y_0} \begin{bmatrix} \Delta x_0 \\ \Delta y_0 \end{bmatrix} = J(x_0, y_0) \begin{bmatrix} \Delta x_0 \\ \Delta y_0 \end{bmatrix}. \quad (\text{VI-7})$$

The matrix representing the linearized mapping in the vicinity of a fixed point of  $T^n$  is denoted by  $M$  and is defined by the relationship

$$M \equiv J(x_{n-1}, y_{n-1}) \cdot J(x_{n-2}, y_{n-2}) \cdot \dots \cdot J(x_0, y_0), \quad (\text{VI-8})$$

where  $(x_0, y_0)$  is a fixed point of  $T^n$  that satisfies the equation

$$(x_0, y_0) = T^n(x_0, y_0). \quad (\text{VI-9})$$

The linearized mapping about  $(x_0, y_0)$  for  $T^n$  is then given by

$$\begin{bmatrix} \Delta x_n \\ \Delta y_n \end{bmatrix} = M \cdot \begin{bmatrix} \Delta x_0 \\ \Delta y_0 \end{bmatrix}. \quad (\text{VI-10})$$

With this linearization formalism in mind, we now turn our attention to the eigenvalues and eigenvectors of the matrix  $M$  in Equation (VI-8) in order to see what stochastic properties they reveal in a mapping.

### Analysis of Separatrix Behavior

In the discussion of Figure 16 it was pointed out that Birkhoff's Theorem predicts that perturbations will break down certain invariant mapping curves into families of elliptic (stable) and hyperbolic (unstable) fixed points. Let us focus our attention on the hyperbolic members of such families. One may linearize the mapping about these hyperbolic fixed points and plot the associated, extended eigenvectors of the matrix  $M$ , thereby gaining insight into the basic structural organization of the plane. We shall first consider the "integrable"

area-preserving mapping, defined as one that yields exact, invariant curves everywhere, which is shown in Figure 19, but which is not explicitly written out here. This figure shows an elliptic point at the origin, which we shall ignore, and an ordinary hyperbolic point along the  $45^\circ$  line in the first quadrant, which we shall consider in detail. This hyperbolic fixed point has the incoming separatrix, labeled 1-1', which consists of two branches or segments as shown in the figure; successive iterates of a point started on either of the two branches will asymptotically approach the fixed point while remaining on the same branch. In addition, successive iterates recede from the fixed point along the double-branched, outgoing separatrix, labeled 2-2', where the iterates continue along the same branch as before. We may generate separatrix branches 1 and 1' by inverse-mapping a point along each incoming branch, while separatrix branches 2 and 2' are evolved by forward-mapping a point on each outgoing branch. Moreover, we observe for the "integrable" mapping of Figure 19 that the forward segment 2 and the inverse segment 1 join smoothly into a single curve. Here a single, smooth curve must result since an "integrable" mapping has smooth curves everywhere.

If on the other hand, one now includes the general perturbation terms  $f$  and  $g$  of Equations (V-5), one finds that there are no longer smooth invariant curves everywhere and, in particular, that the separatrices intersect each other. Figure 20 shows the criss-crossing of the forward-mapped outgoing separatrix  $FJLQARQ'A'R'Q''A''R''$  and the inverse-mapped incoming separatrix  $JKLQBRsQ'R'Q''B''R''$  for a typical non-integrable mapping.<sup>30</sup> The line segment QAR evolves after three

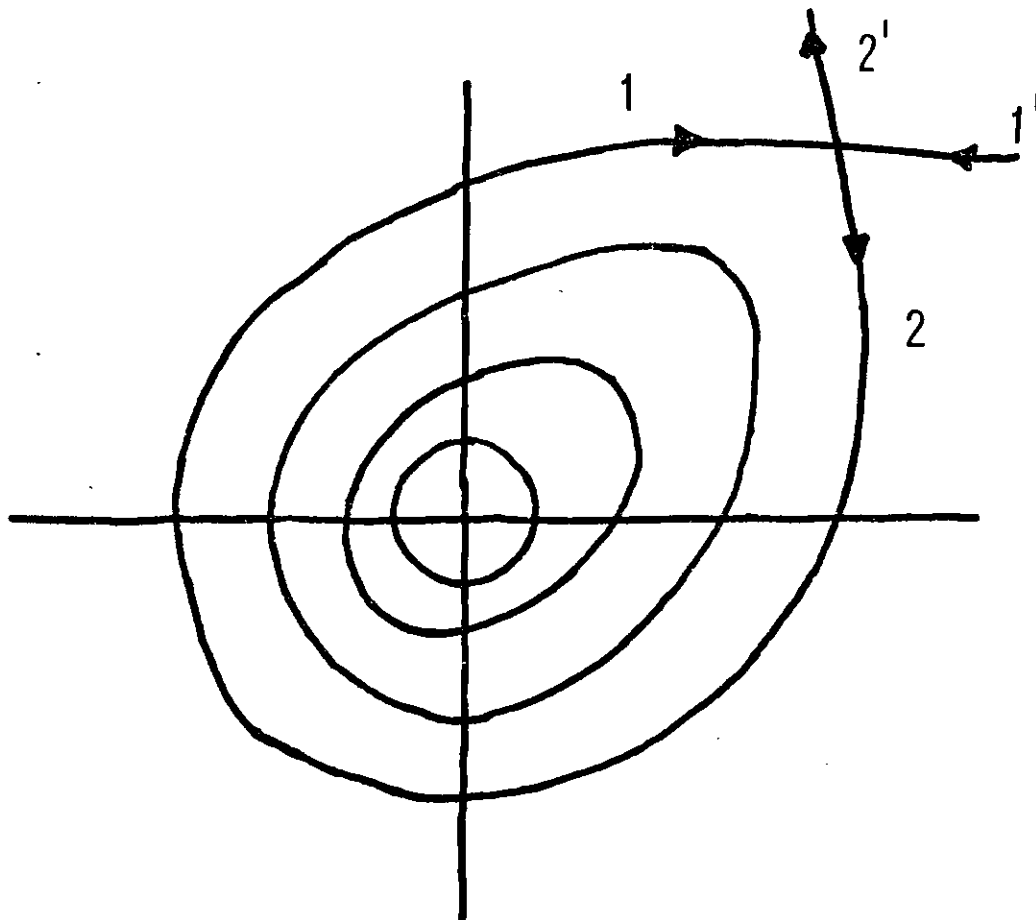


Figure 19. Invariant Curves for an Integrable Mapping. (The self-intersection point is an ordinary hyperbolic fixed point.)

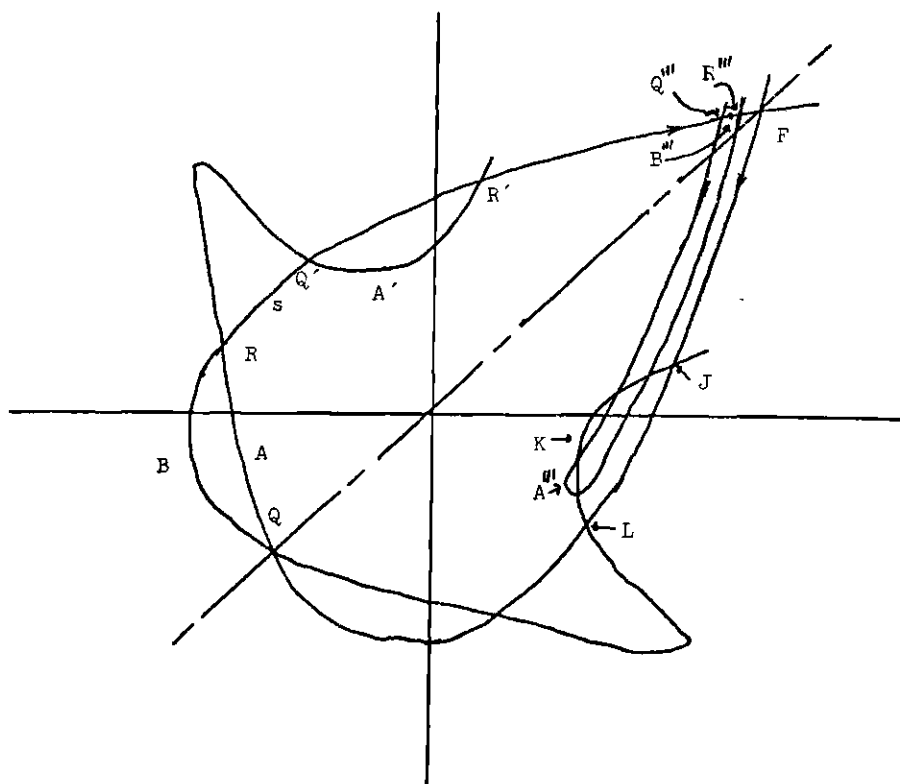


Figure 20. Invariant Curves for a Small Non-integrable Perturbation.  
 (The separatrices are no longer firm but intersect in wild oscillations.)

iterations of the mapping into the segment  $Q''A''R''$ , while the segment  $QBR$  transforms after three forward iterations into the segment  $Q''B''R''$ . Thus, the area  $QARBQ$  transforms into the thin filament  $Q''A''R''B''Q''$  having equal area. Succeeding iterations will transform this particular area into narrower and more elongated filaments as the section along the incoming separatrix asymptotically approaches the fixed point. These elongating area-filaments provide the mechanism by which points initially close together can map very quickly apart in an exponential fashion. As the strengths of the perturbations  $f$  and  $g$  in Equations (V-5) are increased, the forward and backward separatrices intersect at ever increasing angles, thus eroding more and more of the stable region surrounding the elliptic fixed point.

This phenomenon of intersecting separatrices also occurs when the inverse-mapped incoming separatrix from one hyperbolic fixed point crosses the forward-mapped outgoing separatrix from an adjacent hyperbolic point of the same family, as is illustrated in Figure 16. In this particular figure we note that the relative size of the elliptic fixed-point family in a given annulus diminishes as the distance from the origin increases, which is a direct result of the increasing erosion of the stable areas by the intersecting separatrices. Finally, at sufficient distances from the origin there will be an intertwining of separatrices from different fixed-point families in addition to the intersecting separatrices from adjacent hyperbolic points of the same family, thus giving a random appearance to successive iterates from a given point. When the complexity reaches this last state, it is

almost impossible to predict the location of successive iterates of a point by topological considerations of the type discussed in connection with Figure 20; this phenomenological behavior is characteristic of stochastic regions.

Even the elliptic fixed points can change character and become hyperbolic (unstable) when the general perturbation terms  $f$  and  $g$  in Equations (V-5) become sufficiently large. Moreover when  $f$  and  $g$  are large, most of the invariant curves, predicted by the Moser Theorem for small  $f$  and  $g$ , will decompose into sequences of erratic points. Those hyperbolic fixed points arising from converted elliptic fixed points are called hyperbolic with reflection or hyperbolic II in order to distinguish them from the ordinary hyperbolic I fixed points which interleave between elliptic fixed points as shown in Figure 16. As we shall illustrate, the hyperbolic fixed point with reflection is much more pathological than the ordinary hyperbolic I fixed point. Both of these unstable fixed points have one approaching and one receding separatrix. As we discussed earlier, iterates of points started on a given separatrix branch continue to lie on the same branch for the hyperbolic I fixed point; however, successive iterates for the hyperbolic II fixed point alternately jump from one separatrix branch to the other, hence the phrase "with reflection".

Figure 21 illustrates this behavior by depicting the separatrices of two adjacent hyperbolic II fixed points for a mapping studied by Laslett<sup>31</sup> having the form

$$x_1 = y + c_1 x + c_2 x^2, \quad (\text{VI-11a})$$

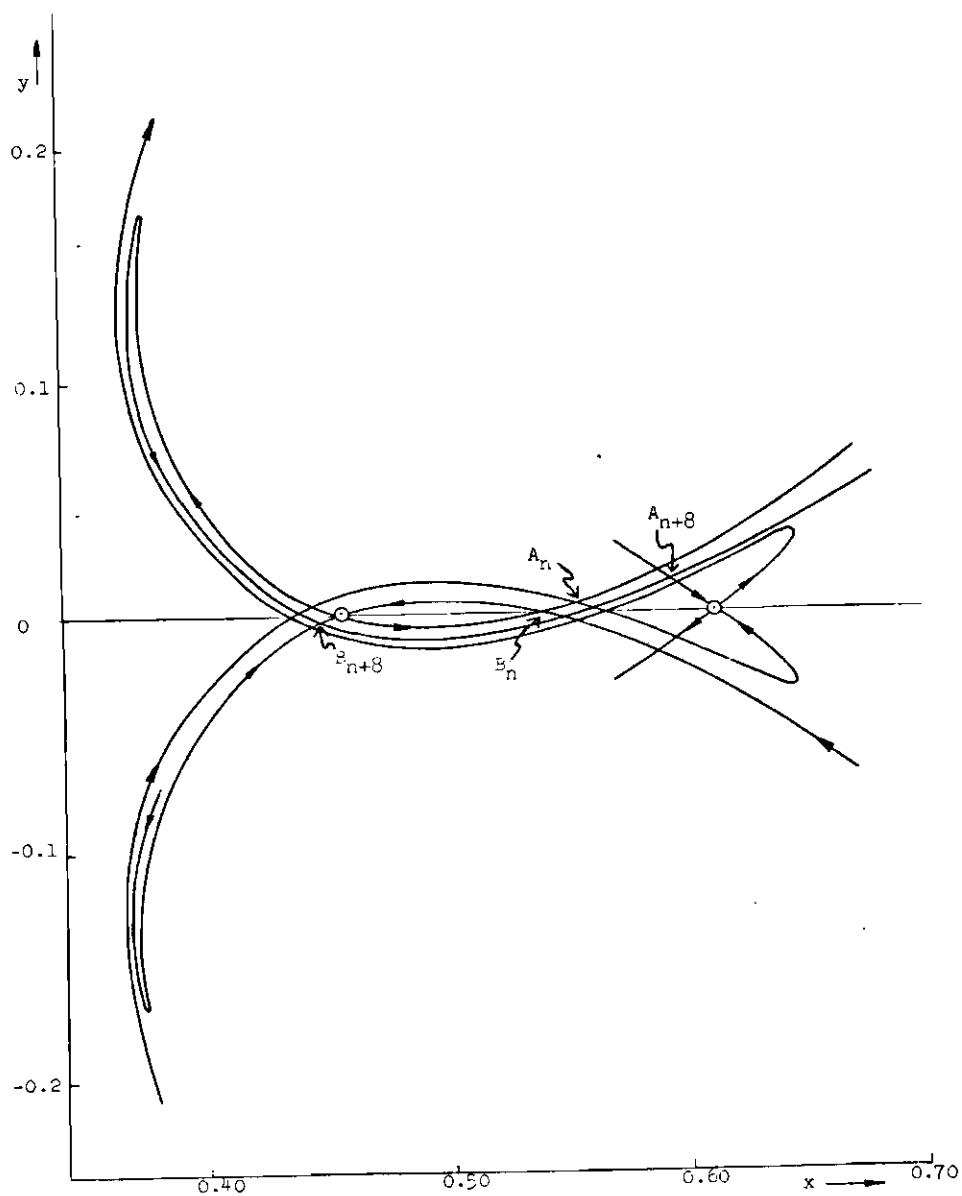


Figure 21. An Adjacent Pair of Hyperbolic II Fixed Points for the Laslett Mapping of Equations (VI-11).



$$y_1 = -x + c_1 x_1 + c_2 x_1^2; \quad (\text{VI-11b})$$

where

$$c_1 = -(1/8), \quad (\text{VI-11c})$$

$$c_2 = 1 - c_1. \quad (\text{VI-11d})$$

Here we choose to consider the two members of a family of eight hyperbolic II fixed points which are located at the  $\odot$ -symbols in Figure 21. Consider the point  $A_n$  that lies on the incoming separatrix approaching the right fixed point and that also lies on the outgoing separatrix directed away from the left fixed point. After eight applications of the mapping (VI-11), the point  $A_n$  becomes  $A_{n+8}$  and has moved so as to lie closer to the right fixed point (but on the other incoming branch) and to lie more remotely from the left fixed point (but on the other outgoing branch). Alternatively, for the point  $B_n$  which lies on the intersection of the outwardly and inwardly directed separatrices from the same left-most hyperbolic II fixed point, we observe that  $B_{n+8}$  lies closer in on the incoming separatrix and more remote on the outgoing separatrix. Moreover,  $B_{n+8}$  is on the opposite branch of each separatrix. Thus we see that the behavior of points near hyperbolic II fixed points is much wilder than that near ordinary hyperbolic I points.

This pair of hyperbolic fixed points with reflection, which occurs for large perturbations, that we have been discussing in Figure 21 is part of a family of eight fixed points which is interleaved between an

associated family of eight ordinary hyperbolic I fixed points. Thus, the elliptic-hyperbolic I alternation that is seen in Figure 16 for weaker perturbations  $f$  and  $g$  quite generally becomes the hyperbolic I - hyperbolic II pattern for the large perturbations of the Laslett mapping in Equations (VI-11). We note in passing that the general perturbation terms  $f$  and  $g$  in Equations (V-5) are simply nonlinear, algebraic terms that become larger as the distance from the origin increases, which means that there are alternating hyperbolic I - hyperbolic II pairs of fixed points present at large distances from the origin beyond the periphery shown in Figure 16. This configuration of alternating unstable points allows the interesting possibility that in the highly nonlinear, stochastic regions of a mapping all (or almost all) fixed points are hyperbolic. In such a region containing principally a large number of unstable fixed points, the iterates of almost every point would be expected to appear randomly, and two points started close together might be expected to diverge apart at an exponential rate. Thus, the exponentiating orbits associated with stochasticity appear to occur when the preponderance of fixed points are hyperbolic and when the measure of the stable regions influenced by elliptic fixed points is very small.

In developing a theory of stochastic systems, Arnold and other investigators<sup>18</sup> use this fundamental property of exponentiation as the defining condition for "C-systems" which may be shown to be both ergodic and mixing. Here ergodic means that each trajectory uniformly covers a specified region of phase space, while mixing is associated with a uniform diffusing of a cluster of initially close orbits throughout the

specified region of phase space. As a simple example, we consider Arnold's area-preserving mapping of the unit square onto itself given by

$$x_1 = x + y, \quad (\text{VI-12a})$$

$$y_1 = x + 2y, \quad (\text{VI-12b})$$

where  $(x_1, y_1)$  is reduced modulo 1. The eigenvalues of the already linearized transformation matrix for this mapping are  $\exp(\pm \theta)$ , where  $\cosh \theta = 3/2$ . We now note that a series of transformations can bring the general mapping of Equations (VI-1) into the form<sup>28</sup>

$$x_1 = \lambda x, \quad (\text{VI-13a})$$

$$y_1 = (1/\lambda)y, \quad (\text{VI-13b})$$

where  $\lambda$  and  $(1/\lambda)$  are the real eigenvalues of the linearized transformation matrix. Thus, since the real eigenvalues are  $\exp(\pm \theta)$  for the specific mapping of Equations (VI-12), we anticipate that small area elements will change their shape exponentially for the Arnold transformation by successively diverging in one direction and shrinking in the other direction. The trend toward ergodicity and mixing after only two iterations of the Arnold mapping (VI-12) is indicated in Figure 22, which reveals a crazy, mixed-up cat!

In agreement with the earlier suggestion that such stochastic

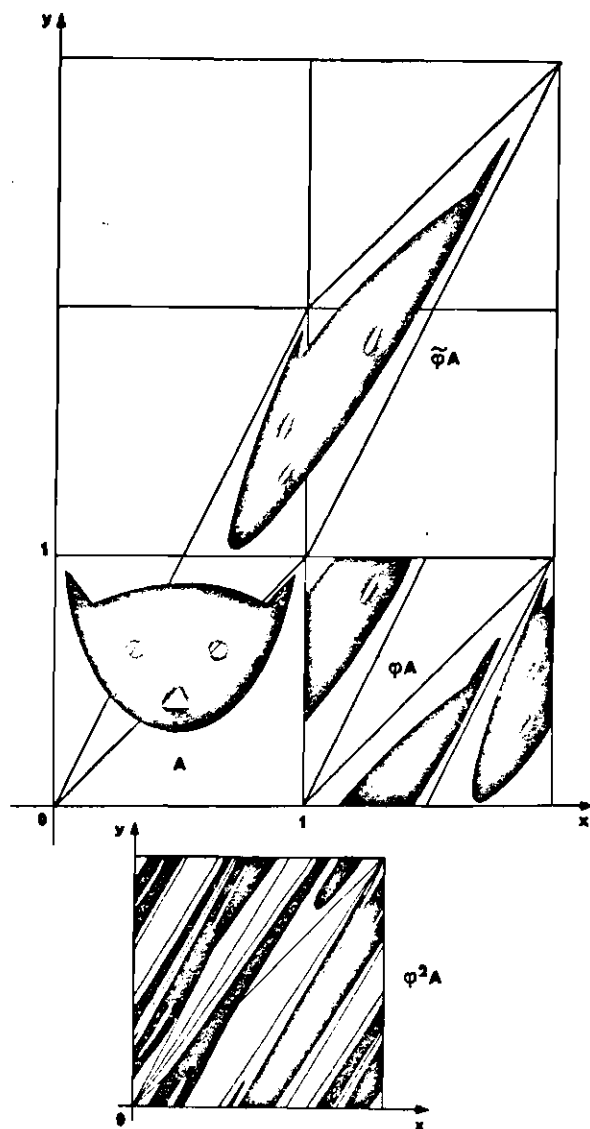


Figure 22. An Example of the Arnold Mapping of Equations (VI-12) Which is Ergodic and Mixing. (Note the mixing of the cat after only two iterations of the mapping.)

behavior results from the presence of a host of hyperbolic fixed points, it is interesting to note that the Arnold mapping (VI-12) does have a dense set of hyperbolic fixed points. First, since the eigenvalues of the mapping are real, it is straightforward to show that all fixed points are hyperbolic. The integer coefficients in Equations (VI-12) then insure that each point  $(a,b)$  in the unit square, for which  $a$  and  $b$  are both rational, is a fixed point after  $k$  iterations of the mapping, for some integer  $k$ . As a consequence, each "non-periodic" point of the mapping uniformly covers the unit square, being "scattered" off the dense set of hyperbolic fixed points.

We have seen that the eigenvalues and extended eigenvectors (separatrices) of the linearized transformation matrix about the unstable fixed points can reveal much interesting detail concerning stochastic behavior. We now turn our attention to a technique developed by Greene which quantifies the occurrence of fixed points, indicating that stochastic regions always contain a dense, or nearly dense, set of hyperbolic fixed points.

#### Stability Analysis Technique of Greene

Having described the behavior of the extended eigenvectors of the linearized matrix about the hyperbolic fixed points, we seek to obtain aggregate data about the complete set of fixed points in a mapping in order to determine the locations of stochastic regions of the mapping plane. Moreover, we desire to predict the stability of a macroscopic area when the nature of a relatively small set of fixed points in the region is known so that we can obtain a maximum of information from a minimum of calculation. To these ends, Greene considers the

fixed points of the algebraic area-preserving mapping  $T_G$  given by<sup>19</sup>

$$x_1 = (1/A)(x_0 - By_0 + Cy_0^3), \quad (\text{VI-14a})$$

$$y_1 = Ay_0 + Bx_1 - Cx_1^3, \quad (\text{VI-14b})$$

where

$$A = 1.25, B = 0.10, C = 0.35. \quad (\text{VI-14c})$$

This mapping is symmetric about the line  $y = x$ , and the fixed points of  $T_G$  are a hyperbolic I point at the origin and elliptic points at  $(1,1)$  and  $(-1,-1)$ . We shall refer to these two elliptic points as central fixed points of the mapping. The pattern of the mapping about either elliptic central fixed point looks very much like Figure 16. Here, however, we shall focus our attention only on the fixed points. Figure 23, for example, shows several fixed-point families in the first quadrant lying about the central fixed point at  $(1,1)$  for the mapping (VI-14). The fixed points of  $T_G$  form two families of  $Q$  members each about the central fixed point in which the  $Q$  members of each family have the same stability. In short, the elliptic central fixed point is surrounded by families of interleaving elliptic-hyperbolic I or, further out from the central fixed point, hyperbolic I - hyperbolic II fixed points just as in Figure 16.

It is convenient to further identify these fixed-point families by their rotation number  $\omega \equiv P/Q$ , where  $Q$  is the number of iterations

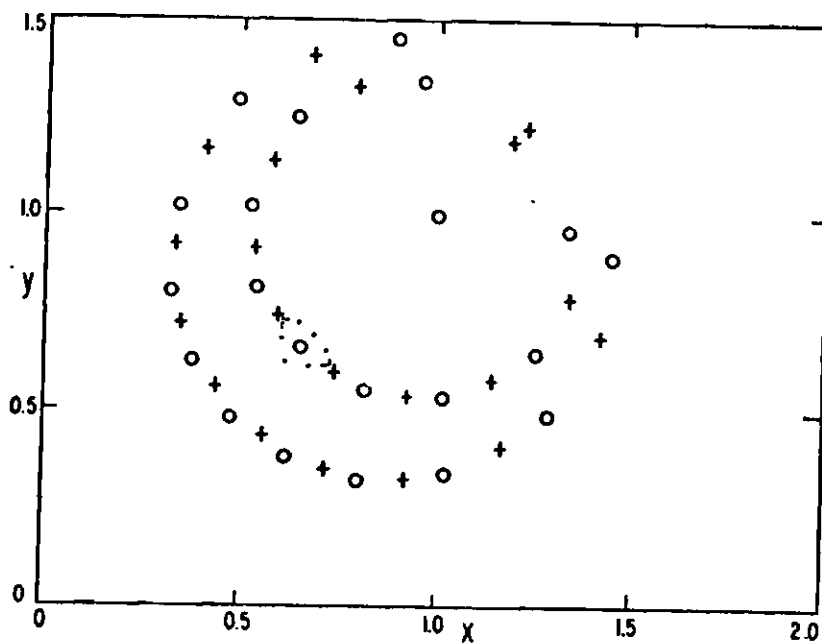


Figure 23. Some Fixed Points of the Greene Algebraic Mapping Given by Equations (VI-14). (The outermost ring consists of fixed points of  $T^{11}$  with alternating hyperbolic I (+) and hyperbolic II (o). The inner ring is composed of fixed points of  $T^9$  with alternating elliptic (o) and hyperbolic I (+). Also shown by (.) are 20 members of a family of  $T^{180}$  associated with the elliptic points of  $T^9$ .)

of the mapping  $T_G$  required to return the fixed point to its initial position, and  $P$  is the number of rotations around the central fixed point when following from a fixed point to its return image through all  $Q$  members of the family. Thus in Figure 23 the rotation numbers of the families of 11 and 9 members are  $1/11$  and  $1/9$  respectively, while the rotation number of the  $T_G^{180}$  family is  $20/180$ . We may also consider the rotation number  $P/Q$  as representing the average fractional part of a complete rotation around the central invariant point that is subtended by a fixed point and its first mapping image at the central fixed point. An additional property of the rotation number is that two fixed-point families lying close to each other should have nearly equal values of  $P/Q$ , which follows from the continuity of the approximate organization of the mapping.

In order to discuss the overall composition of a mapping -- its invariant curves and its stochastic regions -- in terms of its fixed points, one must organize the fixed-point structure recursively in a hierarchy. The zeroth order of the hierarchy consists of the fixed points of  $T_G$ . The first order consists of the invariant curves that enclose the fixed points of  $T_G$  and those fixed points of  $T_G^Q$  for which  $P$  and  $Q$  are relatively prime. The second order of the hierarchy includes this same type structure around the first-order elliptic fixed points in the hierarchy, etc. Thus, there is an infinite number of orders in the hierarchy. It is difficult to expose any meaningful relationships in the mapping unless one first disregards fixed points of higher orders and concentrates primarily on the first order. It perhaps should be pointed out that some fixed-point families cannot be ordered



into the hierarchy, but these appear to be in the minority.

In order to describe the character of the fixed points of a mapping, it is convenient to calculate the trace of the linearized matrix  $M$  of Equation (VI-8) and to define a quantity  $R$  called the residue of the fixed point by the relation

$$R \equiv (1/2) - (1/4) \cdot \text{Trace } (M). \quad (\text{VI-15})$$

For fixed points, Greene establishes the following identification between the various ranges of the residue and the corresponding eigenvalues  $\lambda_i$  of the matrix  $M$ ;

$$R < 0 \rightarrow \lambda_i > 0: \text{ hyperbolic I fixed point,} \quad (\text{VI-16a})$$

$$0 < R < 1 \rightarrow \lambda_i \text{ complex: elliptic fixed point,} \quad (\text{VI-16b})$$

$$R > 1 \rightarrow \lambda_i < 0: \text{ hyperbolic II fixed point.} \quad (\text{VI-16c})$$

In order to calculate the residue of a given fixed-point family (all members may be shown to have the same residue), one first determines the matrix  $M$  in either of two ways. In the first method one explicitly evaluates the Jacobian matrix of the transformation and forms the appropriate matrix product as indicated in Equation (VI-8). The second method due to Henon<sup>32</sup> involves an empirical evaluation of the four elements of the matrix  $M$ . Here one first takes two closely spaced point-pairs, each oriented parallel to a distinct axis of the mapping, and then

one determines the separation between the members of each pair generated by the required number of mapping iterations. Thence one can determine  $M$ . In order to illustrate this method for the case of a fixed point of  $T^Q$  located at  $(x_0, y_0)$ , we follow Greene and specify the matrix elements of  $M$  by the equation

$$M \equiv \begin{bmatrix} (a+d) & (c+b) \\ (c-b) & (a-d) \end{bmatrix}, \quad (\text{VI-17})$$

and then we rewrite Equation (VI-10) in the form

$$\begin{bmatrix} \Delta x_Q \\ \Delta y_Q \end{bmatrix} = M \cdot \begin{bmatrix} \Delta x_0 \\ \Delta y_0 \end{bmatrix} = \begin{bmatrix} (a+d) & (c+b) \\ (c-b) & (a-d) \end{bmatrix} \cdot \begin{bmatrix} \Delta x_0 \\ \Delta y_0 \end{bmatrix}. \quad (\text{VI-18})$$

We now choose a neighboring point of  $(x_0, y_0)$  having coordinates  $(x_0 + \Delta x_0, y_0)$  and iterate  $Q$  times, which carries the original point  $(x_0 + \Delta x_0, y_0)$  to the location  $(x_Q^{(1)}, y_Q^{(1)})$ . Since  $\Delta y_0 = 0$ , we find using Equation (VI-18) that

$$(a+d) = \frac{x_Q^{(1)} - x_0}{\Delta x_0}, \quad (\text{VI-19a})$$

$$(c-b) = \frac{y_Q^{(1)} - y_0}{\Delta x_0}. \quad (\text{VI-19b})$$

We then take another neighboring point of  $(x_0, y_0)$  with coordinates

$(x_0, y_0 + \Delta y_0)$  and again iterate  $Q$  times, obtaining the new point  $(x_Q^{(2)}, y_Q^{(2)})$ . Since  $\Delta x_0 = 0$ , Equation (VI-18) now yields

$$(c+b) = \frac{x_Q^{(2)} - x_0}{\Delta y_0}, \quad (\text{VI-19c})$$

$$(a-d) = \frac{y_Q^{(2)} - y_0}{\Delta y_0}. \quad (\text{VI-19d})$$

Clearly Equations (VI-19) determine the matrix elements of  $M$ , and we shall use these equations to determine  $M$  for the fixed points of the Greene mapping.

Since the mapping (VI-14) is symmetric about the line  $y = x$ , one member of each first-order fixed-point family for odd  $Q$  must lie on this line, while two members of each fixed-point family with even  $Q$  may lie on this line. Thus, we choose to numerically search the line  $y = x$  for fixed points of  $T_G^Q$ , where  $Q$  may be even or odd, and  $Q$  and  $P$  are relatively prime. By varying a trial initial point  $(x_0, y_0 = x_0)$  until the numerically calculated  $Q^{\text{th}}$  iteration returns to within a desired radius of the initial point, we sequentially determine a set of fixed points. The linearized matrix  $M$  is then determined for each fixed-point family using Equations (VI-19) and the residue  $R$  given by Equation (VI-15) is calculated. This numerical search finally then yields a spectrum of residues which demonstrates that most first-order fixed-point families located near the central invariant point at  $(1,1)$  consist of alternating elliptic-hyperbolic I fixed points, while an increasing percentage of alternating hyperbolic I - hyperbolic II fixed-point families are found to occur as the distance from  $(1,1)$  increases. Thus, the residue profile for the Greene mapping has confirmed the same topological progression -- from stable elliptic to unstable hyperbolic II fixed points as the distance from

the central invariant point increases -- that we mentioned earlier in connection with Figure 16.

A further analysis of the residue spectrum using relationships (VI-16) can provide additional insight into the predominant nature of fixed points lying in a stochastic region. In particular, we seek to determine the locations of stochastic regions in the mapping plane by ascertaining the nature of a relatively few selected fixed points of the mapping. In order to establish this insight, we note from previous empirical mapping studies<sup>31</sup> that it is fruitful to generate a residue profile using fixed-point families whose inverse rotation numbers  $\omega^{-1} = Q/P$  lie in selected arithmetic sequences. In particular, we shall follow the procedure used by Greene<sup>19</sup> and consider only the residues of first-order fixed-point families with  $Q/P$  values lying on a sequence of the type  $Q/P = k/\ell \pm 1/n$ , where  $k$  and  $\ell$  are relatively small positive integers and  $n = 1, 2, 3, \dots$ . From this vantage point, it may then be empirically shown that residues can be expressed in terms of a phenomenological function  $f(P/Q)$  defined via

$$R = \alpha [f(P/Q)]^{Q/2}, \quad (\text{VI-20a})$$

or equivalently by

$$f(P/Q) = (R/\alpha)^{2/Q}, \quad (\text{VI-20b})$$

where  $\alpha$  is a constant of proportionality. For the typically large values of  $Q$  we encounter, the factor  $(1/\alpha)^{2/Q}$  is so close to unity that it can

be effectively ignored. We shall use Equations (VI-20) primarily in analyzing the residue spectrum for the selected sequences of first-order fixed-point families indicated above, although in Appendix C we apply these equations to certain second-order families as well. Before presenting the actual fixed-point data obtained by Greene and verified in our own investigation of the  $T_G$  mapping, let us first indicate why the investigative procedure we have described above is efficacious in attempting to locate the stochastic regions in the mapping plane.

In the earlier sections of this chapter, we indicated that widespread stochasticity occurs when there is a predominance of alternating hyperbolic I - hyperbolic II fixed points in a given region of the mapping plane. In view of this result, we desire that the present investigative technique clearly indicate the occurrence and distribution of the unstable hyperbolic I - hyperbolic II fixed-point families in the mapping plane. In this regard, Greene presents arguments indicating that a sequence of fixed points with  $Q/P = k/\ell \pm 1/n$  for  $k$  and  $\ell$  relatively small integers and  $n = 1, 2, 3, \dots$  yields the minimum values of  $f$  that exist in a given  $Q/P$  region where  $f$  is determined from the positive residues via Equation (VI-20b). Moreover, Greene establishes that the hyperbolic I families of the mapping  $T_G^Q$  have residues with magnitudes comparable to their interleaved, associated  $T_G^Q$  elliptic positive-residue families. Thus, we are at liberty to take an absolute value in the relationship  $f = |R/\alpha|^{2/Q}$  and admit the negative-residue hyperbolic I families to the discussion. Since the equation  $f = |R/\alpha|^{2/Q}$  implies that  $f > 1$  occurs when  $|R| > 1$  and since relationships (VI-16) associate values of  $|R| > 1$  with unstable hyperbolic fixed points, we

would anticipate a preponderance of hyperbolic I - hyperbolic II families in those regions of the mapping plane for which the corresponding  $f$ -values exceed unity. Having indicated that the chosen procedure does indeed augur a modest success, let us now consider some actual fixed-point data obtained by Greene using these techniques .

Figure 24 presents a plot of  $f$  versus  $Q/P$  for  $\alpha = 1/4$  which is constructed from the first-order, positive-residue, fixed-point families of  $T_G^Q$  with inverse rotation numbers given by  $Q/P = k/\ell \pm 1/n$  as previously described. The most salient feature of this graph is the general upward trend of the minimum  $f$ -curve, which appears to remain above unity for values of  $Q/P > 9.0$ . Since we shall locate the stochastic regions of the mapping plane by observing which portions of the  $f$ -curve lie above unity, it is important to establish beyond reasonable doubt that Figure 24 does in fact present the minimum  $f$ -curve for the given  $Q/P$  region. In this regard, we located a host of fixed points with rather arbitrary values of  $Q/P$ , all of which yielded  $f$ -values that lay on or above the  $f$ -curve in Figure 24. Therefore, the curve in the figure appears likely, as Greene suggests, to indeed be the minimum  $f$ -curve for the given span of  $Q/P$  values.

In light of Equations (VI-20) and Figure 24, we anticipate that nearly all fixed-point families with  $Q/P > 9.0$  are hyperbolic I or II. We do not say "all" fixed-point families for at least two reasons. The first reason is that a minority of families are irregular in behavior and cannot be ordered into the hierarchial structure, and these anomalous families might have  $f$ -values lying below unity when  $Q/P > 9.0$ . The second reason why all fixed-point families may not be hyperbolic for

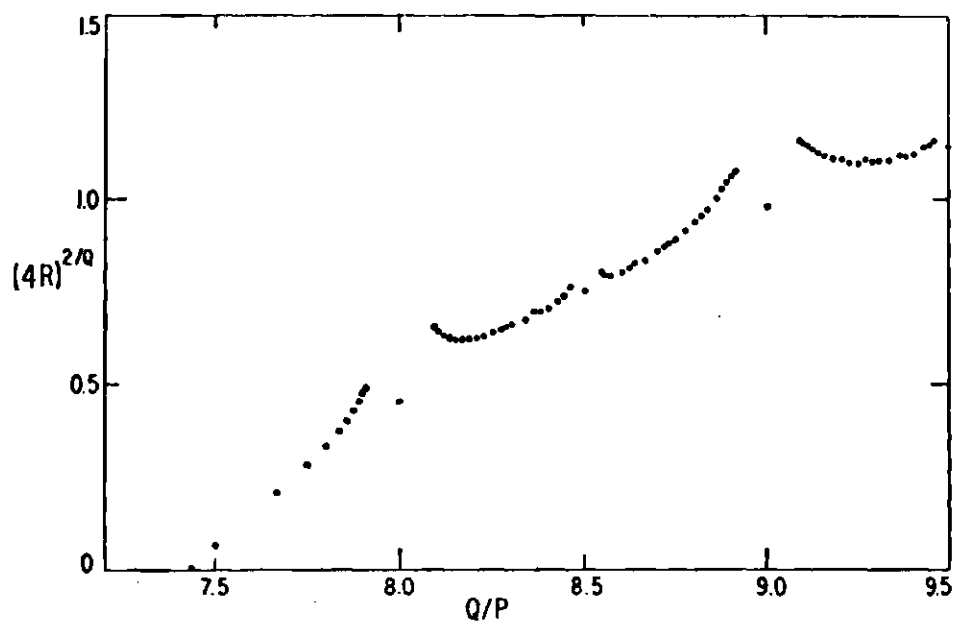


Figure 24. A Plot of  $f = (4R)^{2/Q}$  Versus Inverse Rotation Number for Selected Fixed Points of the Greene Mapping.

$Q/P > 9.0$  is that Figure 24 is an  $f$ -curve plot for only first-order families of the hierarchy. While it is reasonable to assume that the higher-order families associated with each first-order elliptic family become unstable concurrently with the transition to instability of the first-order elliptic family, we cannot disallow the converse.<sup>33</sup> Thus, there may be an associated set of higher-order elliptic-hyperbolic I fixed-point pairs that closely surround a first-order hyperbolic II fixed point. However, we conjecture that at worst the effective influence of these higher-order elliptic families declines with higher values of  $Q/P$ , where the  $Q/P$  ratio becomes greater with increasing distance from the central invariant point of the mapping. In addition, our investigations indicate that the stability of the higher-order fixed-point families is principally determined by the nature of their associated first-order fixed points. This in turn implies that most higher-order families surrounding a first-order hyperbolic II point are unstable. Thus, there is non-trivial evidence that most fixed points are alternating hyperbolic I - hyperbolic II pairs in those  $Q/P$  regions for which the minimum  $f$ -curve exceeds unity. Finally let us note that  $Q/P$  regions exhibiting a preponderance of unstable families would also be expected to display widespread stochasticity.

We have now achieved our purpose in developing the stability analysis technique of Greene; namely, we can now predict the locations of the widely stochastic regions in a mapping by determining the residue spectrum of selected sequences of fixed points of the transformation and then by calculating the corresponding  $f$ -curve as a function of  $Q/P$  for those fixed points. Let us now take these numerical techniques,



which proved rather powerful in studying the stochastic properties of algebraic mappings, and apply them to the Henon and Heiles non-linear oscillator system in order to expose additional characteristics of stochastic behavior in the differential equation systems.

# CHAPTER VII

## STABILITY OF PERIODIC ORBITS OF THE HENON AND HEILES SYSTEM

In the Introduction we discussed the nonlinear oscillator system of Henon and Heiles and showed that the very regular trajectories occurring at low system energy became highly stochastic for large values of energy. In this chapter we shall demonstrate that this increasing stochasticity as the energy increases is associated with a shift from predominantly stable periodic orbits to preponderantly unstable periodic orbits in much the same fashion that stochastic behavior occurs in algebraic area-preserving mappings as one moves from the stable regions near the central invariant point into those more distant regions which contain mainly hyperbolic I - hyperbolic II fixed-point pairs. We shall also examine stability as a function of energy for two particular periodic orbits, illustrating the generic tendency of the system as a whole to develop an increasing number of unstable trajectories with increasing energy. Let us now direct our attention to the Henon and Heiles system and adapt the numerical procedures used for algebraic area-preserving mappings in Chapter VI to this differential equation system.

The Henon and Heiles Hamiltonian<sup>7</sup> introduced in Chapter I has the form

$$H = (1/2)(p_1^2 + p_2^2 + q_1^2 + q_2^2) + q_1^2 q_2 - (1/3)q_2^3 . \quad (\text{VII-1})$$

As in the Introduction, we choose the  $q_2, p_2$  plane with  $q_1 = 0, p_1 \geq 0$  to be the surface of section and consider the set of  $(q_2, p_2)$  points generated by a given trajectory as it intersects this surface of section. However, we now regard a given surface of section with constant energy as an area-preserving mapping  $T_h$  of the plane onto itself which is here generated by solving the differential equations obtained from Hamiltonian (VII-1). We note that the fixed points of  $T_h^Q$  ( $Q = 1, 2, 3, \dots$ ) represent the intersections of periodic solutions of these differential equations with the surface of section. We shall call these periodic orbits stable or unstable as their generated fixed points are elliptic or hyperbolic. Thus, we may determine the stability of the periodic orbits in the four-dimensional phase space by applying the linearization techniques of Chapter VI to the corresponding fixed points in the surface of section.

We utilize here the same basic procedure which was described earlier for the algebraic mappings in Chapter VI. In particular, we search numerically along the positive  $q_2$  axis for fixed points of  $T_h^Q$ , where  $Q$  may be either odd or even, since periodic orbits of the Henon and Heiles system with odd  $Q$  must pass through the  $q_2$  axis due to a symmetry of the level curve plane which is demonstrated analytically in Appendix A. Before presenting the results of this numerical search for fixed points of  $T_h$ , we should point out that the notation employed in Chapter VI will be used in this chapter in order to expedite the discussion and to emphasize the strong similarities between the algebraic mappings and the differential equation systems. In addition, we shall present the mathematical details of our computations in Appendices B and C.

In order to illustrate the pattern of fixed points for the Henon and Heiles system, we present Figure 25, which is a continuation of Figure 2. Here one observes an elliptic fixed-point family of four members with  $Q/P = 4/1$  which has a very small residue, indicating a very stable periodic orbit in phase space. Although not shown in the figure, there is an associated family of four hyperbolic I fixed points interleaved between the four elliptic points. Indeed, in Figure 25 we have in each instance plotted only one of the two associated families for given  $\omega = P/Q$ . Farther away from the central invariant elliptic fixed point of  $T_h$  whose coordinates are  $(0.303, 0.0)$  for this energy, we see the elliptic  $Q/P = 5/1$  family, which is surrounded by a hyperbolic I family of the second order in the hierarchy with  $Q/P = 55/11$ . We note in passing that several other second-order families associated with the  $5/1$  were found but are not plotted, those closest to the  $5/1$  being either elliptic or hyperbolic I, while the more remote were hyperbolic I or II fixed points. Thus, differential equation systems yield the same type of recursive, fixed-point structure indicated in our discussion of Figure 16 for the algebraic mappings. Next, lying even farther from and surrounding the central invariant point, there is a hyperbolic II family with  $Q/P = 8/1$ . A comparison of Figure 25 with Figure 2 indicates that the inner elliptic  $4/1$  family lies well within the stable level curve region, while the elliptic  $5/1$  family of Figure 25 lies on the borderline of the stochastic sea. Finally, the hyperbolic  $8/1$  is located in the unstable region itself, probably lying beyond the last Moser invariant curve for the  $T_h$  mapping.

Let us now calculate a spectrum of residue values for the fixed

1 Tick = 0.2

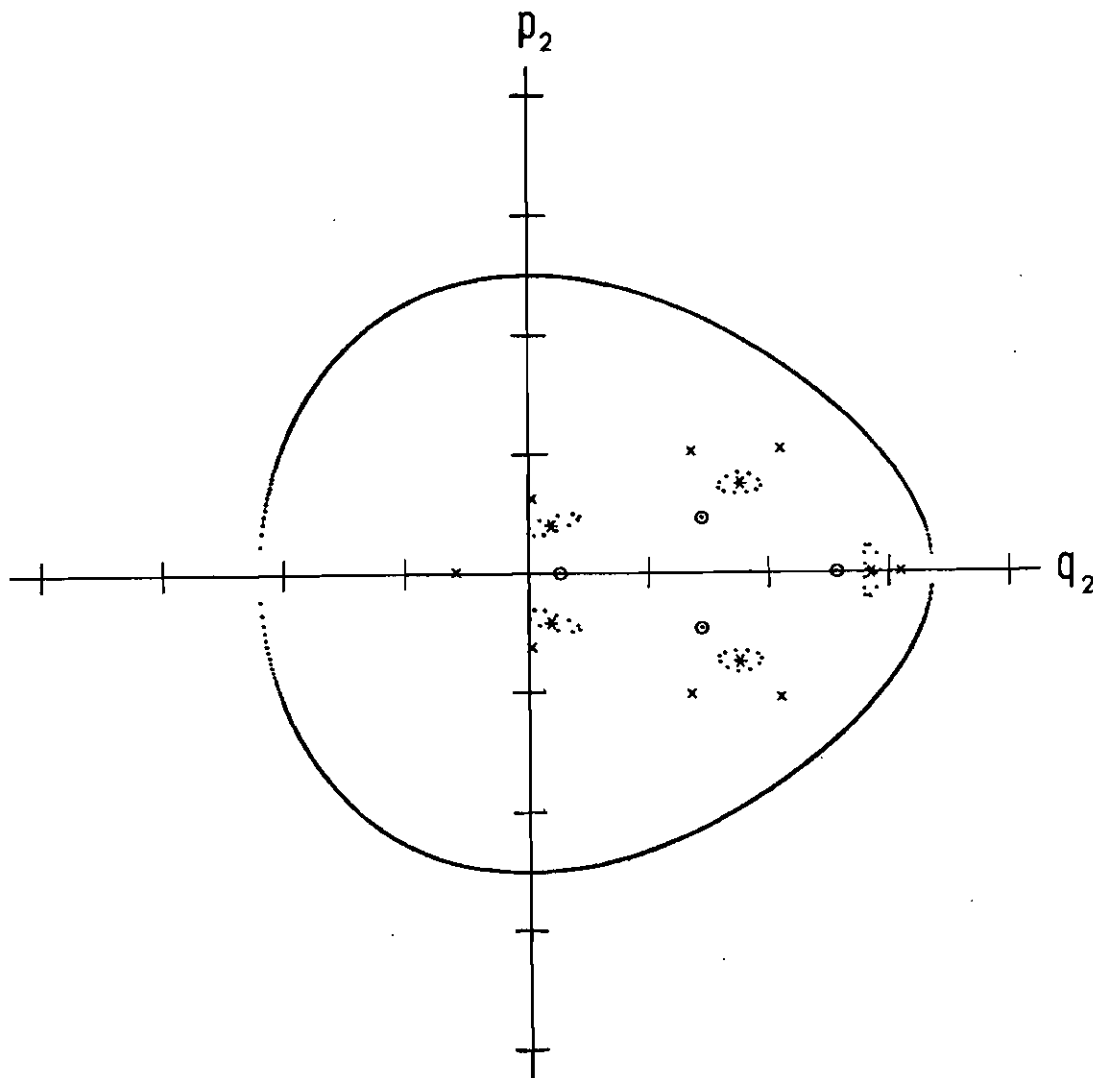


Figure 25. Selected Periodic Orbits in the Henon and Heiles Level Curve Plane for Energy  $E = 1/12$ . (The inner ring of four points denoted by (o) represents a stable elliptic orbit with  $Q/P = 4/1$ . The five points denoted by (\*) lie on a periodic orbit with  $Q/P = 5/1$  and have a residue almost unity. The sequence of 55 points indicated by (.) represents a hyperbolic I family with  $Q/P = 55/11$  in the second order of the hierarchy. The eight points represented by (x) lie on a hyperbolic II periodic orbit with  $Q/P = 8/1$ .)

points of the Henon and Heiles mapping  $T_h$  just as we did for the Greene algebraic mapping in Chapter VI. Noting that as before there is a regular decrease of rotation number  $\omega = P/Q$  with increasing distance from the central invariant point for the mapping  $T_h$ , we again calculate residues for sequences of fixed points with  $Q/P = k/\ell \pm 1/n$ . Here we take  $\ell = 1$  and let  $k$  be the set of smallest positive integers for which the corresponding orbits can be located. Using the procedure discussed in Appendix C, we determined that the factor  $\alpha$  of Equations (VI-20) equals unity for the Henon-Heiles mapping  $T_h$ . Furthermore, we here calculated both positive and negative residues, determining  $f$  by taking absolute values in Equation (VI-20b).

For the energy  $E = 1/12$  Figure 26 presents a plot of  $f = |R|^{2/Q}$  versus  $Q/P$ . This plot is based on the data for selected fixed-point sequences presented in Table 3. The same basic features of the earlier Figure 24 are present in Figure 26, with the important exception that the minimum  $f$ -curve in Figure 26 for the  $T_h$  mapping does not rise and remain above unity in the  $Q/P$  range considered. Thus, in keeping with the analysis of Chapter VI, we conjecture that most of the level curve plane is covered by fixed points which are members of elliptic-hyperbolic I pairs and that widespread stochasticity is not to be found at this energy. This appraisal is based on the observation that the  $f$ -curve shown in Figure 26 is empirically found to be the minimum  $f$ -curve for the region. As before, we located a host of fixed points for the  $T_h$  mapping representing a uniform sampling of  $Q/P$  values and found that their calculated  $f$ -values all lay on or above the  $f$ -curve presented in Figure 26. A further aspect of Figure 26 that should be mentioned is

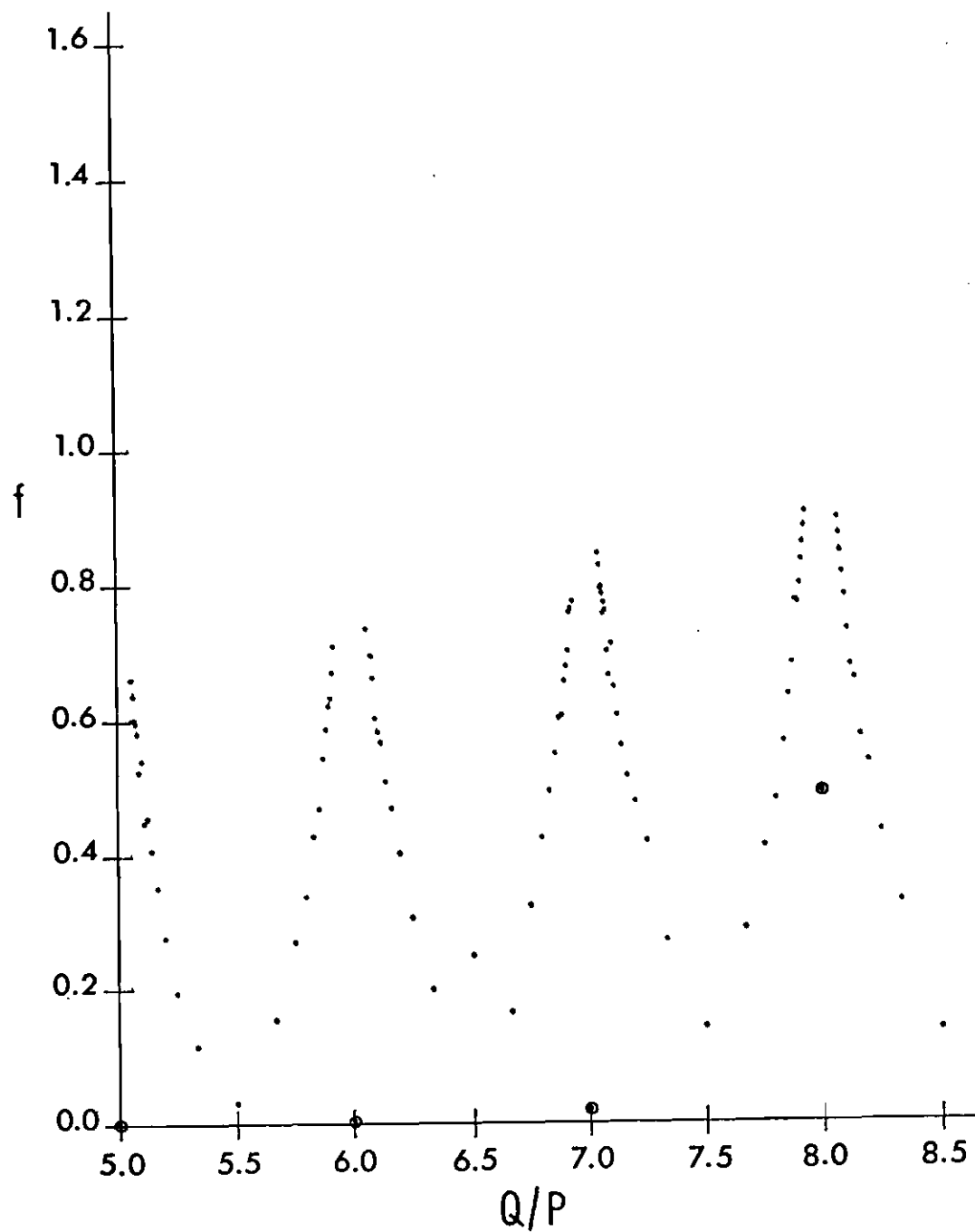


Figure 26. A Plot of  $f = |R|^{2/Q}$  Versus Inverse Rotation Number for Selected Fixed Points of the Henon and Heiles System at Energy  $E = 1/12$ .

Table 3. The Quantity  $f = |R|^{2/Q}$  As a Function of  $Q/P$  for Selected Fixed Points of the Henon and Heiles System at Energy  $E = 1/12$ .

No.	Q	P	Q/P	Residue	$f =  R ^{2/Q}$
1	5	1	5.0000	1.00000000-007	1.58489319-003
2	11	2	5.5000	4.51883022-009	3.03900913-002
3	6	1	6.0000	7.01268928-008	4.12377409-003
4	13	2	6.5000	1.12894530-004	2.47012487-001
5	7	1	7.0000	1.06660435-006	1.96659641-002
6	15	2	7.5000	4.14993099-007	1.40952284-001
7	8	1	8.0000	5.75775951-002	4.89850302-001
8	17	2	8.5000	4.22203676-008	1.35648300-001
9	16	3	5.3333	-2.91346265-008	1.14301303-001
10	21	4	5.2500	-3.24771761-008	1.93560608-001
11	26	5	5.2000	-5.54614518-008	2.76595735-001
12	31	6	5.1667	-1.00834686-007	3.53687733-001
13	36	7	5.1429	-9.77007875-008	4.07896419-001
14	41	8	5.1250	-1.01534027-007	4.55888989-001
15	46	9	5.1111	-9.92864912-009	4.48785382-001
16	51	10	5.1000	-1.55719917-007	5.40795544-001
17	56	11	5.0909	-1.43438778-008	5.24663617-001
18	61	12	5.0833	-6.80262321-008	5.82110971-001
19	66	13	5.0769	-4.06091892-008	5.97061295-001
20	71	14	5.0714	-1.54385765-008	6.02505156-001
21	76	15	5.0667	-3.67654454-008	6.37314324-001
22	81	16	5.0625	-5.47355496-008	6.61756189-001
23	17	3	5.6667	1.32147397-007	1.55136067-001
24	23	4	5.7500	-2.84201621-007	2.69618777-001
25	29	5	5.8000	1.39623252-007	3.36696394-001
26	35	6	5.8333	3.46333661-007	4.27393850-001
27	41	7	5.8571	-1.72410939-007	4.67817359-001
28	47	8	5.8750	5.80781872-007	5.42798768-001
29	53	9	5.8889	7.09915486-007	5.86097761-001
30	59	10	5.9000	-7.71199193-007	6.20562185-001
31	65	11	5.9091	3.40461799-007	6.32392513-001
32	71	12	5.9167	-6.63563837-007	6.69836065-001
33	77	13	5.9231	1.75805197-006	7.08794443-001
34	19	3	6.3333	2.08271087-007	1.98014862-001
35	25	4	6.2500	3.46246869-007	3.04194157-001
36	31	5	6.2000	7.33330274-007	4.01987805-001
37	37	6	6.1667	7.87967356-007	4.67822953-001
38	43	7	6.1429	4.75076037-007	5.08037721-001
39	49	8	6.1250	8.70814651-007	5.65783177-001



Table 3. The Quantity  $f = |R|^{2/Q}$  As a Function of  $Q/P$  for Selected Fixed Points of the Henon and Heiles System at Energy  $E = 1/12$ . (Continued)

No.	Q	P	Q/P	Residue	$f =  R ^{2/Q}$
40	55	9	6.1111	-3.31520259-007	5.81275722-001
41	61	10	6.1000	1.87086803-007	6.01743283-001
42	67	11	6.0909	9.72107588-007	6.61498382-001
43	73	12	6.0833	1.71345455-006	6.95062578-001
44	97	16	6.0625	-2.93299000-007	7.33339998-001
45	20	3	6.6667	1.41977725-008	1.64142869-001
46	27	4	6.7500	2.16714903-007	3.20894395-001
47	34	5	6.8000	4.58551281-007	4.23780009-001
48	41	6	6.8333	5.06422857-007	4.93063765-001
49	48	7	6.8571	5.53582033-007	5.48654884-001
50	55	8	6.8750	7.88617750-007	5.99884823-001
51	62	9	6.8889	1.69112732-007	6.04719641-001
52	69	10	6.9000	4.50937335-007	6.54728640-001
53	76	11	6.9091	-3.67083152-007	6.77098257-001
54	83	12	6.9167	-3.76017999-007	7.00141386-001
55	90	13	6.9231	3.43625137-006	7.56100743-001
56	97	14	6.9286	1.91432285-006	7.62260483-001
57	111	16	6.9375	6.29632936-007	7.73164394-001
58	22	3	7.3333	5.64704627-007	2.70385725-001
59	39	4	7.2500	3.21876421-006	4.18042025-001
60	36	5	7.2000	1.56323333-006	4.75823368-001
61	43	6	7.1667	6.24842518-007	5.14554274-001
62	50	7	7.1429	-5.19892141-007	5.60578620-001
63	57	8	7.1250	5.97959525-007	6.04835964-001
64	64	9	7.1111	8.46928945-007	6.46018891-001
65	71	10	7.1000	5.20141412-006	7.09836538-001
66	78	11	7.0909	1.08704004-007	6.62891108-001
67	85	12	7.0833	-2.51909000-007	6.99415327-001
68	92	13	7.0769	3.06619673-006	7.58828229-001
69	99	14	7.0714	2.55746341-006	7.70950427-001
70	106	15	7.0667	-3.07324042-007	7.53571496-001
71	113	16	7.0625	1.01958434-006	7.83347374-001
72	120	17	7.0588	-1.00069950-006	7.94337492-001
73	127	18	7.0556	3.50719517-007	7.91308491-001
74	141	20	7.0500	1.29546294-006	8.25065253-001
75	155	22	7.0455	1.92308388-006	8.43810914-001
76	23	3	7.6667	-5.74828413-007	2.86649475-001
77	31	4	7.7500	9.83724024-007	4.09678750-001

Table 3. The Quantity  $f = |R|^{2/Q}$  As a Function of  $Q/P$  for Selected Fixed Points of the Henon and Heiles System at Energy  $E = 1/12$ . (Concluded)

No.	Q	P	Q/P	Residue	$f =  R ^{2/Q}$
78	39	5	7.8000	6.01017216-007	4.79698720-001
79	47	6	7.8333	1.46940591-006	5.64668118-001
80	55	7	7.8571	3.51128052-006	6.33363879-001
81	63	8	7.8750	5.47211124-006	6.80702427-001
82	71	9	7.8889	1.04492490-004	7.72434302-001
83	79	10	7.9000	3.07470484-005	7.68718221-001
84	87	11	7.9091	4.87810964-005	7.95938196-001
85	95	12	7.9167	1.50884926-004	8.30903214-001
86	103	13	7.9231	3.43380698-004	8.56512119-001
87	111	14	7.9286	8.62903816-004	8.80627240-001
88	119	15	7.9333	2.26194513-003	9.02687677-001
89	25	3	8.3333	8.29728071-007	3.26223214-001
90	33	4	8.2500	9.46369521-007	4.31432415-001
91	41	5	8.2000	2.61507860-006	5.34173308-001
92	49	6	8.1667	-1.15536940-006	5.72350512-001
93	57	7	8.1429	6.11894062-006	6.56260642-001
94	65	8	8.1250	3.03905835-006	6.76453774-001
95	73	9	8.1111	9.53126426-006	7.28521679-001
96	81	10	8.1000	4.30843198-005	7.80199043-001
97	89	11	8.0909	9.45452609-005	8.12016658-001
98	97	12	8.0833	2.66772634-004	8.43941204-001
99	105	13	8.0769	6.44971787-004	8.69419441-001
100	113	14	8.0714	1.74692478-003	8.93697810-001

that the  $Q/P = 5/1$  fixed point lies very near the central invariant point while the  $Q/P = 17/2$  fixed point is located fairly close to the bounding curve on the right in Figure 1, which means that nearly all of the  $q/p$  level curve plane for energy  $E = 1/12$  about the central invariant point is represented in Figure 26. Thus, Figure 26 indicates that the Henon and Heiles system would be expected to exhibit rather regular behavior with only a small measure of isolated stochastic regions at this low energy. This expectation is verified in Figure 1; it is also supported by the KAM Theory as well as the Moser and Birkhoff Theorems.

In Figure 27 we plot the curve  $f = |R|^{2/Q}$  versus  $Q/P$  for selected fixed-point sequences of the  $T_h$  mapping at energy  $E = 1/8$ . We notice here the very rapid escalation of the minimum  $f$ -curve to a value which remains greater than unity for  $(Q/P)$  values greater than five. We re-emphasize here that the fixed points represented on this graph have  $Q/P$  values that lie in approach sequences of the type  $Q/P = k/\ell \pm 1/n$  for  $\ell = 1$  and  $k = 3, 4, 5$ , which according to Greene<sup>19</sup> do approximate the minimum  $f$ -curve. Thus, noticing from Equation (VI-20b) that  $f > 1$  implies  $|R| > 1$  for  $\alpha = 1$  and recalling the relationships (VI-16), we now claim that nearly all fixed-point families are hyperbolic at energy  $E = 1/8$  when  $Q/P > 5.0$ . These facts in turn imply that the region beyond the "chain" of five islands in Figure 2 is almost entirely stochastic.

To summarize our results thus far, we have demonstrated that the KAM prediction of stability at low energies is verified by the  $f$ -curve in Figure 26. Here, most periodic orbits which exert a relatively widespread influence on the phase space trajectories generate fixed points

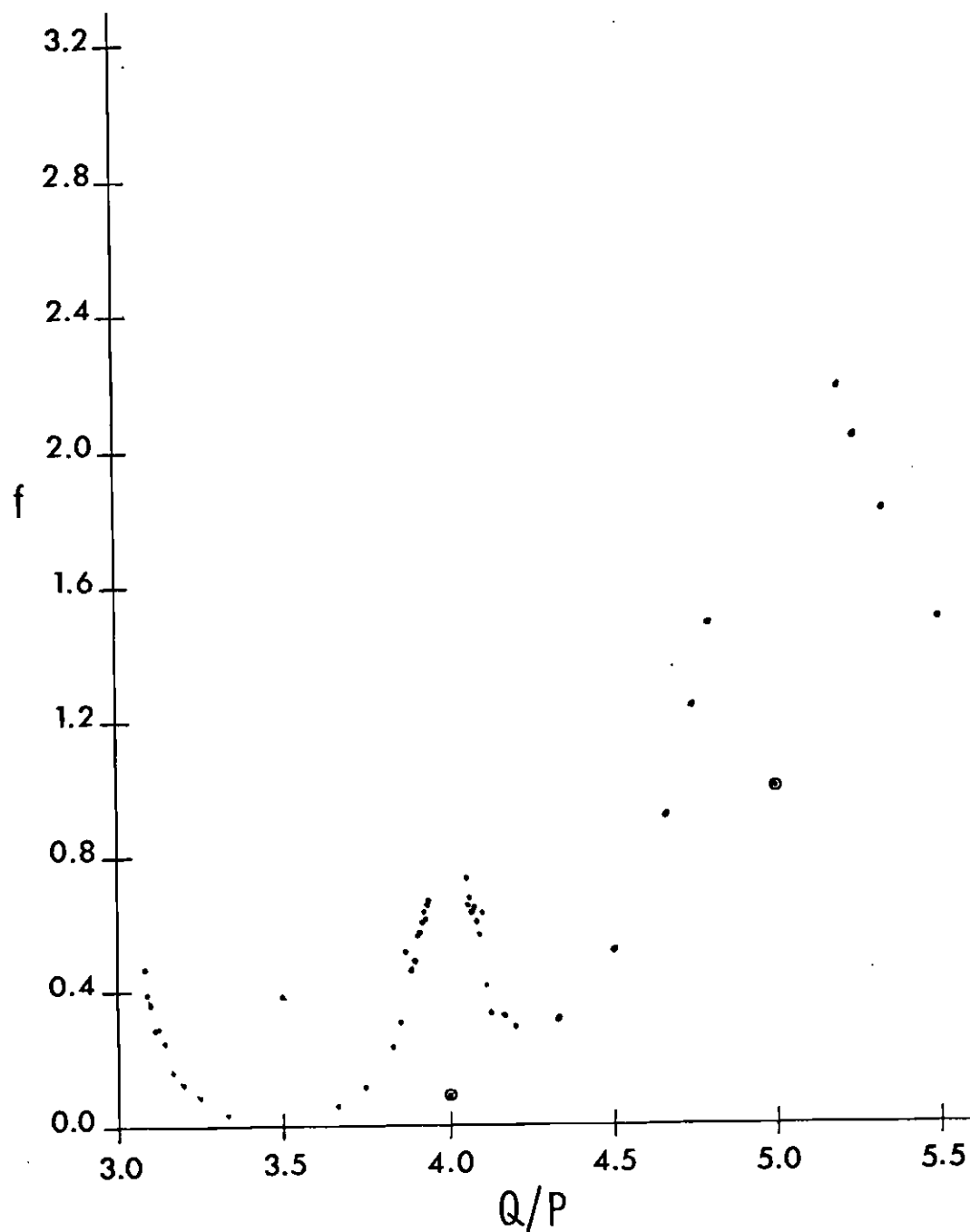


Figure 27. A Plot of  $f = |R|^{2/Q}$  Versus Inverse Rotation Number for Selected Fixed Points of the Henon and Heiles System at Energy  $E = 1/8$ . (Notice the rather quick excursion toward  $f > 1$  associated with a preponderance of hyperbolic I - hyperbolic II pairs of fixed points.)

consisting of elliptic-hyperbolic I pairs. On the other hand, we have shown in Figure 27 that at the energy  $E = 1/8$  a sizeable portion of the level curve plane beyond the chain of five islands in Figure 2 contains a dense or nearly dense set of hyperbolic fixed points. These periodic orbits act as unstable scattering centers for nearby, non-periodic orbits in the four-dimensional phase space for Hamiltonian (VII-1), yielding the stochastic behavior shown in Figure 2. Consideration of Figures 26 and 27 leads one to conjecture that an increasing number of stable periodic orbits become unstable as the system energy is increased. This conjecture could be proved by showing that increasing portions of the minimum  $f$  versus  $Q/P$  curve lie above unity as the system energy approaches the dissociation value  $E = 1/6$ . Unfortunately, such a continued study is not economically feasible. Nonetheless, the generic trend toward an increasing percentage of hyperbolic I - hyperbolic II fixed points at higher energies seems sufficiently well established by Figures 26 and 27 that a continued study of this type does not appear necessary.

The second portion of our research with the Henon and Heiles differential equation system focuses on the residue values of two distinct periodic orbits as functions of system energy. The behavior of these two periodic orbits illustrates the general tendency of the system as a whole to generate increasingly unstable trajectories with increasing energy. In addition, this investigation reveals new details about the evolution of fixed points in the mapping plane. We begin this study by examining the graph of residue versus system energy shown in Figure 28, which was drawn from the data of Table 4. The periodic orbit

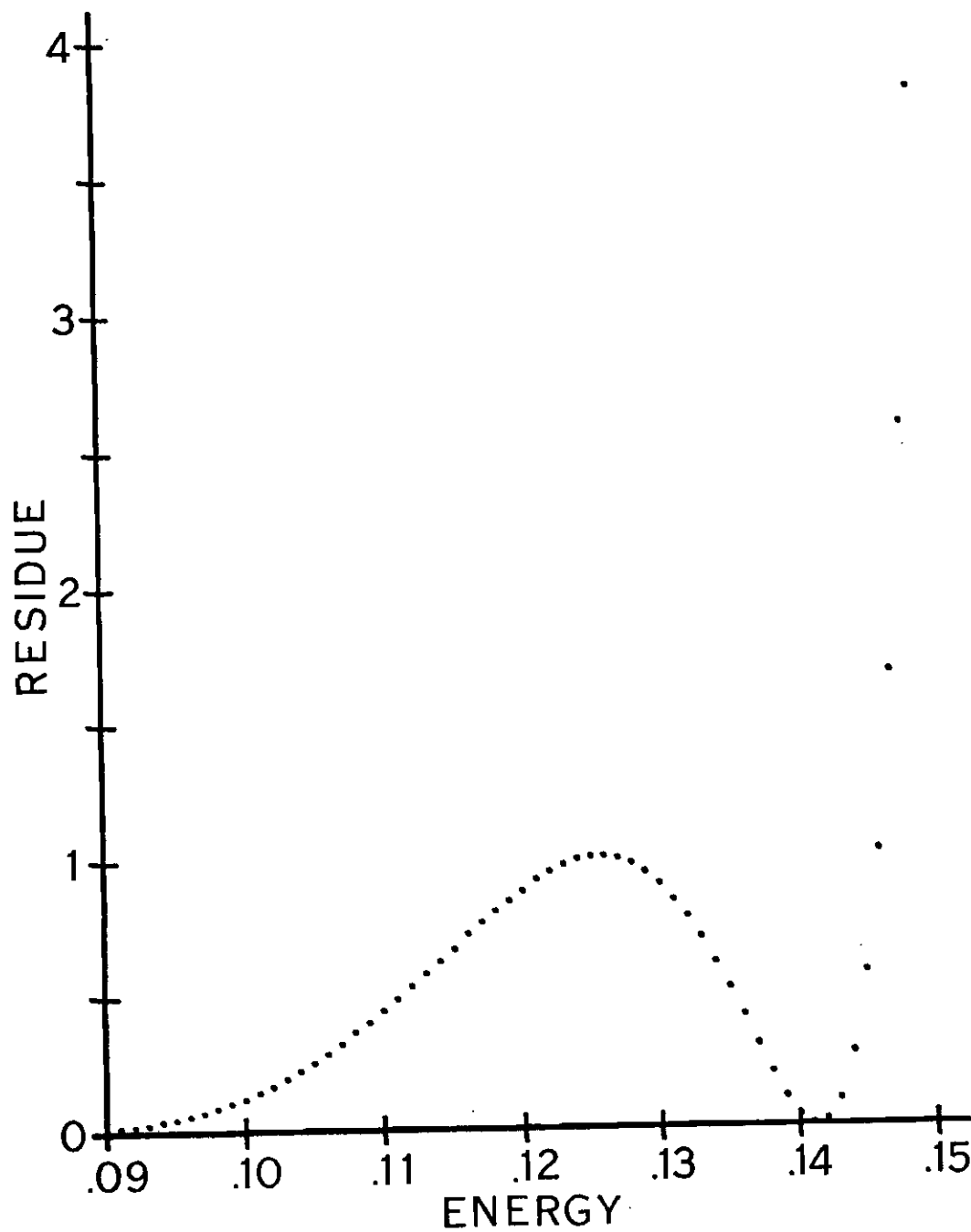


Figure 28. The Profile of Residue Versus System Energy for the 5/1 Fixed-Point Family in the Henon and Heiles System.

Table 4. The Residue as a Function of System Energy for the 5/1 Fixed-Point Family in the Henon and Heiles System.

No.	Energy	Residue
1	9.00000000-002	7.65559467-003
2	9.10000000-002	1.23813019-002
3	9.20000000-002	1.74976990-002
4	9.30000000-002	2.30622491-002
5	9.40000000-002	3.35885822-002
6	9.50000000-002	4.02586752-002
7	9.60000000-002	5.20653643-002
8	9.70000000-002	6.46093910-002
9	9.80000000-002	8.24968332-002
10	9.90000000-002	1.01268199-001
11	1.00000000-001	1.16386857-001
12	1.01000000-001	1.41652065-001
13	1.02000000-001	1.63353426-001
14	1.03000000-001	1.90734734-001
15	1.04000000-001	2.19225255-001
16	1.05000000-001	2.48844646-001
17	1.06000000-001	2.79603714-001
18	1.07000000-001	3.16151088-001
19	1.08000000-001	3.58483580-001
20	1.09000000-001	3.92609987-001
21	1.10000000-001	4.37093927-001
22	1.11000000-001	4.82555504-001
23	1.12000000-001	5.24241857-001
24	1.13000000-001	5.71343635-001
25	1.14000000-001	6.19054067-001
26	1.15000000-001	6.62545461-001
27	1.16000000-001	7.15544047-001
28	1.17000000-001	7.59225095-001
29	1.18000000-001	8.02598978-001
30	1.19000000-001	8.40723013-001
31	1.20000000-001	8.77875150-001
32	1.21000000-001	9.18262022-001
33	1.22000000-001	9.47638937-001
34	1.23000000-001	9.70182668-001
35	1.24000000-001	9.90002143-001
36	1.25000000-001	9.97464268-001
37	1.26000000-001	1.00000000+000
38	1.27000000-001	9.91640312-001
39	1.28000000-001	9.72861308-001
40	1.29000000-001	9.39951210-001

Table 4. The Residue as a Function of System Energy for the 5/1  
Fixed-Point Family in the Henon and Heiles System.  
(Concluded)

No.	Energy	Residue
41	1.30000000-001	8.97096226-001
42	1.31000000-001	8.39598348-001
43	1.32000000-001	7.71882545-001
44	1.33000000-001	6.94090496-001
45	1.34000000-001	6.02241222-001
46	1.35000000-001	5.05978765-001
47	1.36000000-001	4.06535308-001
48	1.37000000-001	2.97067383-001
49	1.38000000-001	1.93317715-001
50	1.39000000-001	1.03148572-001
51	1.40000000-001	3.55634799-002
52	1.41000000-001	1.00589784-003
53	1.42000000-001	1.59569617-002
54	1.43000000-001	9.48479468-002
55	1.44000000-001	2.67453336-001
56	1.45000000-001	5.62555279-001
57	1.46000000-001	1.01300786+000
58	1.47000000-001	1.66493475+000
59	1.48000000-001	2.57457460+000
60	1.49000000-001	3.80158063+000



considered here generates the fixed-point family with  $Q/P = 5/1$ , which we have also encountered previously in Figures 2 and 25. In Figure 28 we note that the inception residue is very small when this periodic orbit first evolves from the central invariant point near energy  $E = 0.085$ , and we also observe that the interleaved  $5/1$  elliptic-hyperbolic I fixed-point families eventually convert to hyperbolic I - hyperbolic II fixed-point families near the energy  $E = 0.141$ . We mention in passing that the central invariant point and the  $5/1$  fixed point on the  $q_2$  axis indicated in Figures 2 and 25 both move to the right at rather uniform rates with increasing energy; however, the  $5/1$  gradually separates itself from the central invariant point because it has the higher uniform rate of travel. The rising and falling pattern we see in the residue curve in Figure 28 will be explained later in connection with Figure 30.

In Figure 29 we present a very similar curve of residue versus system energy for the fixed-point family with  $Q/P = 8/1$ , whose location for energy  $E = 1/8$  was shown in Figure 25. We note that the  $8/1$  family appears at a lower energy than the  $5/1$  family, and that the elliptic  $8/1$  fixed-point family becomes a hyperbolic II family around energy  $E = 1/8$ , which is also lower than the transition energy for the  $5/1$  family. These two examples are typical of the general case. Fixed-point families with larger values of  $Q/P$  first appear and then move away from the central invariant point at lower system energies than do the fixed points with smaller  $Q/P$  ratios, in agreement with our earlier observation that the  $Q/P$  quotients became larger for increasing distances from the central invariant point. In addition, we may point out that this

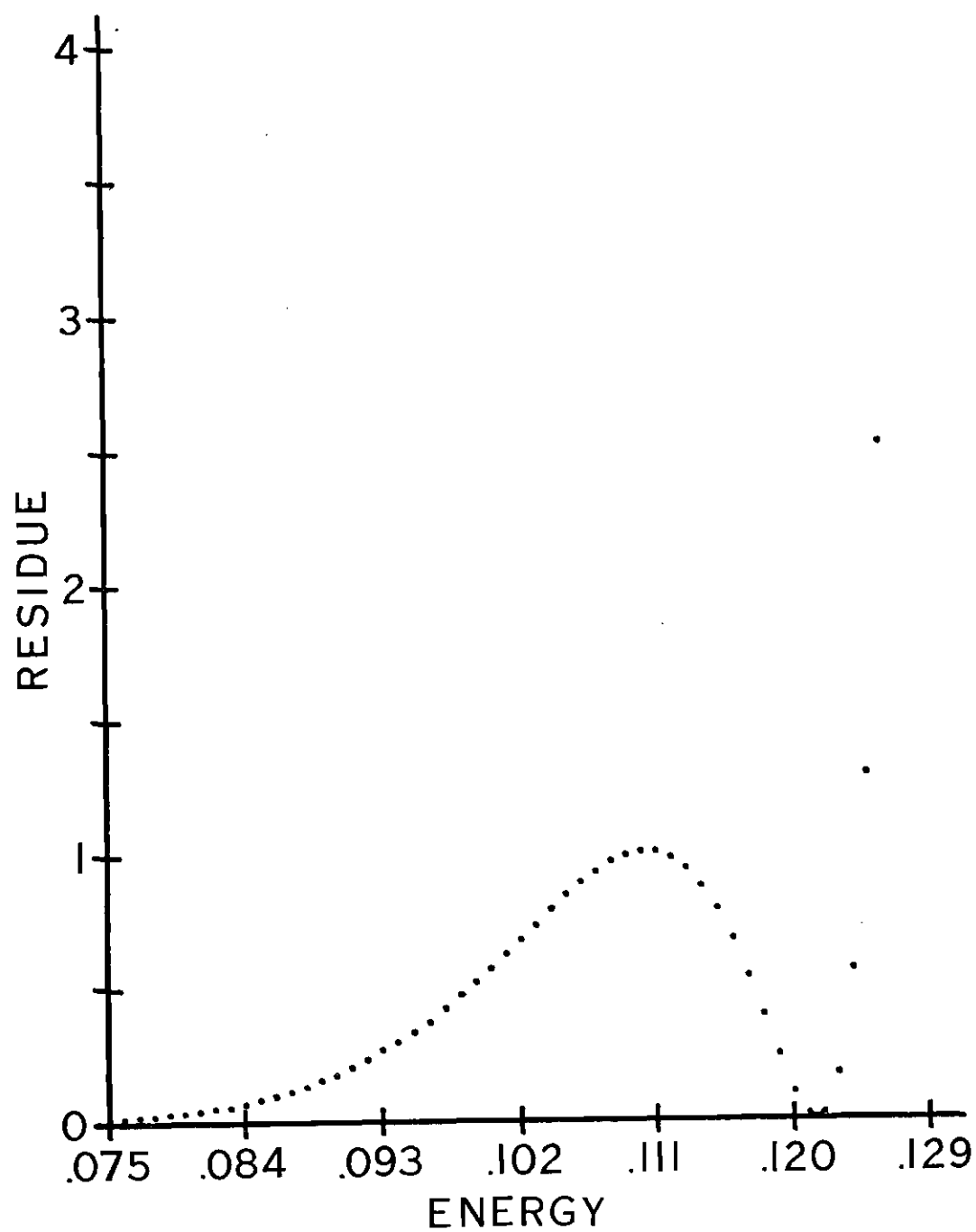


Figure 29. The Profile of Residue Versus System Energy for the 8/1 Fixed-Point Family in the Henon and Heiles System.

phenomenon of increasing  $Q/P$  for greater separations from the central invariant point is also seen in the arrangement of second-order fixed points around their associated first-order elliptic members. We find, for example, that the fixed-point family with  $Q/P = 55/11$  shown in Figure 25 lies farther away from the  $5/1$  fixed point than does the family with  $Q/P = 30/6$ , which is not shown in Figure 25. When these second-order families are viewed from a  $5/1$  fixed point itself, the inverse rotation numbers are  $11/1$  and  $6/1$  respectively, with the  $6/1$  family lying closer to the central  $5/1$  fixed point. In addition, the second-order families lying closer to the first-order elliptic fixed points are more stable than those located farther away, which is analogous to the first-order  $5/1$  family remaining stable after the  $8/1$  elliptic family has become hyperbolic II. Thus, the macroscopic stability progression in the first order of the hierarchy implied by Figures 28 and 29 is also observed in sequentially higher orders of the hierarchy as anticipated in Figure 16.

The last property of individual periodic orbits we shall consider is illustrated in Figure 30. At energy  $E \approx 0.121$ , a numerical search along the positive  $q_2$  axis reveals at least two distinct fixed-point families with  $Q/P = 8/1$ . The original  $8/1$  continues to be found at the location predicted by its past uniform rate of travel rightward, while a new bifurcated  $8/1$  lies on the  $q_2$  axis just to the left of the original  $8/1$ . As the system energy increases, the original  $8/1$  continues to move rightward at the usual rate, but the bifurcated version appears to move leftward for a small energy range and then to move rightward at a uniform rate (but more slowly than the original  $8/1$ ) for succeeding

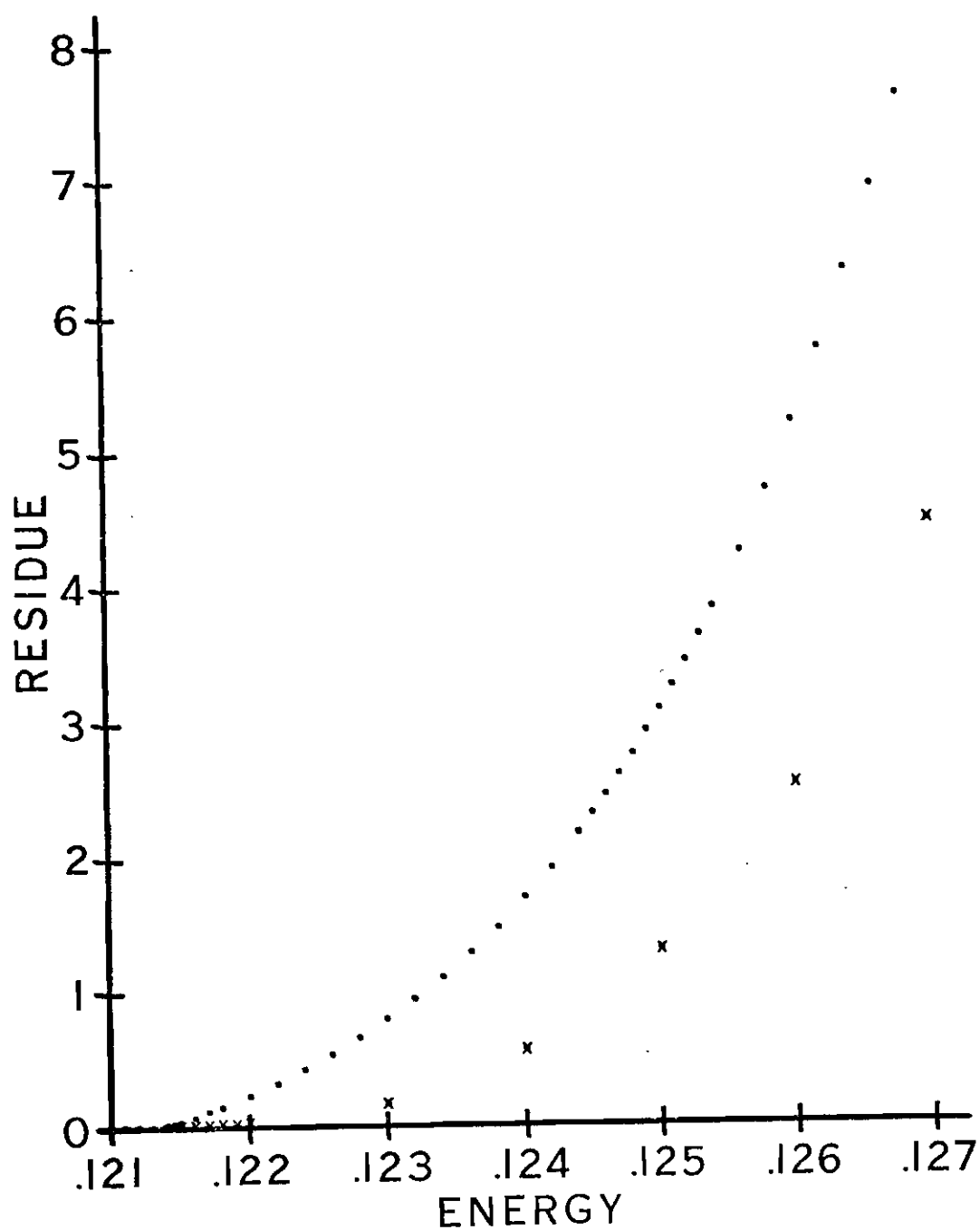


Figure 30. A Plot of Residue Versus System Energy for the Original and Bifurcated 8/1 Periodic Orbits of the Henon and Heiles System. (The original 8/1 family is denoted by (x), and the bifurcated 8/1 family is depicted by (•).)

higher energies. It is entirely possible that more than one new  $8/1$  evolved from the original  $8/1$ , but only one was found along the  $q_2$  axis in the search.

Greene<sup>19,35</sup> offers an explanation of the bifurcation process itself and then attempts to connect the unexpected rising and falling pattern of the residue profiles in Figures 28 and 29 with the bifurcation concept. According to Greene, each original  $8/1$  fixed point is the center of a second-order system of surfaces and fixed points with relative  $P/Q$  values lying between zero and  $\omega_0$ , where the maximum rotation number  $\omega_0$  about the  $8/1$  and the residue  $R$  of the  $8/1$  fixed point are connected via

$$R = \sin^2 \pi \omega_0 . \quad (\text{VII-2})$$

In Equation (VII-2)  $\omega_0$  is the limiting rotation number about the  $8/1$  when the  $8/1$  itself is considered to be a central fixed point. Referring to Figure 29, when  $R = 1/2$  near the energy  $E = 0.099$ , the maximum rotation number for the second-order hierarchy surrounding the  $8/1$  fixed point extends to  $\omega_0 = 1/4$ , which is equivalent to  $P/Q = 4/32$  around the central invariant point. When  $R = 1$  near  $E = 0.11$ , the linearized matrix  $M$  becomes the negative identity matrix and  $\omega_0 = 1/2$ . When  $R = 1/2$  again near  $E = 0.117$ , the maximum rotation number  $\omega_0$  around the  $8/1$  fixed point is  $3/4$ . There is a crisis at  $R = 0$  near  $E = 0.1215$  for which the linearized matrix  $M$  becomes the identity matrix. The ambiguity in  $\omega_0$  is probably best resolved by taking  $\omega_0 = 1$  for  $R = 0$ . Thus, we can view the bifurcated  $8/1$  as having  $\omega_0 = P/Q = 1/1$  about the

original  $8/1$ , which is equivalent to  $Q/P = 8/1$  about the central invariant point. We note that a bifurcation of the original  $8/1$  into another  $8/1$  at  $R = 1$  is not possible since  $\omega_0 = 1/2$ , which implies that  $Q/P = 16/2$  around the central fixed point is the lowest  $Q$  and  $P$  multiple of the  $8/1$  that could evolve. An extensive numerical search for a second  $8/1$  at  $E = 0.11$  was unsuccessful, whereas the second  $8/1$  is easily found at  $E = 0.1215$  when  $R = 0$  and  $\omega_0 = 1$ .

The bifurcation process also helps to explain the distribution of rotation numbers for the first-order fixed points in a given level curve plane of the Henon and Heiles system. Using Equation (VII-2), we see that the limiting rotation number  $\omega_0$  about the central invariant point depends upon the residue of the central elliptic point, where the residue is determined by the given value of system energy. We note that specifying a maximum  $\omega_0$  is equivalent to setting a minimum value of  $Q/P$  for the first-order fixed-point families, although Equation (VII-2) does not indicate a concurrent upper bound on  $Q/P$ . Since the central invariant point is itself tending to pass from elliptic to hyperbolic II as the system energy increases, we anticipate from Equation (VII-2) that the  $\omega_0$  is also increasing in the same fashion that we observed earlier for the  $8/1$  family. Consequently, as the system energy increases, the minimum  $Q/P$  ratio in the level curve plane declines, which explains why the  $T_h^Q$  families with the smallest values of  $(Q/P)$  do not bifurcate from the central fixed point until higher energies are achieved. Moreover, an existing  $T_h^Q$  family will move away from the central fixed point as the system energy is increased, which implies that the  $Q/P$  ratios increase with increasing distance

from the central fixed point.

In this chapter we have sought to examine the nature of stochastic behavior in the Henon and Heiles differential equation system by applying some of the techniques of mapping analysis developed in Chapters V and VI. We have indicated that the widely stochastic regions of phase space contain a preponderance of unstable periodic solutions of Hamiltonian (VII-1), and that the nature of any given periodic orbit apparently tends toward eventual instability as the system energy is increased. This chapter has attempted to expose additional insight into stochastic behavior in the physical nonlinear oscillator systems, thereby enhancing our understanding of the irreversible processes.

## CHAPTER VIII

## CONCLUSIONS

One of the cornerstones of equilibrium statistical mechanics is the assignment of equal probability to states of equal energy for an isolated system using the microcanonical distribution. In this particular distribution the small interaction terms coupling the internal degrees of freedom are neglected in the expression for the potential energy, since such terms are presumed significant only in destroying almost all well behaved constants of the motion and in bringing the system to equilibrium. Accordingly, statistical mechanics assumes that these small coupling terms, even though extremely weak, have a profound effect upon the individual system trajectories. One of the central concerns of this thesis has been to establish the criteria under which very weak nonlinear coupling terms can indeed radically alter the unperturbed motion. Using a nearly-linear oscillator system as an example, we have demonstrated that statistical behavior can occur provided that there is resonance overlap. In this view each individual resonant interaction attempts to carry the unperturbed phase space trajectory into a distinct and previously unvisited region of the energy surface. When many resonances act simultaneously, the system trajectory is influenced very strongly by first one and then another resonant term with the result that most system trajectories wander freely over much of the energy surface. In this thesis we have used the term stochastic behavior to denote the more or less random wandering of a trajectory over the energy surface.



Let us now indicate the role of resonance overlap in the wholesale destruction of well behaved constants of the motion. Using Hamiltonian (II-7) as an example, we note that each resonant interaction, if acting alone, yields an integrable system in which linear combinations of the  $J$  variables are constants of the motion.<sup>25</sup> When resonance overlap is present, the trajectory is very strongly influenced by first one and then another resonance; consequently, the actual trajectory may be approximated by a sequence of short integrable system segments with an analytically distinct set of constants of the motion for each segment. Thus, the trajectory as a whole would not have a well behaved constant of the motion beyond the total energy, since the approximate "local" constants of the motion have a varying analytic form. In addition, the number of overlapping resonant terms increases as  $N^2$  in Hamiltonian (II-7), so that we would expect the motion to become more and more pathological as the number of resonantly coupled oscillators increases. This latter view of the source of stochasticity for Hamiltonian (II-7) is quite closely related to the notions leading Poincaré to a proof of the non-existence of analytic constants of the motion for nonlinear systems.

In the first portion of this thesis we demonstrated for arbitrarily small  $\gamma$  that the purely resonant, nearly-linear, three-oscillator Hamiltonian (III-1) did indeed exhibit those freely wandering trajectories which would be expected to lead to macroscopically irreversible behavior. Clearly, fluctuations from equilibrium would occur and recur, due to Poincaré recurrences. If the motion along a trajectory approaching equilibrium were reversed, the system would proceed at the onset through

an excursion away from equilibrium and then return. Consequently, recurrence and irreversibility constitute paradoxes only if one insists on a monotonic approach to equilibrium without fluctuations. In regard to the origin of the irreversibility for these nonlinear oscillator systems, we note that the exponential pair-orbit separation in stochastic regions represents that stirring of phase space which Gibbs envisioned as causing irreversibility. In particular, the rate at which these pair-orbits diverge gives at least one measure of entropy production in the system. We anticipate that extensive use of pair-orbit separation as a probe for studying various nonlinear systems will occur in the future. Indeed, a beginning has already been made by R. H. Miller<sup>37</sup> and by E. Myles Standish, Jr.<sup>38</sup> In addition, it is likely that this exponential pair-orbit separation will be used as a starting point for rederiving master equations governing the approach to equilibrium for nearly-linear oscillator systems.

Whereas the first portion of this thesis sought to establish the criteria under which a nearly-linear oscillator system can exhibit widespread stochasticity and to demonstrate that such stochastic systems possess exponentially separating orbits, the second half of the thesis directed its attention to elaborating further details of the motion in the stochastic region of the system phase space. To this end, we showed that the surface of section graphs, which illustrated typical behavior of trajectories in nonlinear oscillator systems, could be regarded as area-preserving mappings of a plane onto itself.<sup>18,19</sup> Since there is such a close correspondence between the pathology of trajectories for Hamiltonian systems and the pathology of area-preserving mappings, a

study of the generic properties of algebraic area-preserving mappings was used to yield additional insight into the stochastic behavior present in the many-body problem. In particular, the direct study of algebraic systems provided us with powerful mapping theorems not available for differential equation systems. For example, the Moser<sup>8</sup> and Birkhoff<sup>29</sup> Theorems for algebraic mappings were used to predict the dissolution processes that take place when small perturbation terms are added to smooth algebraic transformations. These theorems show that the introduction of small nonlinearity into an algebraic system exhibiting otherwise regular behavior will cause the invariant curves bearing rational rotation numbers to decompose primarily into alternating elliptic (stable) and hyperbolic I (unstable) fixed points of the mapping. A typical mapping generated by a slightly nonlinear, algebraic area-preserving transformation was presented in Figure 16 from the paper by Arnold,<sup>23</sup> showing the stable areas surrounding the elliptic fixed points and the waving separatrices emanating from the unstable fixed points of the associated hyperbolic I families.

A detailed study of the nature of the fixed-point families, predicted by the Moser and Birkhoff Theorems and illustrated in Figure 16, revealed additional properties of stochastic behavior. In particular, we observed that the intersecting separatrices from adjacent hyperbolic fixed points of an unstable family encompass the elliptic fixed points of the associated stable family. When weak nonlinear perturbations are added to an otherwise smooth algebraic transformation, the total measure of the stable regions is only slightly reduced since the separatrices from adjacent hyperbolic fixed points almost join smoothly, and hence

they merely partition the original stable area into various stable sub-regions. However, as the amount of nonlinearity in the mapping is increased, the separatrices intersect at larger angles and thus progressively erode away more and more of the stable areas surrounding the associated elliptic fixed points. The culmination of the erosion process is reached when the stable elliptic fixed-point families themselves change character and become unstable hyperbolic II families. Thus, our mapping studies have provided a geometrical interpretation to the advent of increasing stochasticity which accompanies increasing nonlinearity in the transformation. Moreover, we conjecture from these studies of algebraic mappings that the stochastic regions of a mapping plane are dominated by alternating hyperbolic I - hyperbolic II fixed points.

In order to empirically verify the validity of this conjecture, we modified a stability analysis technique developed by Greene<sup>19</sup> and determined the nature of the periodic orbits in the stochastic region of phase space for the Henon and Heiles Hamiltonian (VII-1). Using this procedure, we demonstrated that at low system energy in the Henon and Heiles mapping the surface of section is dominated by alternating elliptic-hyperbolic I fixed points. On the other hand, as the system passes beyond the province of KAM Theory with increasing energy, we observe an increasing occurrence of hyperbolic I - hyperbolic II fixed-point pairs. In addition, we showed that regions of phase space which contain mainly unstable periodic orbits coincide with the domains that display widespread stochasticity.

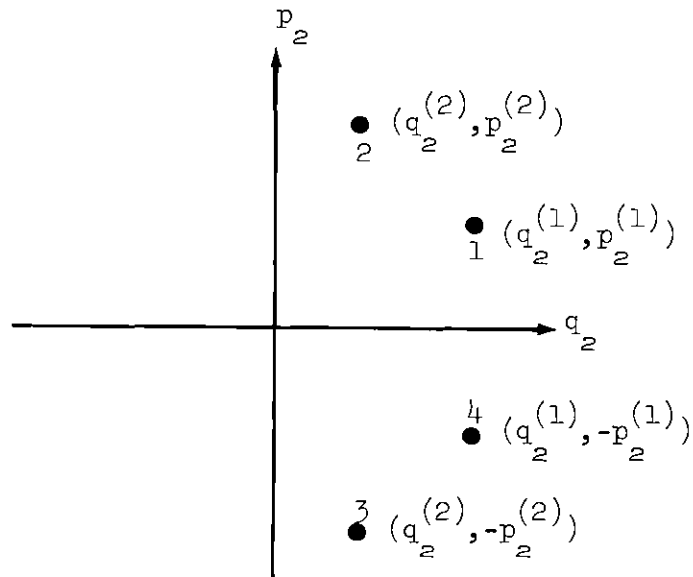
In conclusion, let us indicate two possible extensions of the

research described in this thesis. First, we could diversify our approach in studying stochastic behavior by considering the periodic orbits of nonlinear oscillator systems as scattering centers for the non-periodic trajectories. In this view, we might be able to measure the effective influence of an unstable periodic orbit by calculating a type of scattering cross section for the periodic solution. Furthermore, the application of scattering theory to a stochastic region of phase space could perhaps elucidate additional pathological distinctions between the hyperbolic I and hyperbolic II fixed points and thereby reveal new characteristics of stochastic behavior.

Second, and perhaps more important, it would be of great interest to know the extent to which a set of successive iterates of a point lying in a stochastic region is truly random. In this regard, Contopoulos<sup>39</sup> has found that two different starting points in a supposedly stochastic region of phase space can generate similar but distinctly different macroscopic patterns of trajectory intersections in a surface of section. In partial response to this issue, we observed in our studies that quasi-periodic orbits exist in Hamiltonian systems, which give the appearance of periodicity for several mapping iterations, but which then display very erratic behavior for all succeeding iterations. Thus, within the constraints of numerical mapping accuracy, there appear to be transition regions in phase space separating stable areas from stochastic domains, which might explain Contopoulos' result. It is hoped that future research in ergodic theory will answer these and other related questions that have arisen from our own research efforts.

## APPENDIX A

This appendix demonstrates that the  $q_2 p_2$  level curve plane for the Henon and Heiles Hamiltonian given in Equation (VII-1) is symmetric about the  $q_2$  axis. Consider the following diagram which represents four points in the  $q_2 p_2$  plane with  $q_1 = 0$ ,  $p_1 \geq 0$ , for each point:



The Henon and Heiles Hamiltonian is given by

$$H = \frac{p_1^2}{2} + \frac{p_2^2}{2} + (1/2) \left[ q_1^2 + q_2^2 + 2q_1^2 q_2 - (2/3)q_2^3 \right], \quad (\text{A-1})$$

for which Hamilton's equations of motion become

$$\dot{q}_1 = \frac{\partial H}{\partial p_1} = p_1, \quad (\text{A-2a})$$

$$\dot{q}_2 = \frac{\partial H}{\partial p_2} = p_2, \quad (\text{A-2b})$$

$$\dot{p}_1 = -\frac{\partial H}{\partial q_1} = -q_1 - 2q_1 q_2, \quad (\text{A-2c})$$

$$\dot{p}_2 = -\frac{\partial H}{\partial q_2} = q_2^2 - q_2 - q_1^2. \quad (\text{A-2d})$$

Hamiltonian (A-1) is sufficiently smooth so that the existence and uniqueness theorems of differential equations as applied to Equations (A-2) guarantee that there is only one orbit through each point of the allowable phase space. We postulate that the trajectory passing through the point 1 with coordinates  $(q_1^{(1)} = 0, q_2^{(1)}, p_1^{(1)} \geq 0, p_2^{(1)})$  will next intersect the  $q_2 p_2$  plane in point 2 with coordinates  $(q_1^{(2)} = 0, q_2^{(2)}, p_1^{(2)} \geq 0, p_2^{(2)})$ , which defines a mapping represented by

$$T(q_1^{(1)} = 0, q_2^{(1)}, p_1^{(1)} \geq 0, p_2^{(1)}) = \quad (\text{A-3})$$

$$(q_1^{(2)} = 0, q_2^{(2)}, p_1^{(2)} \geq 0, p_2^{(2)}).$$

The symmetry of the  $q_2 p_2$  plane about the  $q_2$  axis can be demonstrated by proving that if Equation (A-3) holds, then the "mirror" point 3 maps into the "mirror" point 4. We write this latter mapping as

$$T(q_1^{(3)} = 0, q_2^{(2)}, p_1^{(2)} \geq 0, -p_2^{(2)}) = \quad (\text{A-4})$$

$$(q_1^{(4)} = 0, q_2^{(1)}, p_1^{(1)} \geq 0, -p_2^{(1)}),$$

since the values of  $p_1$  are determined from Equation (A-1).

A given trajectory in phase space will exactly reverse its evolution if we replace  $t$  by  $-t$  in Hamilton's equations. However, we observe from Hamilton's equations that an alternative reversing procedure for Hamiltonians that are even functions in each momentum is to change the signs of the momenta and to perform a second integration in the forward time direction. The final position in phase space achieved by this technique is the mirror image in the momenta coordinates of the initial point from which the first integration began. If we apply the momentum reversing technique to return from point 2 to point 1, we have via momenta sign changes that

$$T(q_1^{(3)} = 0, q_2^{(2)}, p_1^{(2)} \leq 0, -p_2^{(2)}) = \quad (A-5)$$

$$(q_1^{(4)} = 0, q_2^{(1)}, p_1^{(1)} \leq 0, -p_2^{(1)}).$$

Equation (A-5) is the same as Equation (A-4) except the  $p_1$  momenta are negative instead of positive as required by the conditions for the  $q_1 p_2$  level curve plane. This difference is reconciled in the following manner.

We observe that the equations of motion are invariant under the canonical transformation given by

$$q_1 = -q_1, \quad (A-6a)$$

$$q_2 = q_2, \quad (A-6b)$$



$$p_1 = -p_1, \quad (\text{A-6c})$$

$$p_2 = p_2. \quad (\text{A-6d})$$

Since the two points indicated in Equation (A-5) lie on a solution to the equations of motion, Equations (A-6) ensure that the Equation (A-5) points with the signs of  $q_1$  and  $p_1$  reversed also lie on a solution for Hamiltonian (A-1). Therefore, using the transformation of Equations (A-6), we may rewrite the mapping sequence of Equation (A-5) in the form

$$T(q_1^{(3)} = 0, q_2^{(2)}, p_1^{(2)} \geq 0, -p_2^{(2)}) = \quad (\text{A-7})$$

$$(q_1^{(4)} = 0, q_2^{(1)}, p_1^{(1)} \geq 0, -p_2^{(1)}),$$

which was to be proved.

## APPENDIX B

In this appendix we first present some of the mathematical considerations involved in locating the fixed-point families of the Henon and Heiles differential equation system, which we investigated in Chapter VII. We then discuss the accuracy criteria used in determining the linearization matrix  $M$  of Equation (VI-17) for the Henon and Heiles system.

All calculations were performed in double precision on the Univac 1108 Computer using an eighth-order Runge-Kutta integration routine<sup>34</sup> to generate the trajectories with a step size of 0.05 seconds. Passages of  $q_1$  within  $\pm 10^{-10}$  of zero and values of  $p_1 \geq 0$  were required before the associated  $(q_2, p_2)$  coordinates were accepted for plotting. In locating the fixed points of  $T_h^Q$  for this differential equation mapping, we found that the reproducibility of the calculations was much more sensitive to the thickness of the level curve plane, measured by the maximum allowable deviation of  $q_1$  from zero, than it was to the closeness with which a trial initial point returned to its original location after  $Q$  intersections with the surface of section. The combination of a level curve plane thickness of  $\pm 10^{-10}$  and a return after  $Q$  intersections to within  $10^{-8}$  of the initial starting point was found to provide a sufficient requirement for accurately locating the fixed-point family of  $T_h^Q$ .

Once a fixed-point family was located within the desired precision, the associated linearized matrix  $M$  was determined using the second method in conjunction with Equations (VI-17) - (VI-19). Here we transposed

$(x,y)$  into  $(q_2, p_2)$  and identified an iteration of the algebraic mapping with successive trajectory intersections of the surface of section. There were two criteria used to judge the reliability of the four computed elements of the matrix  $M$ . First, the determinant of  $M$  should equal unity, since  $M$  is the Jacobian matrix representing the linearized transformation for the canonical, area-preserving mapping  $T_h$ . For the matrix  $M$  in Equation (VI-17) the unit determinant condition becomes

$$a^2 + b^2 - c^2 - d^2 = 1. \quad (B-1)$$

The second accuracy check on the computed matrix  $M$  evolves from a consideration of the quadratic form  $\Psi(q_2, p_2)$  given by<sup>19</sup>

$$\begin{aligned} \Psi(q_2, p_2) \equiv & (b-c)(q_2 - q_2^{(0)})^2 + 2d(q_2 - q_2^{(0)})(p_2 - p_2^{(0)}) + \\ & (b+c)(p_2 - p_2^{(0)})^2, \end{aligned} \quad (B-2)$$

which may be shown to be an invariant of the matrix  $M$  of Equation (VI-17), which is

$$M = \begin{bmatrix} (a+d) & (c+b) \\ (c-b) & (a-d) \end{bmatrix}. \quad (B-3)$$

Here  $M$  gives the linearized mapping about a fixed point at  $(q_2^{(0)}, p_2^{(0)})$ . For the linearized transformation matrix  $M$ ,  $\Psi(q_2, p_2)$  represents an elliptic or hyperbolic form as  $M$  is linearized about a stable or unstable fixed point respectively. We also note from Equation (B-3) that the

coefficients  $(b-c)$ ,  $2d$ , and  $(b+c)$  occurring in  $\Psi$  are directly determined by the elements of the matrix  $M$ . If the origin of coordinates is translated to the fixed point  $(q_2^{(0)}, p_2^{(0)})$  and if the symmetry in  $p_2$  from Appendix A is invoked for the invariant curves around fixed points on the  $q_2$  axis, then we see that  $d \equiv 0$  in the matrix  $M$  of Equation (B-3). This equality of the diagonal elements of the matrix  $M$  constitutes the second accuracy condition.

During the actual computation of the matrix  $M$  by the second method, the program determined the four matrix elements for each of five different separation distances between the fixed point and the second members of the two perpendicularly-oriented pairs. It was found for most fixed-point families considered that the same value of pair-separation distance simultaneously provides the best satisfaction of both accuracy conditions stated above. In those cases which indicated a different optimal pair-separation distance for meeting each accuracy condition, the trace of the matrix  $M$  that best satisfies the determinant condition was almost the same as the trace from the linearized matrix for which the diagonal elements are the most nearly equal. In view of the minor difference between the two accuracy checks, we elected to determine the residue from that linearized matrix  $M$  whose determinant most nearly equaled unity.

## APPENDIX C

This appendix presents the analysis used to determine the factor  $\alpha$  in Equations (VI-20) for the Henon and Heiles differential equation mapping  $T_h$  discussed in Chapter VII. Taking the absolute value in Equation (VI-20b), we have the relationship

$$f(P/Q) = |R/\alpha|^{2/Q}, \quad (C-1)$$

from which we obtain

$$\ln f = (2/Q) \cdot \ln(1/\alpha) + (2/Q) \cdot \ln |R|, \quad (C-2)$$

where we require that  $\alpha > 0$ . We may rewrite Equation (C-2) in the form

$$Q \cdot \ln f = 2(\ln |R| - \ln \alpha). \quad (C-3)$$

As we mentioned previously in Chapter VI, Equations (VI-20) are used primarily for first-order fixed-point families, although the empirical investigation described below shows a consistency of results when Equations (VI-20) are also used for second-order families. If we now consider a first-order fixed point and an associated second-order family, which is required to have the same  $Q/P$  ratio as the first-order family it surrounds, we may write Equation (C-3) for each family separately, using  $f = f(P/Q)$ , as

$$Q_1 \cdot \ln f = 2(\ln |R_1| - \ln \alpha), \quad (C-4a)$$

$$Q_2 \cdot \ln f = 2(\ln |R_2| - \ln \alpha), \quad (C-4b)$$

where the subscripts 1 and 2 denote the first-order and second-order families respectively. We then obtain from Equations (C-4) an expression for  $\ln \alpha$ , which is given by

$$\ln \alpha = \frac{Q_1 \cdot \ln |R_2| - Q_2 \cdot \ln |R_1|}{Q_1 - Q_2}. \quad (C-5)$$

In order to determine the value of  $\alpha$  to be used in Equation (C-1) for the system energy  $E = 1/8$ , several second-order families, associated with the first-order fixed-point family bearing  $Q/P = 5/1$ , were used successively in combination with the  $5/1$  family in Equation (C-5), which gave an average value of  $\alpha \approx 1.0$ . In addition, numerical computations showed that the  $f$ -function as defined by Equation (C-1) is relatively insensitive to variations in  $\alpha$ , especially at low energies. Thus, we took  $\alpha = 1$  in our determinations of the  $f$ -curves via Equation (C-1) for both energies  $E = 1/12$  and  $E = 1/8$ .

## FOOTNOTES

- <sup>1</sup>G. Walker and J. Ford, Phys. Rev. 188, 416(1969).
- <sup>2</sup>A. N. Kolmogorov, Dokl. Akad. Nauk. SSSR 98 , 527(1954).
- <sup>3</sup>V. I. Arnold, Russian Math. Surveys 18, 9(1963).
- <sup>4</sup>J. Moser, Nachr. Akad. Wiss. Göttingen, II Math Physik Kl. 1(1962).
- <sup>5</sup>K. R. Symon and A. M. Sessler, Proceedings CERN Symposium on High Energy Accelerators and Pion Physics, Geneva 1956, Vol. I, p. 44.
- <sup>6</sup>E. Thiele and D. J. Wilson, J. Chem. Phys. 35, 1256(1961).
- <sup>7</sup>M. Henon and C. Heiles, Astron. J. 69, 73(1964).
- <sup>8</sup>J. Moser, Mem. Am. Math. Society 81, 1(1968).
- <sup>9</sup>G. Contopoulos, Bull. Astron. 2, 223(1967).
- <sup>10</sup>N. Saito, N. Ooyama, Y. Aizawa, and H. Hirooka, Supp. Prog. of Theor. Phys. 45, 209 (1970).
- <sup>11</sup>D. Bunker, J. Chem. Phys. 37, 393(1962).
- <sup>12</sup>F. M. Izrailev and B. V. Chirikov, Soviet Phys.-Doklady 11, 30 (1966).
- <sup>13</sup>G. M. Zaslavskii, "Statistical Irreversibility in Nonlinear Systems", Preprint 254, Institute of Nuclear Physics, Novosibirsk, U. S. S. R., 1968.
- <sup>14</sup>N. J. Zabusky and G. S. Deem, J. Comput. Phys. 2, 126(1967).
- <sup>15</sup>W. H. Jefferys, Astron. J. 71, 306(1966).
- <sup>16</sup>A. S. Wightman, in Statistical Mechanics at the Turn of the Decade, Edited by E. G. D. Cohen (Marcel Dekker, New York, 1971), pp. 1-32.
- <sup>17</sup>D. V. Anosov and Ja. Sinai, Russian Math. Surveys 22, 103(1967).
- <sup>18</sup>V. I. Arnold and A. Avez, Ergodic Problems of Classical Mechanics (W. A. Benjamin, Inc., New York, 1968).

- <sup>19</sup>J. M. Greene, J. Math. Phys. 9, 760(1968).
- <sup>20</sup>E. Merzbacher, Quantum Mechanics (John Wiley and Sons, Inc., New York, 1964).
- <sup>21</sup>H. Goldstein, Classical Mechanics (Addison-Wesley Press, Inc., Cambridge, Mass., 1951), p. 241.
- <sup>22</sup>C. Froeschle, Astron. and Astrophys. 9, 15(1970).
- <sup>23</sup>Arnold, op. cit., p. 85.
- <sup>24</sup>J. G. Sinai in Statistical Mechanics, Proceedings of the I. U. P. A. P. Meeting, Copenhagen, 1966, Edited by T. A. Bak (W. A. Benjamin, Inc., New York, 1967), p. 559.
- <sup>25</sup>E. T. Whittaker, Analytical Dynamics (Cambridge University Press, London, 1961), pp. 322-323.
- <sup>26</sup>Goldstein, op cit., pp. 247-250.
- <sup>27</sup>M. Henon, Quart. of Appl. Math. 27, 291(1969).
- <sup>28</sup>G. D. Birkhoff, Acta. Math. 43, 1-119(1920).
- <sup>29</sup>G. D. Birkhoff, Dynamical Systems (American Mathematical Society Publications, New York, 1927).
- <sup>30</sup>Figure 20 is reproduced from a private communication from L. Jackson Laslett of the Lawrence Radiation Laboratory, Berkeley.
- <sup>31</sup>L. Jackson Laslett, AEC Research and Development Report NYO-1480-101, New York University, 1968 (Unpublished).
- <sup>32</sup>M. Henon, Annales d'Astrophysique 28, 992(1965).
- <sup>33</sup>G. Contopoulos, Astron. J. 75, 108(1970).
- <sup>34</sup>L. J. Gallaher et. al., "Study of the Methods for the Numerical Solution of Ordinary Differential Equations", Final Report, Project A-831, Engineering Experiment Station, Georgia Institute of Technology, Atlanta, Georgia, 1968.
- <sup>35</sup>This discussion is based on private communications with J. M. Greene of the Plasma Physics Laboratory, Princeton.
- <sup>36</sup>Goldstein, op. cit., pp. 242-243.
- <sup>37</sup>R. H. Miller, Astrophys. J. 140, 250(1964).



<sup>38</sup>E. Myles Standish, Jr., "Numerical Studies of the Gravitational Problem of N Bodies", Thesis, Yale University, 1968.

<sup>39</sup>G. Contopoulos, Astron. J. 76, 147(1971).

## VITA

Gary Hamilton Lunsford was born on May 19, 1940, in Springfield, Missouri, the son of W. E. and Mildred Lunsford. He was graduated from Greenwood High School in Springfield, Missouri, in 1958. Following one year at Drury College in Springfield, Missouri, he attended Duke University in Durham, North Carolina, where he received the degree of Bachelor of Science in Physics in 1962. He then attended the University of Illinois in Urbana, Illinois, where he received the degree of Master of Science in Physics in 1964. While attending Illinois, he held a half-time research assistantship in the Computer Sciences Department, where he worked under Dr. John R. Pasta. Mr. Lunsford then was awarded an NSF Graduate Traineeship for one year of study in the Space Sciences Laboratory at the University of California, Berkeley.

In 1967 Gary H. Lunsford was employed by the Federal Systems Division of the IBM Corporation in Huntsville, Alabama, where he engaged in trajectory analysis studies for the Saturn launch vehicle. In September, 1968, he was granted an Educational Leave by IBM to complete doctoral studies in the Physics Department at the Georgia Institute of Technology in Atlanta, Georgia. His work for the Ph.D. Degree in Physics was completed in 1971. While attending Georgia Tech, Mr. Lunsford held an NDEA Fellowship and taught several undergraduate physics courses. Upon completion of the Ph.D. program, he was re-employed by the Federal Systems Division of IBM at Morris Plains, New Jersey, where he engaged in studies on the Sentinel ABM System.

In 1966 Gary H. Lunsford married the former Miss Judith Ann Zandrew. Mr. Lunsford is a member of Phi Eta Sigma, Phi Beta Kappa, and Sigma Pi Sigma.